SPECTROSCOPIC AND LASING PROPERTIES OF RARE-EARTH ION BASED LASER MATERIALS

By

ROGER RONALD PETRIN

Bachelor of Science

Southeastern Massachusetts University

North Dartmouth, Massachusetts

1987

Submitted to the Faculty of the
Graduate College of the
Oklahoma State University
in partial fulfillment of
the requirements for
the Degree of
DOCTOR OF PHILOSOPHY
May, 1993

OKLAHOMA STATE UNIVERSITY

SPECTROSCOPIC AND LASING PROPERTIES
OF RARE-EARTH ION BASED
LASER MATERIALS

Thesis Approved:

Richard C. Powell
Thesis Adviser

Donna Kay Bandy

Roger J. Reeves

Bruce A. Wade

Edward T. Keller

Thomas C. Collins
Dean of the Graduate College

ACKNOWLEDGMENTS

A great many individuals have contributed to the completion of this work, both on a professional and personal level. Without the support, encouragement, and assistance of these individuals, my time at Oklahoma State University would not have been as rewarding as it has been. I would like to express my gratitude to my research adviser for the past four years, Dr. Richard C. Powell. The guidance he has given me in this work, the experience I have gained working in his lab on a large number of projects, and simply the exposure to the wide variety of research projects and individuals in his lab have been invaluable. I also want to thank my thesis committee members, Drs. Bruce J. Ackerson, Donna K. Bandy, Edward T. Knobbe, and Roger J. Reeves. The discussions I have had with them about a wide variety of topics in physics, both directly and indirectly associated with this work, have been extremely rewarding. I would especially like to acknowledge Dr. Reeves for the conversations we have had and the assistance he has given me. I must also thank Dr. William A. Sibley for providing me with the opportunity to work in his laboratory my first 18 months at Oklahoma State University and for the many hours he spent teaching physics to an "engineer". I also acknowledge the rest of the faculty in the physics department at Oklahoma State University, two of whom have been especially influential and important in my study here: Dr. Paul Westhaus and the late Dr. Earl Lafon. A course taught by either of them was always a rewarding challenge and their dedication to teaching excellence has been inspiring. I benefitted greatly from the many hours they spent assisting and guiding me through "the gory details".

The assistance of my co-workers has also been very important in the completion of this work. I would like to thank Dr. Mahendra Jani for his assistance in and discussions of much of the research I have done, notably that involving

Tm,Ho:YAG. I would like to acknowledge Dr. Michael Kliewer for assistance in my studies of Nd-doped materials. Thanks also go to Ms. Carol Paulin, who spent many hours obtaining and assisting in the analysis of the absorption spectra in Chapter IV. I would also like to thank Drs. Tasoltan T. Baisev, Baha Jassemnejad, Antonio Munoz F., and Donald Yeh for their guidance and office mates Drs. Valentina French and Mark Petrovic and Mssrs. Scott Holmstrom, James Murray, Bahman Taheri, and Keith Ver Steeg for the many discussions we have had and the assistance they have provided. Additionally, I thank Mr. Brian Markey for developing the software used in the computer simulations in this work.

I would also like to acknowledge a number of individuals who have not directly contributed to this work, but whose support has been on a more personal level. Ms. Carol Wicksted, whose overall support and encouragement has kept everything in perspective. I thank those who struggled through classes with me and those who helped celebrate afterwards, fellow students Mike and Linda Clark, Henry John, Ulf Nobbman, Steve Paulin, Dave Schoonmaker, Doyle St. John, the "Dead Dinner Society", especially Sunnie Thompson, and once again separated by field, the "chemists", Candee Chambers and Dr. Tommy Sewell. I must also thank my roommate for the past four years, John Hays, and his wife, Dr. Kathy Swallows. The conversations I have had with him have made me think much more deeply about physics than I would have otherwise. Additionally, I would especially like to express my gratitude to Donna Gagne for the friendship, support, and encouragement she has given me the past six years.

I thank my family, my sisters, Claire and Diane, and their families, who have been there for support when I needed it, and my "big" brother, Dr. Ronald Petrin, his wife Liz, and their family for the wonderful times we have had together. I especially thank Ron for the guidance he has provided through the conversations we have had over the years. It has been greatly rewarding and appreciated.

Lastly, I want to thank my parents, my father George, who did not survive to see this work completed, and my mother Marie. They were always there to

encourage me to excel, to watch over me while I tried, to assist me when I needed help, and to praise me when I was done. I dedicate this work to them.

I gratefully acknowledge financial support during this work from a Fellowship in Areas of National Need from the U.S. Department of Education. Additional support from the Naval Research Laboratory and the U.S. Army Research Office is also acknowledged.

TABLE OF CONTENTS

Chapter Page

LIST OF TABLES

LIST OF FIGURES

CHAPTER I

INTRODUCTION

The development and understanding of rare-earth ion based laser systems has long been an important part of laser physics. As early as 1958 Schawlow and Townes[1] suggested that the rare-earth ions, also called the lanthanide ions, might possibly be used to produce an optical equivalent of the maser (microwave amplification by the stimulated emission of radiation), the laser (light amplification by the stimulated emission of radiation). Although the first laser developed, the ruby laser (Cr^{3+}:Al_2O_3),[2] was not based on a lanthanide ion, rare-earth ion based lasers were soon developed.[3] An important step in laser development was the room temperature Nd:$CaWO_4$ laser operating at $\approx$1.0 μm.[4] Unlike the ruby laser, which operated as a three level laser with the terminal level of the laser transition the highly populated ground state, Nd^{3+} lasers operating at 1.0 μm operated as a four level laser, with the terminal level well above the ground state and therefore depopulated. The lower population in the terminal level of the laser transition reduced the flashlamp pump energy required for laser emission to begin and led to improved efficiencies. Since this early work, rare-earth ion based laser systems, especially those based on Nd^{3+}, have played a dominant role in the development of new materials and the study of solid state laser physics. A good review showing the scope of solid state laser material development was compiled by Kaminskii in Ref.[5].

The study of solid state laser systems is driven by the numerous requirements for new applications along with the desire for a basic understanding of the physical mechanisms important in the laser materials. The need for higher efficiencies, higher powers and operation at different wavelengths is extremely important in

continuing interest and furthering study. Only through an understanding of the physical processes active in the materials can systems be optimized for better performance. Recent developments in other fields, for example the development of high power semiconductor diode lasers, are also very important. Systems based on materials that can be optically pumped by diode lasers offer the possibility of more compact and efficient lasers. Although the optical properties required by such materials are similar in many ways to those required for traditional flashlamp pumped systems, there are important differences in operating conditions that must be considered. One example is the intense nearly monochromatic nature of the emission from diode lasers must be very carefully matched to the narrow absorption bands of the rare-earth doped laser materials to insure efficient absorption. This is in contrast to traditional systems where the broad band emission of the flashlamp often overlaps multiple absorption bands. Another factor that must often be considered is the high pump intensities present in diode pumped materials may lead to multiple photon absorption effects not seen in flashlamp pumped systems. The need to understand these additional processes, and to develop materials which can efficiently absorb the diode laser pump energy and convert it to laser output at the desired wavelength is an important part of the fields of laser physics and laser materials.

Summary of Thesis

This work addresses a number of current issues in the fields of laser physics and laser materials research, especially problems associated with the understanding of diode pumped rare-earth ion based laser systems. Chapter II provides some of the theoretical background required for understanding the optical properties of rare-earth ions incorporated into solid state host materials. After a discussion of the origin and energy level structure of the states responsible for the optical properties, the mechanisms responsible for transitions between these states are discussed. These mechanisms include radiative decay via forced electric dipole transitions, non-radiative multiphonon decay, and non-radiative ion-ion energy transfer. A

useful formalism for quantitatively analyzing and understanding excited state dynamics, the rate equation formalism, is also introduced. The chapters following this introduction to the optical properties of rare-earth ions each address different laser systems, materials, and physical processes that are of present interest.

Chapter III presents an analysis of an important laser system for medical and remote sensing applications: Tm,Ho:$Y_3Al_5O_{12}$ (yttrium aluminum garnet or YAG). The Tm,Ho:YAG material system has a number of interesting properties that make it a useful material for use as a diode laser pumped 2.1 μm laser. Diode lasers operating in the 780 nm spectral region can be used to optically pump Tm^{3+} ions. A series of ion-ion interactions then occur resulting eventually in energy transfer to the Ho^{3+} ions which are responsible for the 2.1 μm laser emission. This study primarily uses the technique of time resolved spectroscopy to investigate and quantify the effects of a number of these processes. The results of this spectroscopic approach to understanding the energy transfer processes are then used in a rate equation based computer simulation of the dynamics of laser operation. These results are compared to previous experimental results. Additionally, the effects of some previously suggested mechanisms leading to lower laser efficiency are considered and quantified using the rate equation model. A new possible loss mechanism, the effect of which is highly dependent on the pump wavelength selected, is also identified and investigated.

The next chapter, Chapter IV, considers absorption and emission characteristics of two Nd^{3+} doped garnets, yttrium aluminum garnet (YAG) and gadolinium scandium gallium garnet (GSGG). Although Nd^{3+} doped garnets, especially Nd:YAG, have been extensively studied a number of interesting effects are not well understood. Here the origin of blue and green emission observed under excitation with an alexandrite laser operating in the 720-800 nm spectral region is investigated. The effects of the processes leading to this emission may be important for diode laser pumped systems since the operating wavelength of the alexandrite laser is close to that of the diode lasers often used to optically pump Nd^{3+} lasers. The

spectral content of the blue and green emission is examined carefully and compared to that expected from an analysis of the energy levels. From this analysis the most likely level of origin for the blue emission is identified. A Judd-Ofelt analysis of the absorption data for each material is also performed and the effect of severe intermixing of Stark levels from different multiplets in regions of the spectra on the analysis is considered. The results of the Judd-Ofelt analysis are then used to confirm the identity of the upper state and to predict which excited state absorption paths are responsible for populating it.

Chapter V considers a relatively new type of Nd^{3+} doped laser material, a heavy metal fluoride glass. The random structure of the glass host causes site to site variations in the crystal field strength and symmetry. This variation causes differences in the energies of the crystal field split Stark levels for rare-earth ions in different sites. Although the variation is not as great in fluoride glasses as in oxide glasses, the inhomogeneous broadening of the transitions that does occur offers broader absorption lines that can be more easily matched to the output of diode lasers than the sharp lines present in crystals. Fluoride glasses also offer slower non-radiative multiphonon relaxation rates than those found in other materials which leads to longer effective fluorescence lifetimes for some excited states. In this chapter the results of a study of some of the spectroscopic and laser properties of Nd:ZBAN are presented. The stimulated emission cross section is determined spectroscopically and from the laser efficiency measurements. Again, as in the crystalline hosts discussed in Chapter IV, blue and green emission is observed and characterized. A Judd-Ofelt analysis is used to explain the observed wavelength dependence of the excited state absorption (ESA) of pump photons. Finally, a rate equation model is used to determine the effects of this process on the lasing dynamics and efficiency in this material and the physical parameters needed for determining whether the ESA of pump photons will be an important process in a particular host material are identified.

CHAPTER II

THEORETICAL BACKGROUND

The optical properties of materials that contain rare-earth ions have long been studied. Excellent reviews of the optical properties of rare-earths can be found in Ref. [5–8]. Early workers, especially J. Becquerel, observed that at low temperatures the optical absorption spectra of rare-earth salts consisted of numerous sharp lines. Understanding of the origin of these sharp radiative transitions was furthered by the development of crystal field theory, by H. Bethe and H. A. Kramers for example, and by J. H. Van Vleck, who suggested that the transitions were due to a forced electric dipole mechanism and occurred between states in the $4f^n$ electronic configuration.(see the extensive discussions of this early work in Ref. [6] and [8]) For a free ion radiative transitions within a configuration were known to be forbidden since the initial and final states have the same parity. Van Vleck proposed that such a transition becomes allowed when the ion is placed in a host material because of an interaction with the local electric field produced by the surrounding ligand ions.

Detailed analysis of the spectra and relaxation mechanisms in rare-earth doped materials followed this early work. The energy levels and transitions observed in the absorption and emission spectra of rare-earth materials were identified and characterized (see for example Ref. [6,7]) and a phenomenological model describing the radiative transitions was developed.[9,10] Various non-radiative relaxation mechanisms, including multiphonon relaxation [8,11–13] and non-radiative interactions between two or more ions (see reviews in Refs. [14–17]), were also identified and studied. A brief summary of some of the important results will be given here.

Energy Levels

As mentioned previously, the sharp line structure that appears in the absorption and emission spectra of rare-earth materials is produced by transitions which occur between electronic states arising from the optically active 4f electrons. The electronic configuration for atoms in the lanthanide series is $[1s^2 2s^2 2p^6 3s^2 3p^6 3d^{10} 4s^2 4p^6 4d^{10} 5s^2 5p^6 6s^2] + 4f^N$ where N varies from 2 for Ce to 14 for Yb. In the trivalent ion form, RE^{3+}, the two 6s electrons and one of the 4f electrons are ionized, leaving the lowest energy electronic configuration as $[1s^2 2s^2 2p^6 3s^2 3p^6 3d^{10} 4s^2 4p^6 4d^{10} 5s^2 5p^6] + 4f^n$. Interactions between the optically active $4f^n$ electrons, through Coulombic repulsion and spin-orbit coupling, and interaction with the host material, through the static crystal field, lead to a complex set of electronic states with differing energies. By applying the tensor operator methods developed by Racah and Judd[18], the energy level structure of the trivalent rare-earths can be quantitatively understood in terms of these interactions.[6,7] A brief summary of the approach and its results are given here.

The energy level structure involved arises primarily from three interactions: the Coulombic repulsion between electrons, spin-orbit coupling and the electric field due to surrounding hosts ligands. The Hamiltonian for the optically active 4f electrons is written as

$$H = H_o + H_{Coul} + H_{SO} + H_{SCF}. \tag{1}$$

H_o contains the kinetic energy and nuclear potential term for each of the 4f electrons,

$$H_o = \sum_{i=1}^{n} -\frac{p_i^2}{2m_i} - \frac{Z_{eff}e^2}{r_i} \tag{2}$$

where e is the electronic charge, Z_{eff} is the effective potential due to the nucleus and core electrons, i indexes the optically active 4f electrons, p_i, r_i and m_i are the momentum operator, the position operator and the mass of the i^{th} 4f electron. The summation is over all the optically active 4f electrons. The Coulombic repulsion

energy is given by

$$H_{Coul} = \sum_{i<j}^{n} \frac{e^2}{r_{ij}} \tag{3}$$

where r_{ij} is the position operator between the i^{th} and j^{th} electrons. The spin-orbit interaction is

$$H_{SO} = \sum_{i=1}^{n} \xi(r_i) s_i \cdot l_i \tag{4}$$

where $\xi(r_i)$ is the spin-orbit coupling strength and s_i and l_i are the spin and orbital angular momentum operators, respectively, for the i^{th} electron. Finally, the interaction with the surrounding host (the static crystal field) is

$$H_{SCF} = \sum_{q,k,i} B_q^k \left[C_q^k\right]_i \tag{5}$$

where the B_q^k are crystal field parameters, the C_q^k are spherical tensor operators and once again the sum is over the optically active 4f electrons. The exact form of the crystal field, which C_q^k operators are present and the values of the B_q^k's, is determined by the symmetry of the rare-earth site in the lattice and the strength of the interaction with the surrounding ligands. For rare-earth ions in the materials considered here $H_{SCF} < H_{SO} < H_{Coul}$ with energies of $\approx$100 cm^{-1}, $\approx$1000 cm^{-1} and $\approx$10000 cm^{-1} , respectively. A diagram showing the effects of these interactions is shown in Figure 1. Note that this approach ignores any configuration mixing, many body effects or relativistic effects.

The diagonalization of the Hamiltonian to produce the appropriate eigenvalues and eigenstates is usually approached in three steps. First, the central field approximation is made, combining H_o and H_{Coul} into a single central effective potential treating the Coulombic repulsion as a small perturbation. This yields states characterized by the quantum numbers S, L, M_S and M_L where the energy of the state is dependent only upon L. Using spectroscopic notation these states are labeled as the ^{2S+1}L terms.

Application of the next interaction, the spin-orbit coupling, to these states has two important results. First, part of the degeneracy of the various ^{2S+1}L terms is lifted yielding states that are $2J+1$ degenerate. These states are labeled

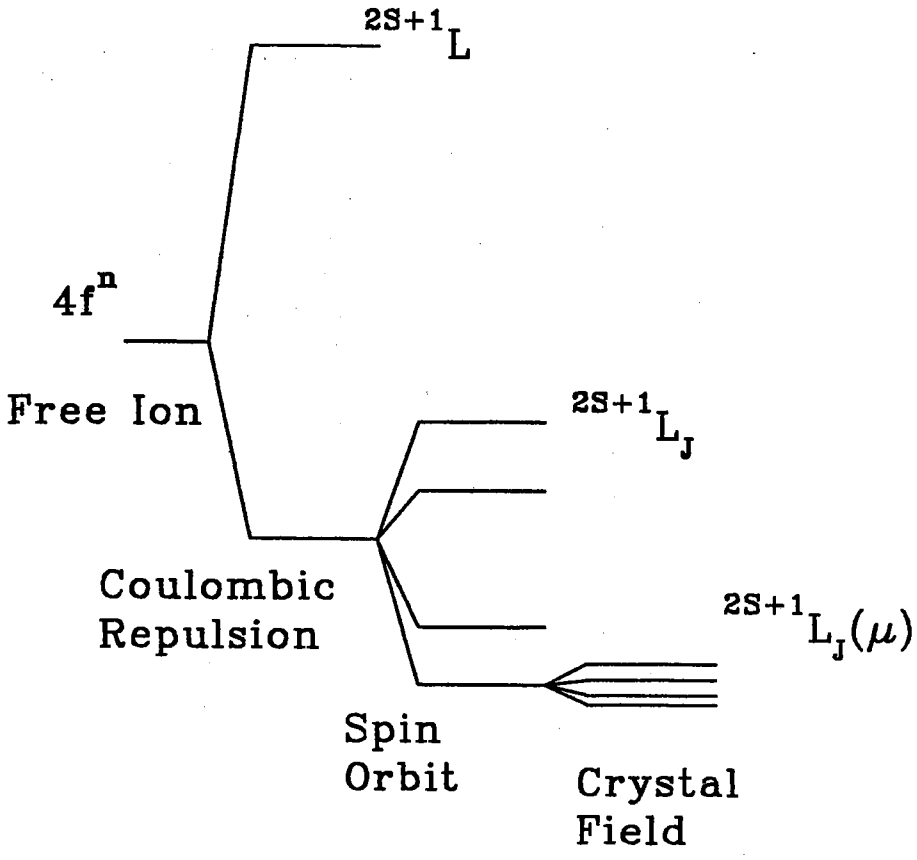

Figure 1. Rare-Earth Ion Energy Level Splittings.

as the $^{2S+1}L_J$ multiplets (the energies are independent of the quantum number J_z). These are the familiar LS coupled or Russell-Saunders states. The second result of applying the spin-orbit interaction is that it mixes states with different values of S and L but having the same value of J. The result of this J-mixing is that S and L are no longer "good" quantum numbers. The spin-orbit coupled states are linear combinations of the Russel-Saunders states:

$$| \gamma 4f^n[S,L]J >= \sum_{\gamma SL} C(\gamma SL) \mid \gamma 4f^n SLJ > \tag{6}$$

where γ represents any other quantum numbers needed to identify the state and the $C(\gamma SL)$ are coefficients dependent upon the strengths of the spin-orbit and Coulombic interactions. This is called the intermediate coupling scheme since the resulting wavefunctions are neither pure LS coupled states nor pure jj coupled states. The $[S,L]$ notation on the left hand side is used as a reminder that although S and L are still used to denote the states, they are no longer good quantum numbers and instead only represent the dominant ^{2S+1}L term in the linear combination.

The interaction with the static crystal field is considered next and like the case of spin-orbit coupling two effects are observed. First, the static crystal field removes part of the $2J+1$ degeneracy of the $^{2S+1}L_J$ multiplets producing crystal field states, also called Stark levels, which are often labeled as $^{2S+1}L_J(\mu)$ where μ is a quantum number associated with the crystal field symmetry (for example, an irreducible representation). The second effect of the static crystal field is that it causes mixing of states with the same value of μ but having different J values. Thus J is no longer a good quantum number and the final result are states of the form

$$| \gamma 4f^n[S,L,J]\mu >= \sum_{\gamma SL} C(\gamma SLJJ_z) \mid \gamma 4f^n SLJJ_z > . \tag{7}$$

where the $C(\gamma SLJJ_z)$ are dependent on the strength of the crystal field in addition to the strengths of the other interactions. Although S, L and J are still used to label the states, it is understood that only μ is a good quantum number and the

other quantum numbers on the left hand side of the equation (S, L and J) simply represent the dominant multiplet in the linear combination.

The procedure outlined above is carried out in practice by comparison to experiment since at present *ab initio* calculations of the energy levels are complicated by difficulties in calculating the actual crystal field strengths and radial wavefunctions. Furthermore, the calculations can only be done for host materials where the symmetry of the rare-earth site is well defined. In glass materials, for example, the site to site variations in the static crystal field strength and symmetry causes inhomogeneous broadening and a detailed analysis of the Stark level structure is not generally possible. In materials where the calculations are possible, the strengths of the interactions outlined above, and in some cases interactions accounting for additional relativistic and three-body effects, are parameterized and determined by a best fit to experimental data, yielding the eigenvalues (the state energies) and eigenvectors (the electronic wavefunctions) of the system.

Transition Mechanisms

Transitions between the states responsible for the optical spectra in a rare-earth ion/host system occur through a variety of mechanisms. The three dominant mechanisms in rare-earth doped materials are forced electric dipole transitions, multiphonon transitions and non-radiative energy transfer. These mechanisms are often separated into two categories: radiative and non-radiative processes. The former involve absorption or emission of a photon for energy conservation and produce the observed absorption and emission spectra while the latter involve either exchange of energy with the host lattice or energy transfer to other ions in the system.

Radiative Transitions

First consider electric dipole radiative transitions between a pair of electronic states. The transition probability rate for such a transition is governed by Fermi's

rule and involves the matrix element containing the electric dipole operator. The electric dipole matrix element is written as

$$M_{ed} = < \Psi_F \mid \mathbf{P} \mid \Psi_I > \tag{8}$$

where $\mid \Psi_F >$ is the wavefunction of the final state, $\mathbf{P}$ is the electric dipole operator and $\mid \Psi_I >$ is the wavefunction of the initial state. The electric dipole operator connects states with opposite parity. In the case of transitions between the states derived in the previous section, the matrix element in Equation (8) is zero and the transition is said to be forbidden since both states arise from the $4f^n$ configuration and therefore have the same parity.

As mentioned previously, Van Vleck suggested that the optical transitions observed in rare-earth materials were due to forced electric dipole transitions. He noted that odd symmetry components of the crystal field mixed states of opposite parity into the $4f^n$ states (configuration mixing). This mixing, ignored in the previous calculation of the energy levels and wavefunctions, provided the initial and final states with some components of opposite parity causing the transition rate to be non-zero. In 1962, B. R. Judd[9] and G. S. Ofelt[10] independently developed similar phenomenological models to explain and quantify this interaction. Detailed descriptions of the Judd-Ofelt theory can be found in [5,8,16,19] and only an outline is given here.

The approach taken by the Judd-Ofelt theory is a straightforward application of perturbation theory. Odd order terms in the crystal field Hamiltonian (designated by $\mathbf{V_{CF}}$) are used as a perturbation causing admixing of states with opposite parity to the initial $4f^n$ states. Using 1^{st} order perturbation theory the new state is given by

$$\mid \Psi_A > = \mid \Phi_A > - \sum_B \frac{< \Phi_B \mid \mathbf{V_{CF}} \mid \Phi_A >}{E_A - E_B} \mid \Phi_B > \tag{9}$$

where $\mid \Phi_B >$ and E_B are the wavefunction and energy of a state arising from a higher lying configuration, $\mid \Phi_A >$ and E_A are the wavefunction and energy of a state arising from the $4f^n$ configuration and the summation is over all states from configurations having parity opposite that of the $4f^n$ configuration.

The electric dipole matrix element can be written using states described as in Equation (9) with $\mid \Psi_I >$ as the initial state where $\mid \Phi_A > \rightarrow \mid \Phi_I >$ and $\mid \Psi_F >$ as the final state where $\mid \Phi_A > \rightarrow \mid \Phi_F >$.Writing the electric dipole matrix element using these states yields

$$\begin{aligned} < \Psi_F \mid \mathbf{P} \mid \Psi_I > = & < \Phi_F \mid \mathbf{P} \mid \Phi_I > - \sum_B \frac{<\Phi_F \mid \mathbf{V_{CF}} \mid \Phi_B><\Phi_B \mid \mathbf{P} \mid \Phi_I>}{E_F - E_B} \\ & - \sum_B \frac{<\Phi_F \mid \mathbf{P} \mid \Phi_B><\Phi_B \mid \mathbf{V_{CF}} \mid \Phi_I>}{E_I - E_B} \\ & + \sum_B \frac{<\Phi_B \mid \mathbf{V_{CF}} \mid \Phi_I>}{E_I - E_B} \sum_B \frac{<\Phi_F \mid \mathbf{V_{CF}} \mid \Phi_B>}{E_F - E_B} < \Phi_B \mid \mathbf{P} \mid \Phi_B > \end{aligned} \tag{10}$$

This can be simplified to

$$\begin{aligned} < \Psi_F \mid \mathbf{P} \mid \Psi_I > = & - \sum_B \frac{<\Phi_F \mid \mathbf{V_{CF}} \mid \Phi_B><\Phi_B \mid \mathbf{P} \mid \Phi_I>}{E_F - E_B} \\ & - \sum_B \frac{<\Phi_F \mid \mathbf{P} \mid \Phi_B><\Phi_B \mid \mathbf{V_{CF}} \mid \Phi_I>}{E_I - E_B} \end{aligned} \tag{11}$$

where the matrix elements formed between states of the same parity have been set equal to zero. The major contribution of Judd and Ofelt involves the simplification of this expression.

The major assumptions involved are as follows: the states arising from the opposite parity configurations are degenerate, $E_1 = E_2 = E_B$, and the energy differences between the states arising from the higher energy configurations and the states arising from the $4f^n$ configuration are nearly equal: $E_I - E_B \approx E_F - E_B$. The first of these assumptions allows the use of closure the simplify the summation over B while the second assumption allows the two terms in Equation (11) to be combined into a single term. The resulting equation can be further simplified by summing over the Stark levels of the upper and lower multiplets. The result is usually written in terms of the electric dipole linestrength for multiplet to multiplet transitions, S_{ed}, which is proportional to the square of the matrix element and written as

$$S_{ed}[\mid [S,L]J >, \mid [S',L']J' >] = e^2 \sum_{t=2,4,6} \Omega_t \left| < [S,L]J \left\| U^t \right\| [S',L']J' > \right|^2 . \tag{12}$$

The doubly reduced tensor operators $< [S,L]J \| U^t \| [S',L']J' >$ are usually considered to be host invariant and have been calculated and tabulated by Carnall,

Crosswhite and Crosswhite. [20] All of the constants, radial integrals and other factors have been absorbed into the Judd-Ofelt parameters, the Ω_t's.

The probability rate for an electric dipole transition from the $\mid [S,L]J >$ multiplet to the $\mid [S',L']J' >$ multiplet is related to the linestrength and can be written as

$$A[\mid [S,L]J >, \mid [S',L']J' >] = \frac{64\pi^4}{3h(2J+1)\lambda_p^3}\chi_{ed}S_{ed}[\mid [S,L]J >, \mid [S',L']J' >] \quad (13)$$

where n is the index of refraction, e is the electron charge, λ_p the wavelength of the transition, and χ_{ed} is the local field correction for the rare-earth in the initial manifold given by

$$\chi_{ed} = \frac{n(n^2+2)^2}{9}. \quad (14)$$

The radiative lifetime of an $\mid [S,L]J >$ multiplet, τ_{rad}, is related to the radiative decay rate through

$$\frac{1}{\tau_{rad}} = \sum_{[S',L']J'} A[\mid [S,L]J >, \mid [S',L']J' >] \quad (15)$$

where the summation is over all lower energy multiplets. A branching ratio for an electric dipole transition from the $\mid [S,L]J >$ multiplet to the $\mid [S',L']J' >$ multiplet can also be defined as

$$\beta[\mid [S,L]J >, \mid [S',L']J' >] = A[\mid [S,L]J >, \mid [S',L']J' >]\tau_{rad}. \quad (16)$$

The branching ratio for a transition is a measure of the relative intensity of a transition to the total intensity of all the transitions originating on a given multiplet. Another important quantity, the oscillator strength of a transition, can be written as

$$f[\mid [S,L]J >, \mid [S',L']J' >] = \frac{8\pi m\nu}{3h(2J+1)e^2n^2}\chi_{ed}S_{ed}[\mid [S,L]J >, \mid [S',L']J' >] \quad (17)$$

where m is the electron mass, and ν is the frequency of the transition.

The Judd-Ofelt parameters for a given rare-earth ion/host combination are determined by fitting experimentally calculated oscillator strengths for transitions from the ground state multiplet to the excited state multiplets to those found by Equation (17). The oscillator strength of a multiplet to multiplet transition is found from the absorption spectra using

$$f[|\,[S,L]J>,|\,[S',L']J'>] = \frac{mc}{\pi e^2 N}\int \alpha(\nu)d\nu \qquad (18)$$

where N is the concentration of rare-earth ions in the sample, $\alpha(\nu)$ is the absorption coefficient at frequency ν and the integral is over frequency range of the transition. Once the Judd-Ofelt parameters are determined from the fitting procedure, the radiative lifetimes of excited states and oscillator strengths for transitions between excited states can be calculated.

Non-Radiative Transitions: Multiphonon Decay

A second mechanism for transitions in rare-earth ion/host systems involves an interaction between the rare-earth ion and the lattice through the exchange of one or more phonons. Very fast transitions involving a small number of lattice phonons occur between the crystal field split Stark levels within a multiplet. These transitions lead to a Boltzman distribution of excited ions within a multiplet and can account for the experimentally measured linewidths of the optical transitions. In addition to these processes, however, there are multiphonon processes that occur on the same time scale as radiative transitions. These processes involve a large number of high energy phonons to provide energy conservation for a transition between a pair of Stark levels from two different multiplets.

Although multiphonon decay in rare-earth materials has been extensively studied,[6,8,12,13,16,21,22] a complete theory describing multiphonon relaxation has not been fully developed. A general theoretical approach and a phenomenalogical model have been established however.(see for example [8,16]) Multiphonon decay is possible through an interaction between the electronic-vibrational states

of the rare-earth ion/lattice system. These states are written as

$$| \Psi_{a,i,j,k...} >=| \Psi_a >| n_i n_j n_k... > \tag{19}$$

where $| \Psi_a >$ is the electronic wavefunction, $| n_i n_j n_k... >$ is the wavefunction describing the lattice and the n_i's are the occupation numbers of the phonon modes of the lattice. The interaction mechanism is the dynamic crystal field which can described by a Hamiltonian of the form

$$H_{DCF} = \sum_i Q_i V_i + \frac{1}{2} \sum_{i,j} Q_i Q_j V_{ij} + ... \tag{20}$$

where the Q_i's are the normal mode coordinates and the $V_{i...}$'s are electron-phonon coupling strengths. Typical theoretical approaches involve the use of nth order perturbation theory using the first order term in the crystal field expansion or use 1st order perturbation theory with the nth order term in the crystal field expansion. In either case since the exact coupling between the rare earth ion and the lattice is not well known, *ab initio* calculations are difficult.

Empirically, multiphonon relaxation rates are found to depend on the temperature of the sample and the energy separation between multiplets.[8,12,22] A multiphonon decay rate is found by comparing the measured fluorescence lifetime, τ_{meas}, with the radiative rate predicted by the Judd-Ofelt theory described previously, τ_{rad}. In the absence of any other interactions the measured and predicted radiative lifetimes are related by

$$\frac{1}{\tau_{meas}} = \frac{1}{\tau_{rad}} + W_{mp} \tag{21}$$

where W_{mp} is the multiphonon decay rate. Mutiphonon decay rates for different transitions in a given host are found to depend exponentially on the energy gap separating the upper and lower multiplets. This relation is known as the energy gap law and is given by

$$W_{mp} = C \exp(-\alpha \Delta E) \tag{22}$$

where C and α are host material dependent and ΔE is the energy gap between the upper and lower multiplets involved in the transition.

Phenomenologically, the energy gap law can be understood using a single frequency phonon model. An energy gap ΔE can be bridged by n high energy phonons of frequency ω so $n = \Delta E/\hbar\omega$. For an n^{th} order perturbation approach to be valid, the n^{th} order term must be smaller than the $(n-1)^{th}$ order term:

$$\frac{W_n}{W_{n-1}} = \epsilon \ll 1 \tag{23}$$

If the ratio between W_n and W_{n-1} is nearly constant for all n then

$$W_n = C\epsilon^n \tag{24}$$

which can be rewritten as

$$W_n = C\exp(-\alpha\Delta E) \tag{25}$$

Once C and α are known for a given host, the energy gap law can be used to determine the rate for multiphonon transitions in the material. One important factor to note, however, is that the energy gap law has been found to be valid only for cases where large numbers of phonons are involved. For small energy gaps, where only one or two high energy phonons are needed, the energy gap law no longer holds and can significantly underestimate the decay rates. Investigation of non-radiative relaxation rates between closely spaced multiplets is still an important area of research in rare-earth materials.[23–27]

Non-Radiative Decay: Ion-Ion Energy Transfer

A third mechanism responsible for multiplet to multiplet transitions in rare-earth ions is non-radiative energy transfer.(see Refs. [8,14–17]) In this type of process an ion in an excited state transfers some or all of its energy to another nearby ion which is originally in either its ground state or an excited state without involving either emission or absorption of a photon. Three examples of energy transfer processes are shown in Figure 2. Figure 2(a) shows an example of energy transfer from an ion of type s, a sensitizer, to an ion of type a, an activator. The sensitizer relaxes to its ground state promoting the activator to its excited state. In situations where this process occurs, the fluorescence emission intensity and

measured fluorescence lifetime of the sensitizer are both reduced (or quenched) in the presence of activators. If the activators luminesce, this type of process is referred to as sensitized luminescence since emission is seen from a type of ion that does not directly absorb the pump energy. Early work in this field can be found in Refs. [28–30]. Figure 2(b) shows a second energy transfer process in which one excited sensitizer ion relaxes to the ground state transferring its energy to another sensitizer ion that was initially in the ground state. This process does not lead to luminescence quenching but it can be responsible for spatial energy migration in which energy is transferred from one location in the crystal to another. Long range energy transfer of this type can be studied using laser induced grating spectroscopy.[31–33] The third type of process shown (Figure 2(c)) is an example of an energy transfer upconversion process in which two ions in excited states interact, one ion relaxing to the ground state and the other being promoted to a higher lying level. This type of process can, for example, convert infrared excitation into visible emission and is one process often present in upconversion laser systems.[34,35] The processes represented in Figure 2(a) and Figure 2(c) are examples of spectral energy transfer processes since their effects can be detected by monitoring changes in the spectral content of the emission.

The study of energy transfer has been an extremely important part of the understanding of the optical properties of rare-earth doped materials.(see for example Ref. [8,14,15,17] Two somewhat different mathematical approaches for studying energy transfer have been developed and used: a macroscopic rate equation approach and a microscopic ion-ion interaction approach. The microscopic approach, in which interactions between pairs of ions are considered, is discussed below while the rate equation approach, which is formally the same as the rate equation approach used to describe laser systems, will be described in the next section. The relationship between these two approaches and the limitations of each approach are discussed in detail in Ref. [36].

A starting point for any discussion of the microscopic approach to nonradiative energy transfer must be the pioneering work of Forster [28] and the

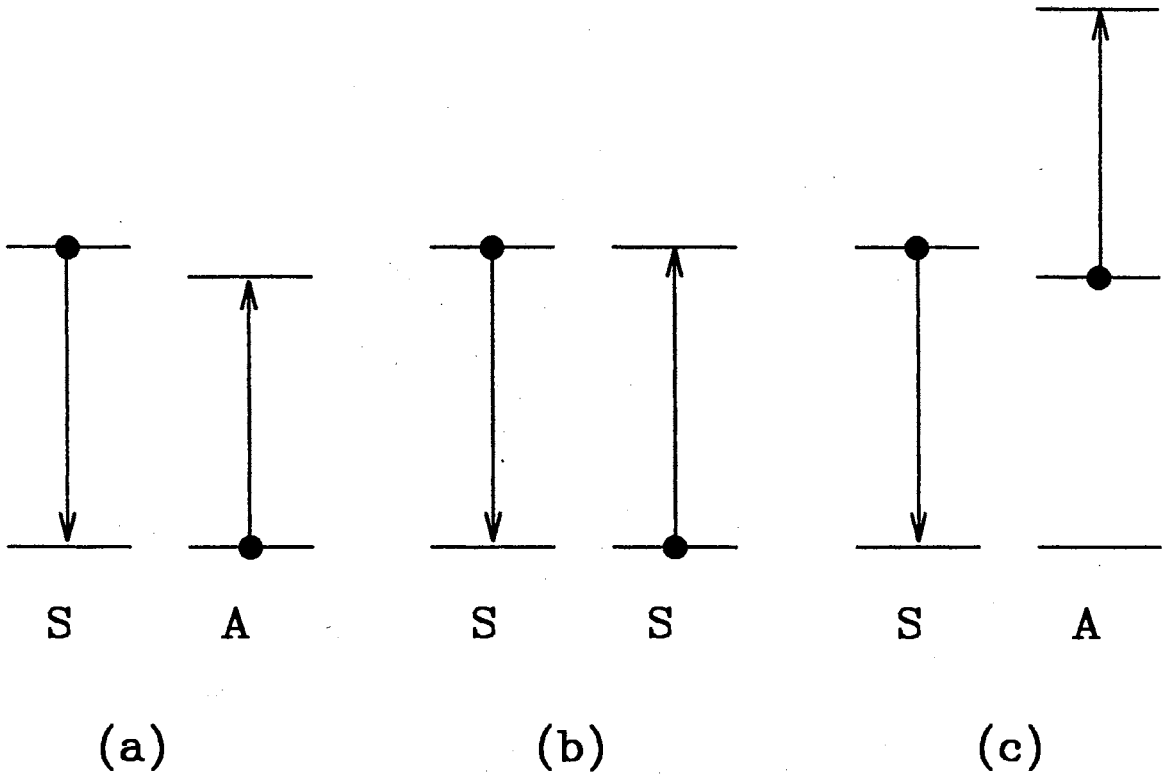

Figure 2. Examples of Energy Transfer Processes. (a) Sensitizer to Activator Energy Transfer (b) Senesitizer to Sensitizer Energy Transfer (c) Upconversion Energy Tranfer.

continuation of this work by Dexter [29]. Forster-Dexter theory provides a simple method of calculating the energy transfer rate from a sensitizer ion to an activator ion with a given spatial separation using the observed emission and absorption spectra of the ions involved. Extensions to this basic theory provide a formalism to understand to more complex systems with many sensitizer and activator ions distributed in the host media [28,30,37] (Reviews in Refs.[8,14,15,17]). The brief review of the Forster-Dexter theory given here parallels the development by Dexter in [29].

A probability rate for energy transfer between two ions as shown in Figure2(a) can be written as follows

$$P_{sa} = \frac{2\pi}{\hbar} |< \Psi_i \mid H_{ij} \mid \Psi_f >|^2 g_e. \tag{26}$$

where $\mid \Psi_i >$ is the wavefunction of the initial state given by

$$\mid \Psi_i >= \mid \Psi(\mathbf{r_s}, E_{se}), \Psi(\mathbf{r_a}, E_{ag}) > \tag{27}$$

where the sensitizer ion at $\mathbf{r_s}$ in the excited state (energy=E_{se}) is described by the wavefunction $\Psi(\mathbf{r_s}, E_{se})$ and the activator ion at $\mathbf{r_a}$ in the ground state (energy=E_{ag}) is described by the wavefunction $\Psi(\mathbf{r_a}, E_{ag})$. The wavefunction of the final state is

$$\mid \Psi_f >= \mid \Psi(\mathbf{r_s}, E_{sg}), \Psi(\mathbf{r_a}, E_{ae}) > \tag{28}$$

where the sensitizer ion at $\mathbf{r_s}$ in the ground state (energy=E_{sg}) is described by the wavefunction $\Psi(\mathbf{r_s}, E_{sg})$ and the activator ion at $\mathbf{r_a}$ in the excited state (energy=E_{ae}) is described by the wavefunction $\Psi(\mathbf{r_a}, E_{ae})$. g_e is the density of states of the final state and H_{ij} is the Hamiltonian describing the interaction between the i^{th} and j^{th} ions.

The form of H_{ij} depends upon the type of interaction considered, electric dipole-dipole, electric dipole-quadrupole, exchange, etc. For simplicity, consider only the electric dipole-dipole interaction so

$$H_{ij} = \left[\mathbf{r_s} \cdot \mathbf{r_a} - \frac{3(\mathbf{r_s} \cdot \mathbf{R_{sa}})(\mathbf{r_a} \cdot \mathbf{R_{sa}})}{\mathbf{R_{sa}}^2}\right] \frac{e^2}{R_{sa}^3} \tag{29}$$

where $\mathbf{R_{sa}}$ is the vector connecting the two ions. The matrix element involving this interaction can be evaluated and, using the Einstein A and B coefficients, related to the observed absorption and emission spectra. This yields

$$P_{sa}^{dd} = \frac{3\hbar^4 c^4}{4\pi n^4} \frac{Q_a}{\tau_s R_{sa}^6} \left(\frac{\mathcal{E}}{\sqrt{\epsilon}\mathcal{E}_c} \right)^4 \int \frac{f_s(E) F_a(E) dE}{E^4} \tag{30}$$

where Q_a is the absorption strength given by $Q_a = \int \sigma(E) dE$ where $\sigma(E)$ is the absorption cross section of the activator at energy E, f_s is the normalized emission spectrum of the sensitizer, $F_a(E)$ is the normalized absorption spectrum of the activator, τ_s is the radiative lifetime of the excited state of the sensitizer (in the absence of the activator), $\mathcal{E}/\mathcal{E}_c$ is the ratio of the applied electric field intensity to that in the crystal, and ϵ is the dielectric constant. This is often written in terms of a critical interaction distance, R_o, as

$$P_{sa}^{dd} = \frac{1}{\tau_s} \left(\frac{R_o}{R_{sa}} \right)^6 \tag{31}$$

with

$$R_o \equiv \left(\frac{3\hbar^4 c^4}{4\pi n^4} Q_a \left(\frac{\mathcal{E}}{\sqrt{\epsilon}\mathcal{E}_c} \right)^4 \int \frac{f_s(E) F_a(E) dE}{E^4} \right)^{1/6} . \tag{32}$$

The critical interaction distance is the separation between a sensitizer and an activator that produces an energy transfer rate equivalent to the intrinsic radiative decay rate of the sensitizer. More importantly, the critical interaction distance can be determined from experimentally measured spectra: the absorption spectrum of the activator and the emission spectrum of the sensitizer.

As mentioned previously, the formalism above describes the energy transfer rate between a pair of ions. The extension to a somewhat more realistic material system, in which there are a large number of sensitizer and activator ions can be found in the work of Forster [28] and of Inoukuti and Hirayama [30]. In this approach, each activator ion in the system contributes to the decay of the sensitizer. The observed decay time, in the absence of other decay processes, is given by

$$\rho_s(t) = \exp\left[-\frac{t}{\tau_s} - \frac{t}{\tau_s} \sum_{i=1}^{N} \left(\frac{R_o}{R_i} \right)^6 \right] \tag{33}$$

where R_i is the distance to the i^{th} activator and N is the number of activators. To determine the average decay rate of all the sensitizers in the system the rate is averaged over a random distribution of activators, $\rho_a(R_i)$, giving

$$\overline{p}_s(t) = \exp\left[-\frac{t}{\tau_s} - \frac{t}{\tau_s}\prod_{i=1}^{N}\int_V \left(\frac{R_o}{R_i}\right)^6 \rho_a(R_i)dV\right] \tag{34}$$

This can be evaluated in the limit as $N\&V \rightarrow \infty$ such that $N/V \rightarrow N_a$, the concentration of activators. The average decay in this limit is then given by

$$\overline{p}_s(t) = \exp\left[-\frac{t}{\tau_s} - \frac{N_a}{N_o}\Gamma(1/2)\sqrt{\frac{t}{\tau_s}}\right]. \tag{35}$$

where N_o is the critical concentration given by $N_o = \frac{4\pi}{3}(R_o)^3$. This type of decay is known as static or Forster decay.

One of the assumptions in the derivation of the static decay is that no interaction between sensitizer ions occurs, that is, there is no sensitizer to sensitizer energy transfer. Although developed above for two different types of ions, Forster-Dexter theory can be applied even if the ions are of the same type. In this case one "sensitizer" ion transfers its energy to another "sensitizer" ion. In many systems the concentration of sensitizers is large enough for sensitizer-sensitizer interaction to be significant. R_{ss}, the distance between two sensitizers which will replace R_{sa} in Equation (31), becomes small so the interaction rate for the process in Figure 2(b) is large. This may lead to spatial migration of energy in the excited state of the sensitizer. A wide variety of methods for describing sensitizer to sensitizer energy migration have been developed, including formalisms based on solving the diffusion equation [38], random walk approaches [37,39] and a generalized master equation approach [40].

To treat the most general case in which both energy migration and sensitizer-activator energy transfer occurs, different formalisms have been developed.(see for example Refs. [37,41] and the reviews) Often, these approaches yields results in which each of the energy migration steps (sensitizer to sensitizer energy transfer steps) is treated using Equation (31). Each of the approaches, however, is faced with limitations on its applicability due to the assumptions that must be made,

especially assumptions related to the distribution of ions in the host and the possibility of energy transfer from "activators" to "sensitizers", called back transfer. To avoid these problems, numerical approaches using Monte Carlo simulations have been carried out.[42] Overall the problem of energy transfer in rare-earth doped materials is an extremely complex one and the brief discussion of some of the single-step energy transfer processes above introduces the concepts and terminology used in the discussions of the systems considered later in this work.

Rate Equation Modeling

In the previous sections the various mechanisms for transitions between the levels of rare-earths have been discussed. These rates describe the decay of and excitation of ions from one state to another. A common approach for describing population dynamics in multi-level systems, often used to describe laser systems and energy transfer, involves the use of semiclassical rate equations. Formally, the semiclassical rate equation approach is related to the population density matrix formalism used in quantum mechanics in the limit that the dephasing time (or dipole decay time) is short compared to the time scale on which the populations of the levels evolve. Discussions of rate equations and their use in the study of laser systems and energy transfer can be found in [5,14,15,36,43,44]

Using the rate equation approximation, the time evolution of the population density of the i^{th} level of a multi-level system is written as

$$\frac{dn_i}{dt} = \sum_E W_E(n_i, n_j, \Phi_k, t...) - \sum_R W_R(n_i, n_j, \Phi_k, t, ...) \tag{36}$$

where $W_E(n_i, n_j, \Phi_k, t, ...)$ is the rate of the E^{th} process that excites ions to the level (a "pump" process) and $W_R(n_i, n_j, \Phi_k, t, ...)$ is the rate of the R^{th} relaxation process that depopulates the level. The sums are carried out over all possible excitation and relaxation processes. In general the rates may depend explicitly on the population of the i^{th} level (n_i), the populations of other levels (the n_j's), the intensities of any fields present (the Φ_k's), and the time, t. The exact forms and proportionality constants involved depend on type of process involved in each

rate. The usefulness of the rate equations for describing a given system depends on determining the important mechanisms in the system and the knowledge of the rate parameters (the proportionality constants) describing each process.

Figure 3 shows a simple system described by the following set of rate equations:

$$\dot{n}_1 = -R_{13} + R_{31} + A_{31}n_3 - k_{52}n_5n_1 + k_{25}n_2n_4 + A_{21}n_2 \tag{37}$$

$$\dot{n}_2 = +A_{32}n_3 + W_{32}n_3 - W_{23}n_2 - A_{21}n_2 - k_{25}n_2n_4 - k_{52}n_5n_1 \tag{38}$$

$$\dot{n}_3 = -\tau_3^{-1}n_3 - W_{32}n_3 + W_{23}n_2 - R_{31} + R_{13} \tag{39}$$

$$\dot{n}_4 = -k_{52}n_5n_1 + k_{25}n_2n_4 + A_{54}n_5 - R_{45} + R_{54} \tag{40}$$

$$\dot{n}_5 = +k_{52}n_5n_1 - k_{25}n_2n_4 - A_{54}n_5 - R_{54} + R_{45} \tag{41}$$

$$\dot{\Phi}_1 = +R_{54} - R_{45} + \omega_{el}n_5 - \gamma\Phi_l \tag{42}$$

The terms in these equations describe the various pump, energy transfer, relaxation and emission processes shown in Figure 3. The definitions of the symbols used are as follows:

n_i: population density of the ith level

R_{ij}: stimulated radiative transition term

W_{ij}: non-radiative multiphonon decay rate for a transition between levels i and j

τ_i: radiative lifetime of the i^{th} level

A_{ij}: radiative decay rate for a transition between levels i and j

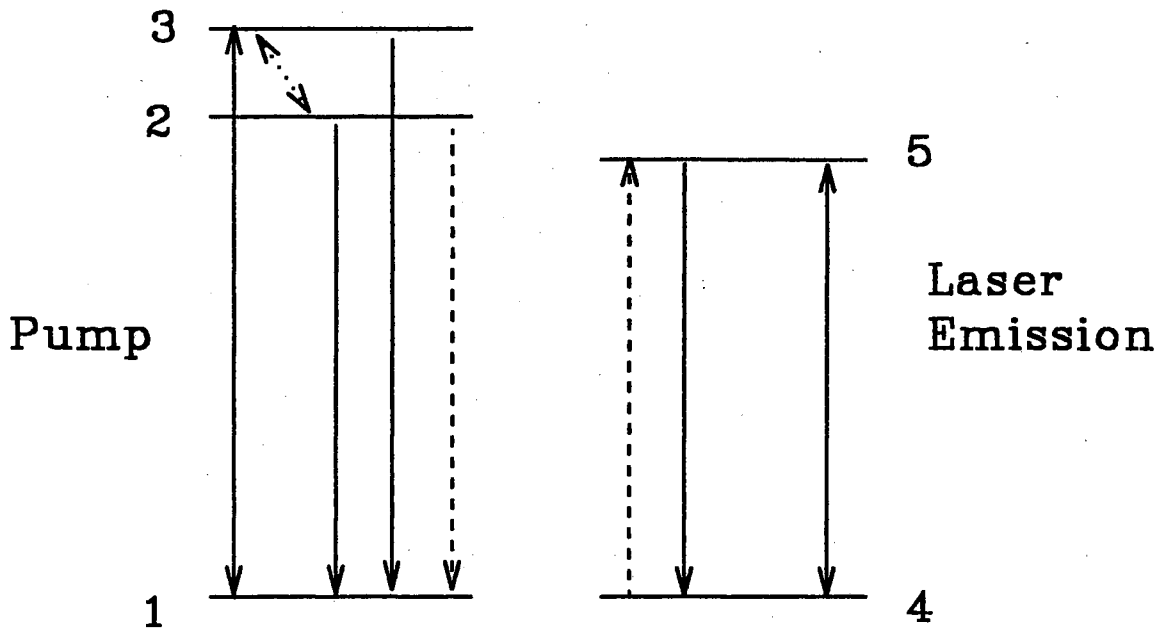

Figure 3. Example of Multi-level System. Solid Lines Represent Radiative Transitions, Dotted Line Represents Multiphonon Relaxation, and Dashed Lines Represent Energy Transfer.

k_{ij}: rate constant for a cross relaxation process in which energy is transferred from level i to level j

γ: cavity decay rate at the output wavelength of the laser

ω: factor describing spontaneous decay into the cavity at the laser wavelength

Φ_l: flux at the laser wavelength.

Each of the terms in the rate equations consists of a rate multiplying a population density or rate parameters multiplying population densities. For spontaneous radiative decay, the term consists of the decay rate, the Einstein A coefficient for the transition (the A_{ij}) or τ_i^{-1} the total radiative decay rate, and the population density of the upper level. Non-radiative multiphonon transitions are treated similarly, using the non-radiative decay rate and the population density of the level in which the transition originates. Note that these equations allow for upward non-radiative transitions along with non-radiative decay. The relation between these rates is given by the Boltzman equation

$$W_{ji} = W_{ij} \exp\left(-\frac{\Delta E_g}{kT}\right). \tag{43}$$

The terms describing the non-radiative ion-ion energy transfer processes depend on two population densities, those of the initial levels in which the two ions are found, and on a rate parameter, k_{lm}, giving the strength of the interaction. The l and the m designate one of the original levels and one of the final levels, respectively. Terms describing the stimulated radiative transitions, R_{ij}, can be written in many different forms. One common form is $R_{ij} = \Phi_r \sigma_{ij} n_i$ where Φ_r is the flux at the resonant wavelength and σ_{ij} is the cross section for the transition. Further discussion of stimulated transitions will be considered in Chapter III.

Often, the rate parameters can be determined from spectroscopic measurements. Absorption and emission spectra can be used to determine the cross sections for stimulated radiative transitions. The total radiative lifetime can be directly found experimentally or can be predicted by a Judd-Ofelt analysis of the absorption spectra, which also gives the radiative decay rates for individual transitions.

Multiphonon rates can be found using the energy gap law or from the difference between the predicted and experimentally measured lifetimes. The rate parameters for the ion-ion energy transfer processes, although in general more difficult to determine, can be found for specific cases from spectroscopic measurements. One of the major difficulties in determining these parameters is that the connection between the microscopic energy transfer models and the rate parameters in the rate equation models is not well understood. The random nature of the distribution of ions in the host material makes the calculation of transfer parameters from microscopic parameters impossible in the general case. If the energy transfer parameters and the other parameters used in the above rate equation model are known, however, the equations can be solved and the population and laser dynamics can be determined. Determining the important processes in the system and finding the parameters describing them is an important step in understanding rare-earth ion based laser systems.

CHAPTER III

SPECTROSCOPIC AND LASING PROPERTIES OF Tm,Ho:YAG

Introduction

In a recent publication [45] the lasing properties of $Y_3Al_5O_{12}$:Tm,Ho excited by an alexandrite laser were reported. Several interesting effects were observed. First, a notable (60- 200 μs) time delay was observed between the end of the pump pulse and the onset of laser emission. This delay was found to shorten as the pump intensity was increased. In addition, under these excitation conditions, fluorescence emission in the 530-565 nm spectral region was observed. The intensity of this emission was found to be dependent upon the excitation wavelength. Since this emission occurs at an energy higher than that of the pump photons it was concluded that it arose from either a sequential multiple photon absorption process or an ion-ion interaction process.

Although a significant amount of research has been done on this crystalline laser system [46–50], there are still many important questions about its optical and lasing properties that remain unanswered. Figure 4 shows the general processes involved in the optical pumping of Tm-Ho lasers. Specific values have not yet been determined for all of the physical parameters governing the optical pumping dynamics of the system. Many of the values reported for the spectral parameters have been determined using flashlamp pumping in crystals containing additional dopants such as Cr^{3+} ions.[49,51,52] Significant discrepancies exist in the literature for values of the lifetimes and rise times of various spectral features.[49–57] Computer modeling of laser operation has been accomplished only by using rough

estimates of the values of the rate parameters or by treating them as fitting parameters.[54,58]

The purpose of the work described here is to determine the values of the fundamental physical parameters necessary for a computer simulation of a Tm-Ho laser system that can accurately predict the temporal properties of the laser emission. To accomplish this, results of a spectroscopic study of the dynamics of optically pumped Tm,Ho:YAG are presented. A rate equation model of this system is used to establish values for the rate parameters governing two of the important ion-ion interaction processes. These parameters are then used in a computer model simulating an alexandrite laser pumped Tm,Ho:YAG laser system. Since the rate parameters are established from the spectroscopic data, the computer simulation has no adjustable parameters. The results of this simulation are shown to be consistent with the experimental results found previously for this system.[45]

Model

In order to understand and explain the optical dynamics of Tm-Ho doped laser materials, a model must be developed that includes several types of radiative and nonradiative transitions among the various energy levels of the two trivalent rare earth ions. Figure 4 shows the model generally used to describe diode laser pumped operation of these systems[48,49] and Figure 5 shows more complete energy level diagrams for the Tm^{3+} and Ho^{3+} ions. In a diode laser pumped Tm,Ho:YAG laser the pump laser directly excites the $^3H_4$ multiplet of Tm^{3+}. After this excitation, a number of different processes occur eventually resulting in energy being stored in the $^5I_7$ state of Ho^{3+}. These processes are as follows. The energy difference between the excited states of Tm^{3+} is such that an energy resonance occurs between the $^3H_4 \rightarrow {}^3F_4$ and $^3H_6 \rightarrow {}^3F_4$ transitions. Thus a cross relaxation process involving these transitions can occur producing two Tm^{3+} ions in the $^3F_4$ metastable state for every ion initially excited by the pump laser. Alternately, energy migration may occur in the $^3H_4$ state followed by this cross relaxation process. After the $^3F_4$ level is populated, fast energy migration among Tm^{3+} ions in

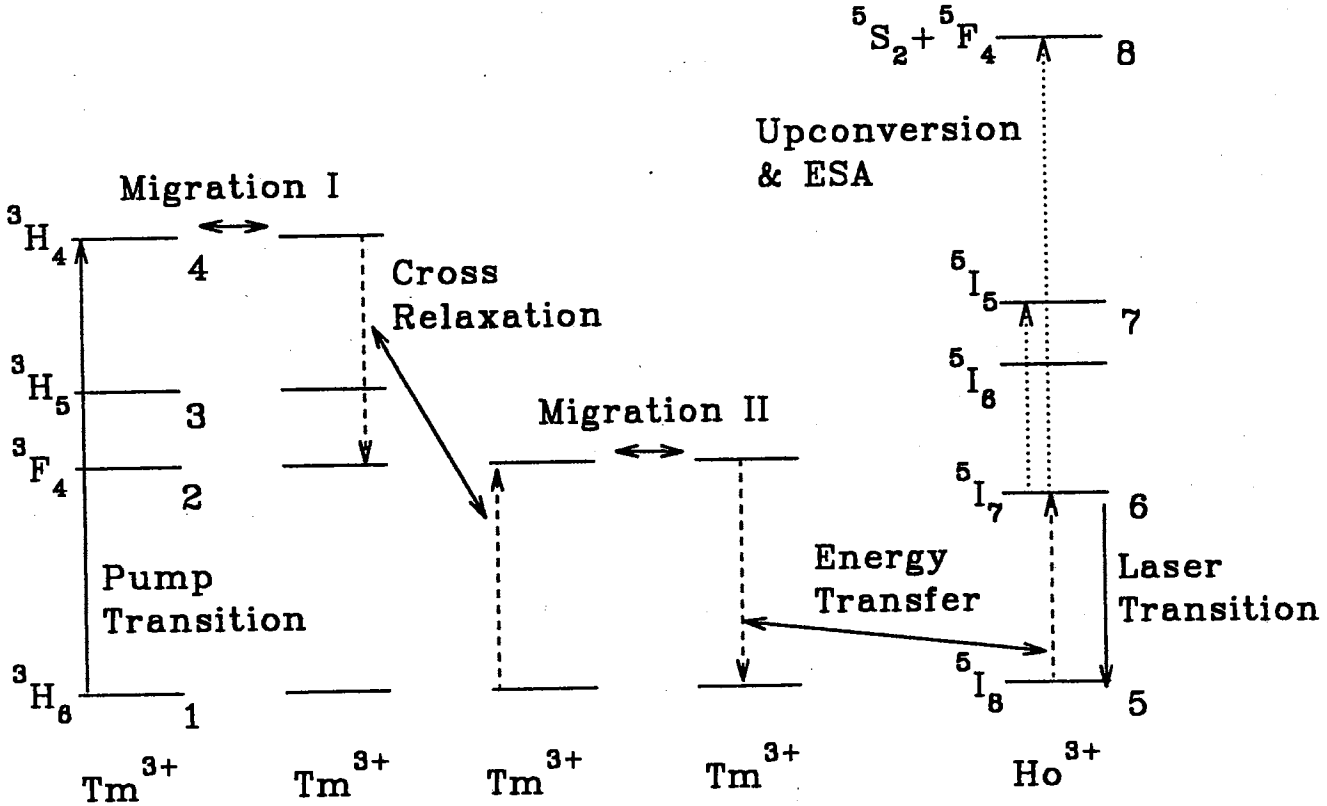

Figure 4. Energy Level Model of Diode Laser Pumped Tm,Ho:YAG Laser Systems.

the metastable state can occur. The details of this process have been described recently.[59,60] Whether energy migration among Tm^{3+} ions occurs both before and after cross relaxation is presently unclear and will be investigated here. Eventually the energy is transferred to a Ho^{3+} ion via a $^3F_4 \rightarrow {}^3H_6$, $^5I_8 \rightarrow {}^5I_7$ cross relaxation process. The $^5I_7$ multiplet is the Ho^{3+} metastable state and the initial laser level for the 2.09 μm emission seen in these systems.

Additional levels involved in transitions resulting in various loss mechanisms are also shown in Figure 4. One of these, involving the $^5F_4$ and $^5S_2$ multiplets, is often cited to explain the origin of the green emission that is often observed. In this case, an additional cross relaxation process involving the terminal level of the pumping transition and the Ho^{3+} metastable state is considered.[50] A second process that may populate the $^5F_4$ and $^5S_2$ multiplets to produce the green emission is absorption of pump photons by ions in the Ho^{3+} metastable state. The $^5I_5$ and $^5I_6$ multiplets of Ho^{3+} are involved in another possible loss mechanism. This is an upconversion process involving the metastable states of both the Tm^{3+} and Ho^{3+} ions which populates the $^5I_5$ level of Ho^{3+}. Ions excited to the $^5I_5$ multiplet relax rapidly to the $^5I_6$ multiplet followed by energy transfer to the $^3H_5$ multiplet of Tm^{3+}. This transfer process is considered to be instantaneous in the model described below and further discussion of this assumption is given later. In the equations describing the transitions involved in this model, the levels are numbered as follows: i=1 is $^3H_6$, i=2 is $^3F_4$, i=3 is $^3H_5$, i=4 is $^3H_4$, i=5 is $^5I_8$, i=6 is $^5I_7$, i=7 is $^5I_5$, and i=8 is $^5S_2$ and $^5F_5$.

The model outlined above can be mathematically described by a series of rate equations. These equations are:

$$\begin{aligned}\dot{n}_1 = &-R_{14} + R_{41} - k_{42}n_4n_1 - k_{62}n_6n_1 + k_{26}n_5n_2 \\ &+k_{48}n_4n_6 + k_{27}n_2n_6 - n_7\tau_7^{-1} + n_2\tau_2^{-1} + A_{41}n_4 - A_{31}n_3\end{aligned} \tag{44}$$

$$\begin{aligned}\dot{n}_2 = &\,2k_{42}n_4n_1 + k_{62}n_6n_1 - k_{26}n_5n_2 - k_{27}n_2n_6 \\ &-n_2\tau_2^{-1} + A_{42}n_4 + A_{32}n_3 + W_{32}n_3\end{aligned} \tag{45}$$

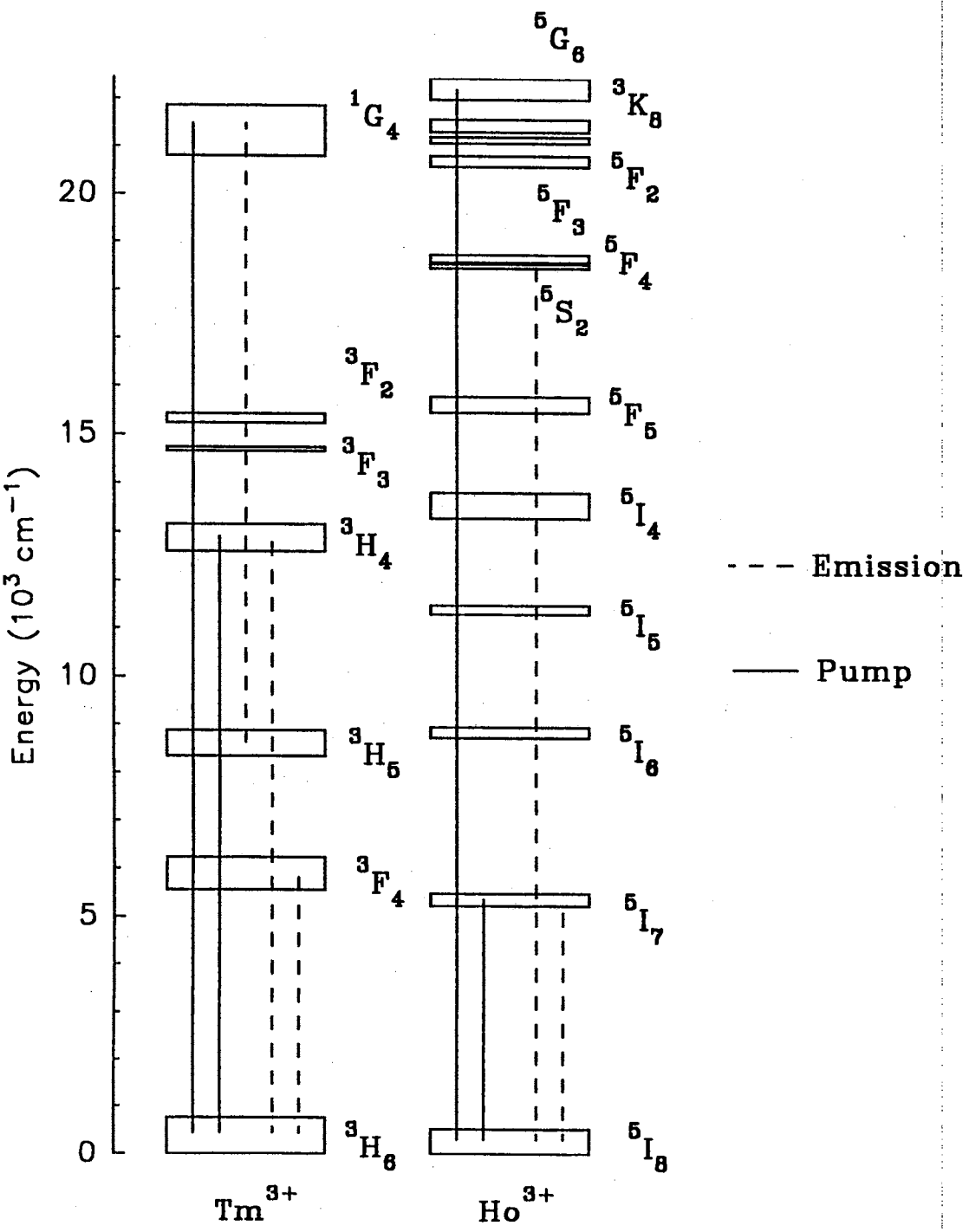

Figure 5. Energy Level Diagram of Tm^{3+} and Ho^{3+} in YAG. Pump Transitions are Designated by Solid Lines and Important Emission Transitions are Designated by Dashed Lines.

$$\dot{n}_3 = +n_7\tau_7^{-1} - n_3\tau_3^{-1} + A_{43}n_4 + W_{43}n_4 - W_{32}n_3 \tag{46}$$

$$\dot{n}_4 = +R_{14} - R_{41} + k_{42}n_4n_1 - k_{48}n_4n_6 - n_4\tau_4^{-1} - W_{43}n_4 \tag{47}$$

$$\dot{n}_5 = +R_{65} - R_{56} + k_{62}n_6n_1 - k_{26}n_5n_2 + n_6\tau_6^{-1} + n_7\tau_7^{-1} + n_8\tau_8^{-1} \tag{48}$$

$$\begin{aligned}\dot{n}_6 = &-R_{65} + R_{56} + R_{86} - R_{68} - k_{62}n_6n_1 + k_{26}n_5n_2 \\ &-k_{48}n_4n_6 - k_{27}n_2n_6 - n_6\tau_6^{-1}\end{aligned} \tag{49}$$

$$\dot{n}_7 = +k_{27}n_2n_6 - n_7\tau_7^{-1} \tag{50}$$

$$\dot{n}_8 = +k_{48}n_4n_6 - n_8\tau_8^{-1} \tag{51}$$

$$\dot{n}_p = +R_{65} - R_{56} - n_p\tau_c^{-1} + n_6\omega_{el} \tag{52}$$

The terms in these equations describe the various pump, energy transfer, relaxation, and emission processes shown in Figure 4. The definitions of the symbols used are the same as those defined in Chapter I. The density of lasing photons, n_p, is used rather than the flux at the laser wavelength and τ_c is the cavity lifetime. Additionally, ω_{el} is given by

$$\omega_{el} = \sigma_{65}c\frac{l}{l_c}. \tag{53}$$

Here σ_{65} is the stimulated emission cross section for the laser transition, c is the speed of light, l is the sample length, and l_c is the cavity length. This factor describes the stimulated emission due to one photon/cm^3 and is used to seed the cavity equation.

The terms involving stimulated emission and absorption must be examined in more detail to obtain the required expressions for the transition rates and cross

sections. Optical transitions of rare earth ions in crystals occur between the crystal field split Stark components of different multiplets. In many cases there are several transitions between different combinations of Stark levels that are within the frequency resolution of the experiment and thus can not be resolved spectroscopically. Therefore the experimentally measured spectral properties are the result of the sum of all of the possible transitions at the particular frequency of interest weighted by population and degeneracy factors. The population density rate of change due to absorption involving one of these transitions between a specific pair of Stark levels can be written as

$$R_{lu=}\Phi(\nu)\sigma_{lu}(\nu)n_l d_u \tag{54}$$

where $\Phi(\nu)$ is the photon flux at frequency ν, $\sigma_{lu}(\nu)$ is the absorption cross section for the transition between the two Stark components, n_l is the population in the lth Stark component of the lower multiplet, and d_u is the degeneracy of the upper state. The total population density rate of change at a given frequency is the sum over all Stark component transitions at that frequency

$$R_a(\nu) = \sum_{lu} \Phi(\nu)\sigma_{lu}(\nu)n_l d_u. \tag{55}$$

Note that the lineshape for the transition is contained within the cross sections for the transitions between the individual Stark components. Although the sum is carried out over all the Stark components of both the upper and lower multiplets, only those transitions with $\sigma_{lu}(\nu) \neq 0$ make an effective contribution.

The absorption cross section at frequency ν is given by[61]

$$\sigma_{abs}(\nu) = (1/Z_l) \sum_{lu} d_l \exp\left(-E_l/k_B T\right) \sigma_{lu}(\nu) d_u \tag{56}$$

where E_l is the energy of the lth Stark component (measured with respect to the lowest Stark component in the multiplet), k is the Boltzmann constant, T is temperature, d_l is the degeneracy of the lth Stark component, and Z_l is the

partition function for the lower multiplet. The partition function for a multiplet is given by

$$Z = \sum_m d_m \exp\left(-E_m/k_BT\right) \tag{57}$$

where the individual Stark components are indexed by m and the energy is measured with respect to the lowest Stark component of the multiplet. The absorption cross section can be written in terms of the Boltzmann factor, $f_l = d_l exp(-E_l/k_BT)/Z_l$, as

$$\sigma_{abs}(\nu) = \sum_{lu} f_l \sigma_{lu}(\nu) d_u. \tag{58}$$

Using $n_l = f_l n_{tl}$ where n_{tl} is the total population of the lower multiplet, Equation (55) can be written as

$$R_a(\nu) = \Phi(\nu)\sigma_{abs}(\nu)n_{tl}. \tag{59}$$

The population density rate of change for stimulated emission can be written as

$$R_e(\nu) = \Phi(\nu)\sigma_{emi}(\nu)n_{tu} \tag{60}$$

where n_{tu} is the total upper multiplet population. The relationship between $\sigma_{abs}(\nu)$ and $\sigma_{emi}(\nu)$ is

$$\sigma_{emi}(\nu) = \frac{Z_l}{Z_u} \exp\left(\frac{E_{ZL} - h\nu}{k_BT}\right) \sigma_{abs}(\nu) \tag{61}$$

where Z_u is the partition function of the upper multiplet defined as in Equation (57) , E_{ZL} is the separation between the lowest Stark components of the upper and lower multiplets, and h is Planck's constant.

In situations where the transitions between different pairs of Stark components are well separated the summation in Equation (55) reduce to a single term. The cross section for the transition is then found by dividing the absorption coefficient by the population in the lower Stark component. For this situation Equation (54) is used to describe the effects of optically stimulated transitions in the rate

equations. However, for Tm,Ho:YAG, there are numerous closely spaced Stark components for the transitions of interest [62,63] and the more complicated expressions for R_{ij} and $\sigma(\nu)$ must be used.(Equation (59),(60), and (61))

Using spectroscopic data and the expressions derived above, quantitative values can be determined for the stimulated radiative transition rates appearing in the rate equations. Specifically, for the 1→4 and 4→1 transitions of Tm^{3+} in YAG as shown in Figure 4, there are a number of transitions occurring at nearly the same (or in fact identical) frequencies. The individual Stark component to Stark component transition cross sections cannot be determined and the terms appearing in the rate equations for R_{14} and R_{41} are given by Equations (59) and (60). The absorption cross section used in determining values for these rates is found by dividing the absorption coefficient by the total ground state population of Tm^{3+} ions. This cross section is a weighted sum of the individual Stark component transition cross sections (the σ_{lu}'s) and the weighting factors are the Boltzmann factors. The stimulated emission cross section can be found from Equation (60) using the measured absorption coefficient with Z_l and Z_u determined from the data in Refs. [62] and [63] and Equation (57).

Similarly, it is possible to determine values for the stimulated radiative transitions between levels 5 and 6 of Ho^{3+}. Since this is the laser transition the photon density at the laser frequency $n_p(\nu_L)$, rather than photon flux at the frequency of the transition $\Phi_L(\nu_L)$ is used. These two quantities are related through the expression

$$n_p = \Phi_L(\nu_L)/c \tag{62}$$

The parameters R_{56} and R_{65} are given by

$$R_{56} = n_p \omega_{el} B n_5 \tag{63}$$

and

$$R_{65} = n_p \omega_{el} n_6 \tag{64}$$

where B is a factor given by $B = \sigma_{56}/\sigma_{65}$. Since there are numerous Stark level to Stark level transitions in this spectral range Equation (61) must be used to determine the emission cross section from the measured absorption cross section.

Table I lists the cross sections determined from the procedures outlined above and other cavity parameters used in the rate equations for the computer simulations described later. Other known parameters needed for the rate equation model such as relaxation times and transition branching ratios for this system are listed in Table II. The major unknown parameters required for solving the rate equations (excluding the loss mechanisms) are the ion-ion interaction rates describing the Tm-Tm and Tm-Ho cross relaxation process. These parameters are determined from analysis of the visible and near infra-red spectral properties as described below.

Experiment

A nitrogen laser pumped dye laser was used to excite the samples either via the Ho^{3+} absorption line at 453.8 nm or the Tm^{3+} absorption lines at 459.1 and 780.0 nm. The pump beam had less than a 10 ns pulse duration and less than a 0.1 nm spectral bandwidth. This source was used for most of the spectral dynamics studies. An alexandrite laser tunable from 700-800 nm with a 60 μs pulse train consisting of numerous 300 ns long pulses was used for laser pumping and for some spectra measurements. Since this source directly excited the $^3H_4$ multiplet of Tm^{3+}, comparison of the resulting emission spectra to that obtained from the higher energy dye laser excitation was useful in determining whether additional emission lines in the regions of interest were produced by the higher energy excitation. A third excitation source, a Cr,Tm,Ho:YAG laser was used in conjunction with the alexandrite laser to study the origin of the green emission previously reported.

Three different samples were used in this study. The first sample, Tm(6.0%), Ho(0.5%):YAG, was cut from the same boule as the sample used for the investigation of laser properties in Ref.[45]. A second sample, Tm(10.0%):YAG, was used

TABLE I

PARAMETERS USED IN RATE EQUATION MODEL
FOR Tm,Ho:YAG LASER SIMULATIONS

Pump Cross Sections

$\sigma_{14} = 5.2 \times 10^{-21} cm^2$

$\sigma_{41} = 2.8 \times 10^{-21} cm^2$

Cavity Parameters

$\tau_c = 33ns$

$\omega_{el} = 9.06 \times 10^{-12} cm^3/s$

Laser Emission Cross Section

$\sigma_{65} = 1.4 \times 10^{-20} cm^2$

B=0.159

TABLE II

PARAMETERS USED IN Tm,Ho:YAG
RATE EQUATION MODEL

Radiative Decay Rates

$A_{41} = 578s^{-1}$ [a]
$A_{42} = 80s^{-1}$ [a]
$A_{43} = 31s^{-1}$ [a]
$A_{31} = 299s^{-1}$ [a]
$A_{32} = 5s^{-1}$ [a]
$A_{21} = 110s^{-1}$ [a]
$A_{65} = 150s^{-1}$ [b]

Non-Radiative Decay Rates

$W_{43} = 580s^{-1}$ [a]
$W_{32} = 7.7 \times 10^4 s^{-1}$ [a]
$W_{21} = 5.9s^{-1}$ [a]

Effective Decay Times

$\tau_8 = 4.7\mu s$ [c]
$\tau_7 = 16.1\mu s$ [d]

---

a Ref. [64].
b Ref. [52].
c Ref. [65].
d Calculated From data in Refs. [63,64].

to determine spectral properties of Tm^{3+} ions in YAG. Similarly the third sample, Ho(0.5%):YAG, was used to determine spectral properties of the Ho^{3+} ions and to investigate the origin of the green emission observed with alexandrite laser pumping.

Emission from the samples was focused into one of two spectrometers and monitored with various detectors depending on the emission wavelength. For obtaining much of the visible emission spectra, a Spex 0.85 m double spectrometer coupled to a Hammamatsu R943-02 photomultiplier tube was used. A Spex 0.22 m spectrometer with a 500 nm blazed grating and a Hammamatsu R446 photomultiplier were used for detecting some of the visible spectra. This spectrometer with a 2.0 μm blazed grating and an InSb detector were used for monitoring all of the near infra-red spectra.

For all spectral measurements, the signal from the detector was averaged using an EG&G series 4400 boxcar averager. The gate delay of the boxcar was varied to observe emission spectra at different times after the excitation pulse. The output was digitized and stored on the spectrometer control computer. For the fluorescence rise time and decay time measurements the signals were either averaged using the boxcar averager or were averaged using a Tektronix 2440 digital oscilloscope. In all cases the data were down-loaded for analysis on an IBM-compatible personal computer.

Results

The first problem is to correlate important spectral features with specific transitions of the Tm^{3+} and Ho^{3+} ions. Figures 6(a) and 6(b) show the emission spectra in the 725-850 nm region for Tm,Ho:YAG after Tm^{3+} (459.1 nm) and Ho^{3+} (453.8 nm) excitation, respectively. The presence of only weak Ho^{3+} emission in the 740-775 nm region under Tm^{3+} excitation indicates little energy transfer occurs between the upper states of the ions. The emission in the 780-850 nm region is due only to Tm^{3+}.

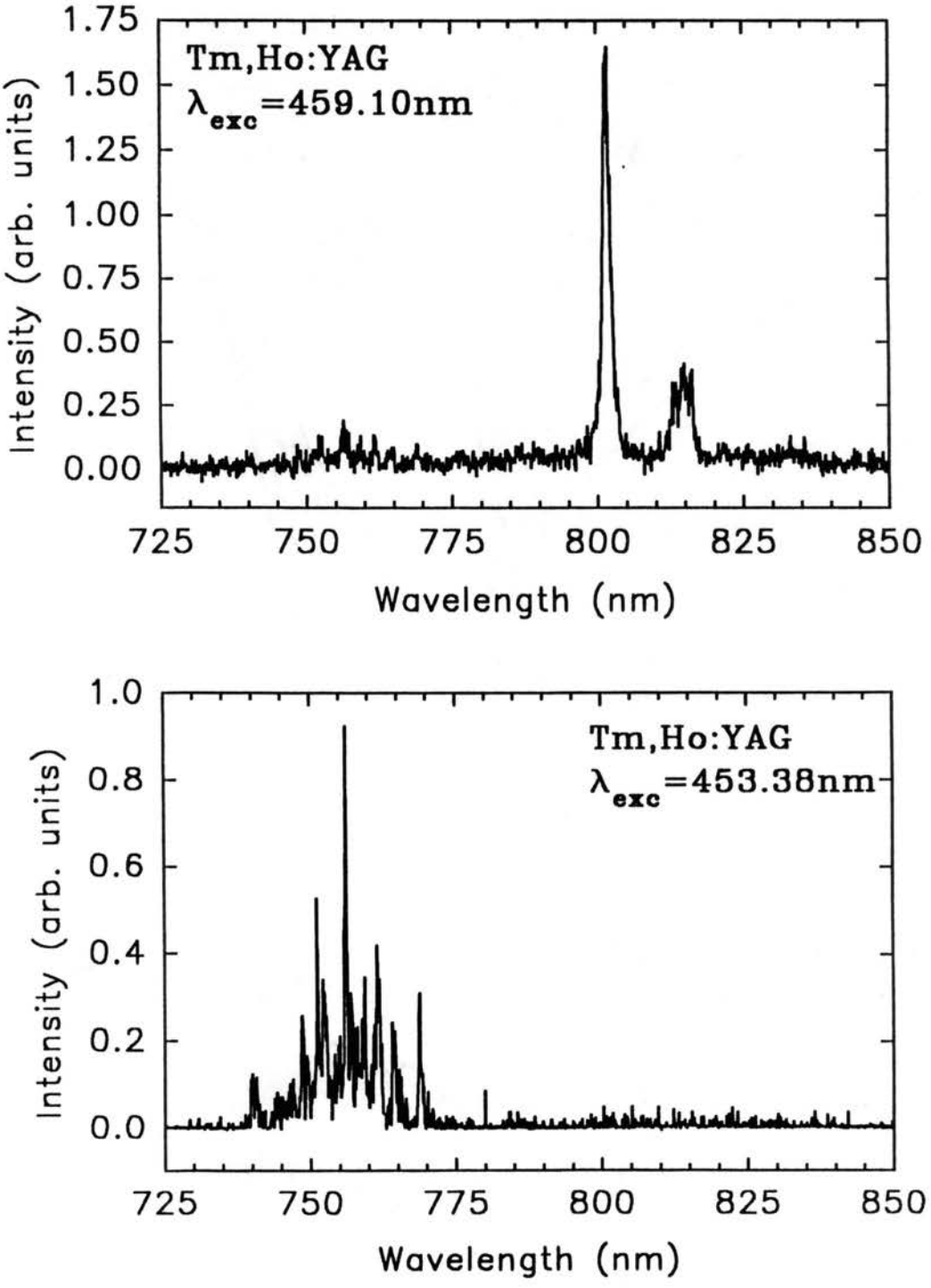

Figure 6. Emission Spectra of Tm,Ho:YAG 725-850 nm. Excitation at (a) 459.10 nm and (b) 453.38 nm.

The observed differences between the emission spectra under different excitation conditions are used to establish the Tm^{3+} transitions responsible for the emission in the 770-850 nm spectral range. Figures 7(a) and 7(b) show these spectra. Figure 7(a) shows Tm,Ho:YAG emission spectrum after 765 nm excitation using the alexandrite laser while Figure 7(b) shows the Tm:YAG spectrum under 459.1 nm excitation. Since there is no significant Ho^{3+} emission in this region (Figure 6(b)), the emission present in Figure 6(a) and not present in Figure 7(a) must be due to transitions in Tm^{3+} originating from levels higher in energy than $^3H_4$, such as the $^1G_4$ level which is the terminal state of the 459.1 nm absorption transition. Thus the strong lines observed at 801.7 nm and between 810-815 nm, visible under 459.1 nm excitation but not observed under 765 nm excitation, are not due to emission from the $^3H_4$ multiplet.

Although the concentration dependence of the $^3H_4$ fluorescence lifetime has been studied previously [55], discrepancies in literature values and differences in sample concentration require the direct measurement of this lifetime in our sample.[50,52,54] The results of fluorescence lifetime measurements in the 800 nm spectral region are consistent with the conclusions stated above. The measured fluorescence lifetimes in this region are as follows: at 801.7 nm a double exponential decay is observed with time constants of 1.6 and 11.5 μs. The lifetime at 822 nm, that of the $^3H_4$ multiplet of Tm^{3+}, is found to be 11.5 μs. The shorter 1.6 μs lifetime measured at 801.7 nm is attributed to a transition originating on the $^1G_4$ multiplet that happens to overlap the $^3H_4$ emission. The lifetime of the $^3H_4$ multiplet is a measure of the $^3H_4 \rightarrow {}^3F_4$, $^3H_6 \rightarrow {}^3F_4$ cross relaxation rate. Figure 8 shows the concentration dependence of the fluorescence quantum efficiency of the $^3H_4$ multiplet. The fluorescence quantum efficiency of emission from $^3H_4$ can be determined from

$$\eta = A_r / A_m \tag{65}$$

where A_r is the predicted radiative relaxation rate and A_m is the measured radiative rate. The predicted radiative lifetime is 790 μs [64] giving a predicted rate of 1270 s^{-1} . The data represent a combination of the results obtained here and those

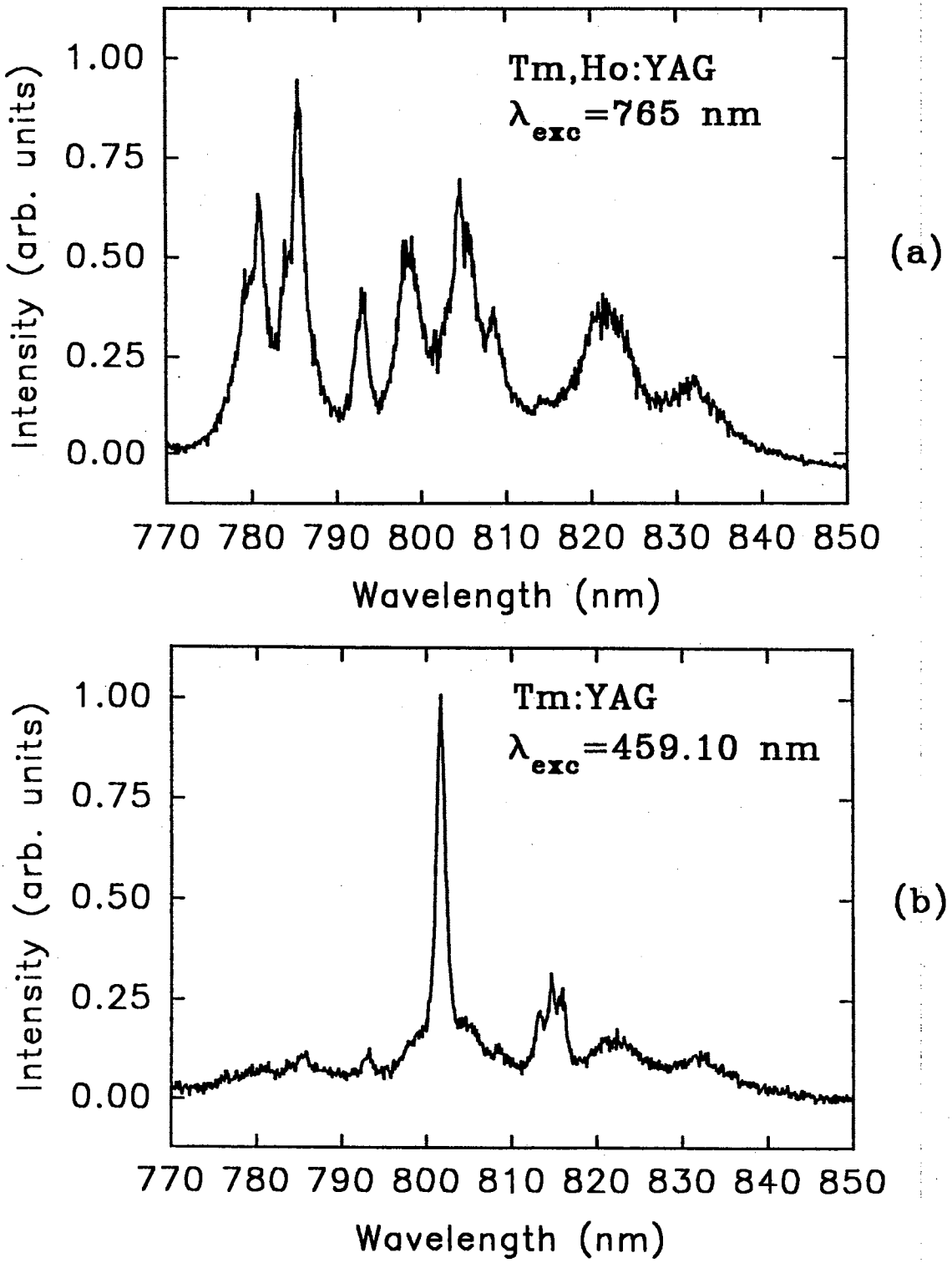

Figure 7. Emission Spectra of Tm,Ho:YAG and Tm:YAG 770-850 nm. (a) Tm,Ho:YAG with excitation at 765 nm and (b) Tm:YAG with excitation at 459.1 nm.

of several other research groups. [55,57] The solid and broken lines represent the theoretical predictions described in the following section.

The time evolution of the fluorescence emission in the 1.6-2.2 μm spectral region is needed to determine the interaction rate between the Tm^{3+} and Ho^{3+} ions in their metastable states. Figure 9 shows the emission from Tm,Ho:YAG in the 1.6-2.2 μm region under excitation at 765 nm. The numerous emission bands in this region correspond to emission from the Tm^{3+} $^3F_4$ and Ho^{3+} $^5I_7$ multiplets. Measurement of the fluorescence decays of the peaks at 1.78 μm and 2.09 μm give the values of the fluorescence lifetimes of the $^3F_4$ and $^5I_7$ levels to be 5$\pm$1 ms and 7$\pm$1 ms, respectively.

The different dynamic behavior of the various emission bands in this region is clearly shown by the results of the time resolved spectroscopic measurements. Figure 10 shows a series of spectra from a Tm,Ho:YAG sample in the 1.5-2.2 μm spectral region taken at various time delays after excitation at 459.1 nm. At short times after the excitation, the emission spectrum is broad and relatively featureless. At successively longer delays, the emission spectrum changes significantly and additional lines at 1.88, 1.93, 2.02 and 2.09 μm become significant. The broad band of peaks between 1.6-1.9 μm remains essentially unchanged or decays slowly. At very long times (5 and 10 ms) the emission in the whole spectral range shows signs of significant decay.

To identify the origin of each of the bands seen in this region, the emission spectrum of Tm:YAG is needed. Figures 11a and 11b show spectra taken at the same delay time, 300 μs, in Tm:YAG and Tm,Ho:YAG, respectively. The additional peaks at the longer delay times in Figure10 must be associated with Ho^{3+} transitions since they are not present in the Tm:YAG spectrum.

Analysis

Although the concentration dependence of the fluorescence lifetime of the $^3H_4$ multiplet of Tm^{3+} has been studied previously [55,57] further investigation of can help is necessary to determine if energy migration occurs in the $^3H_4$ multiplet.

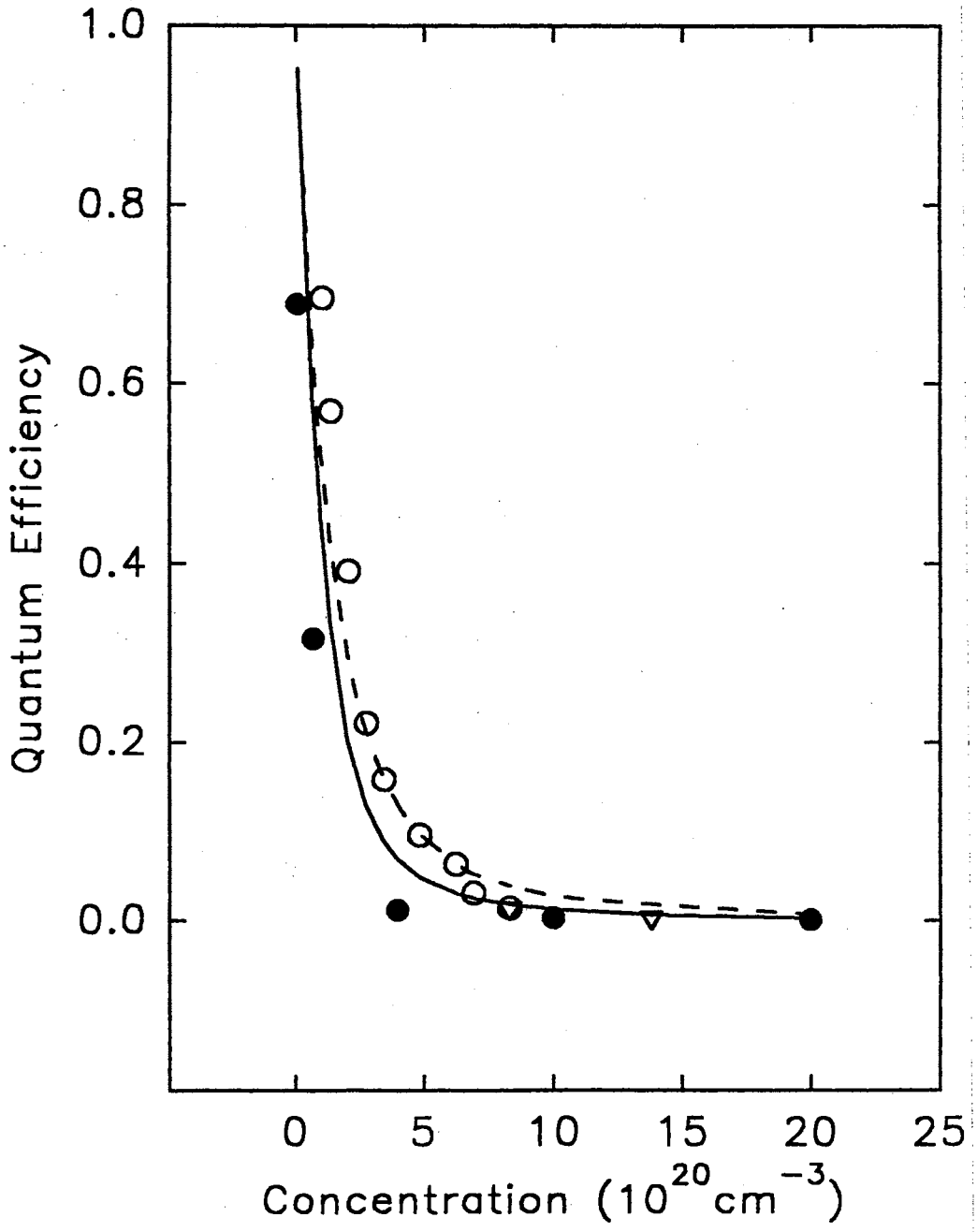

Figure 8. Quantum Efficiency of $^3H_4$ Emission vs Tm^{3+} Concentration.

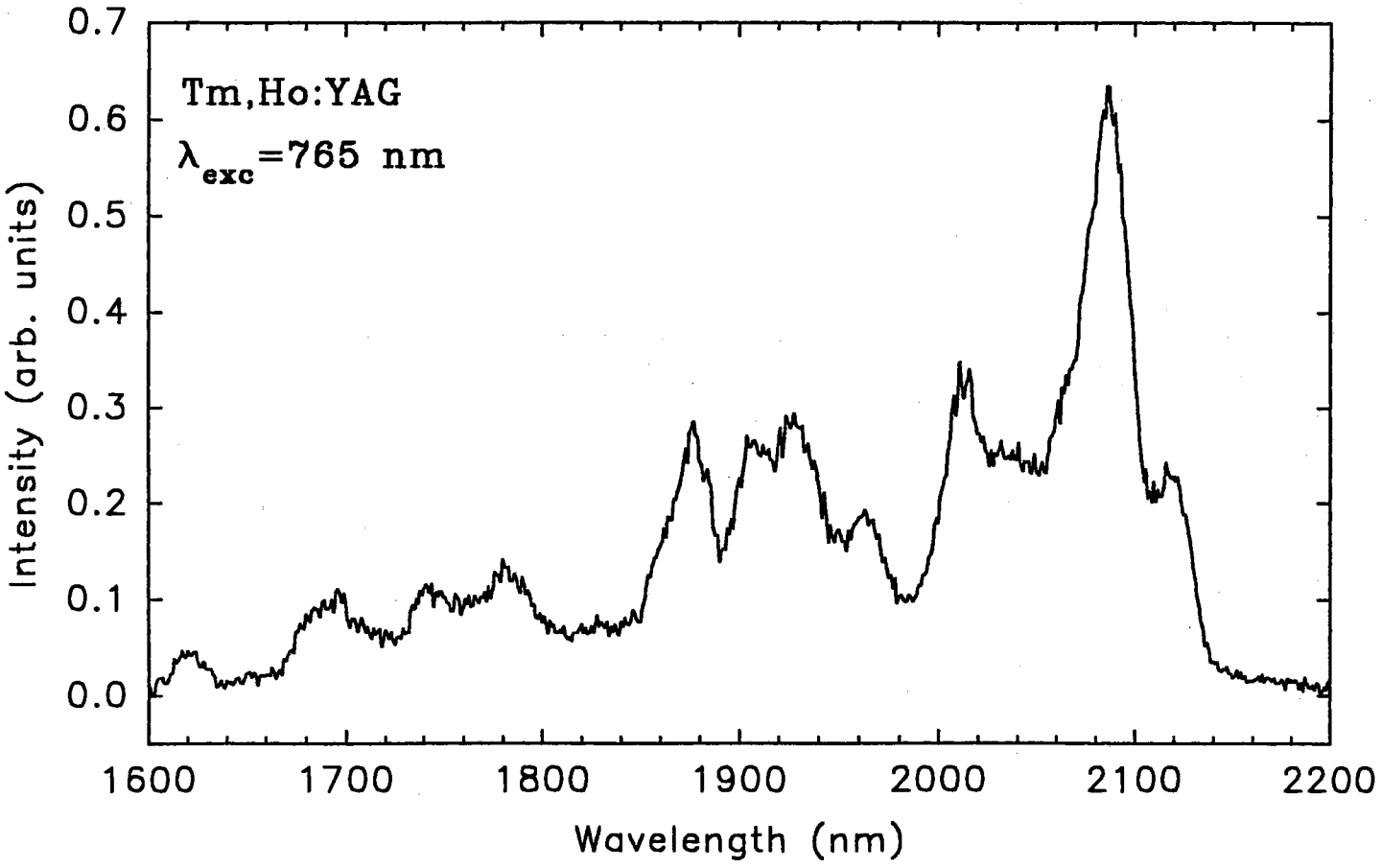

Figure 9. Emission spectrum of Tm,Ho:YAG 1600-2200 nm with excitation at 765 nm.

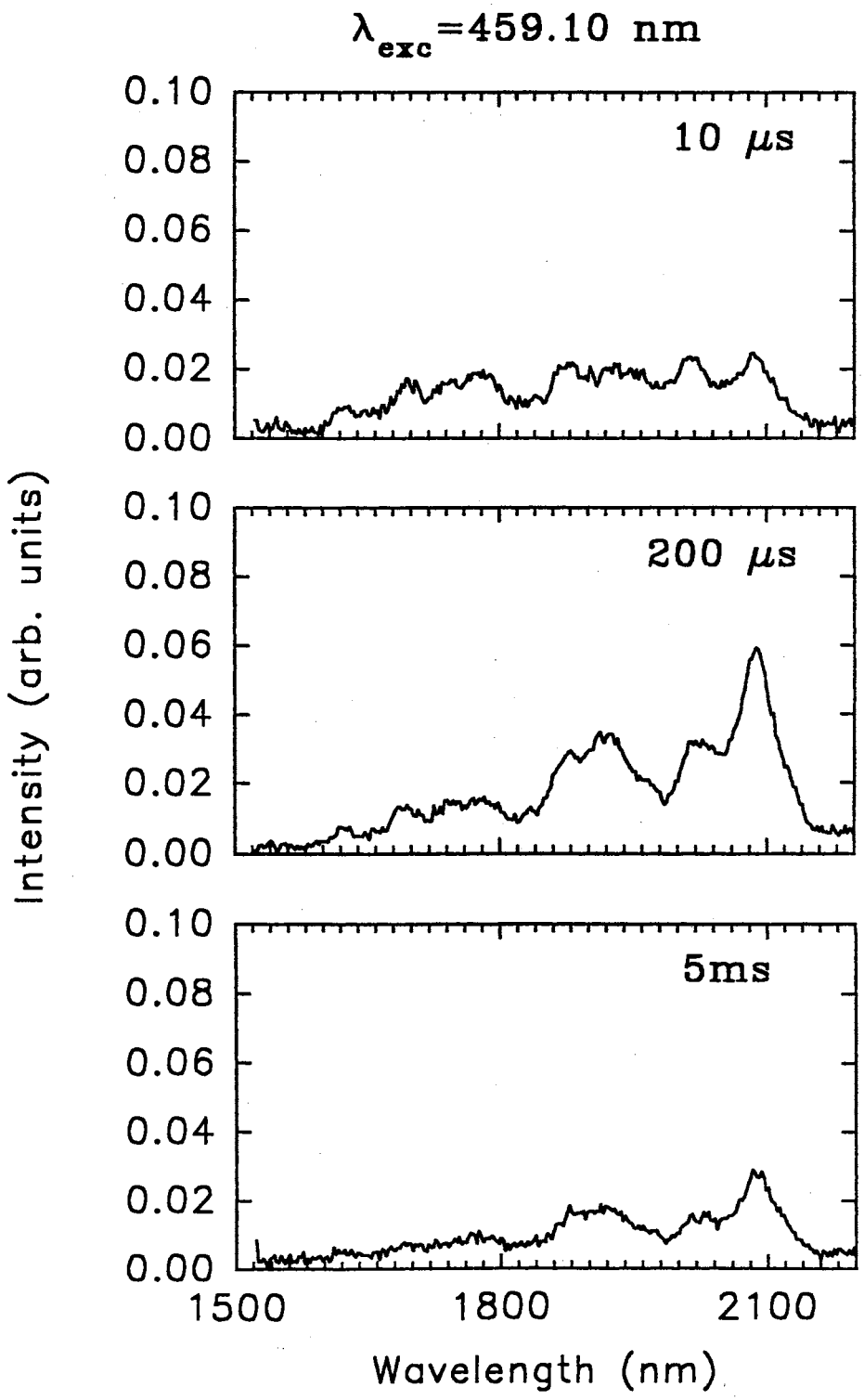

Figure 10. Series of Time-Resolved Spectra of Tm,Ho:YAG.

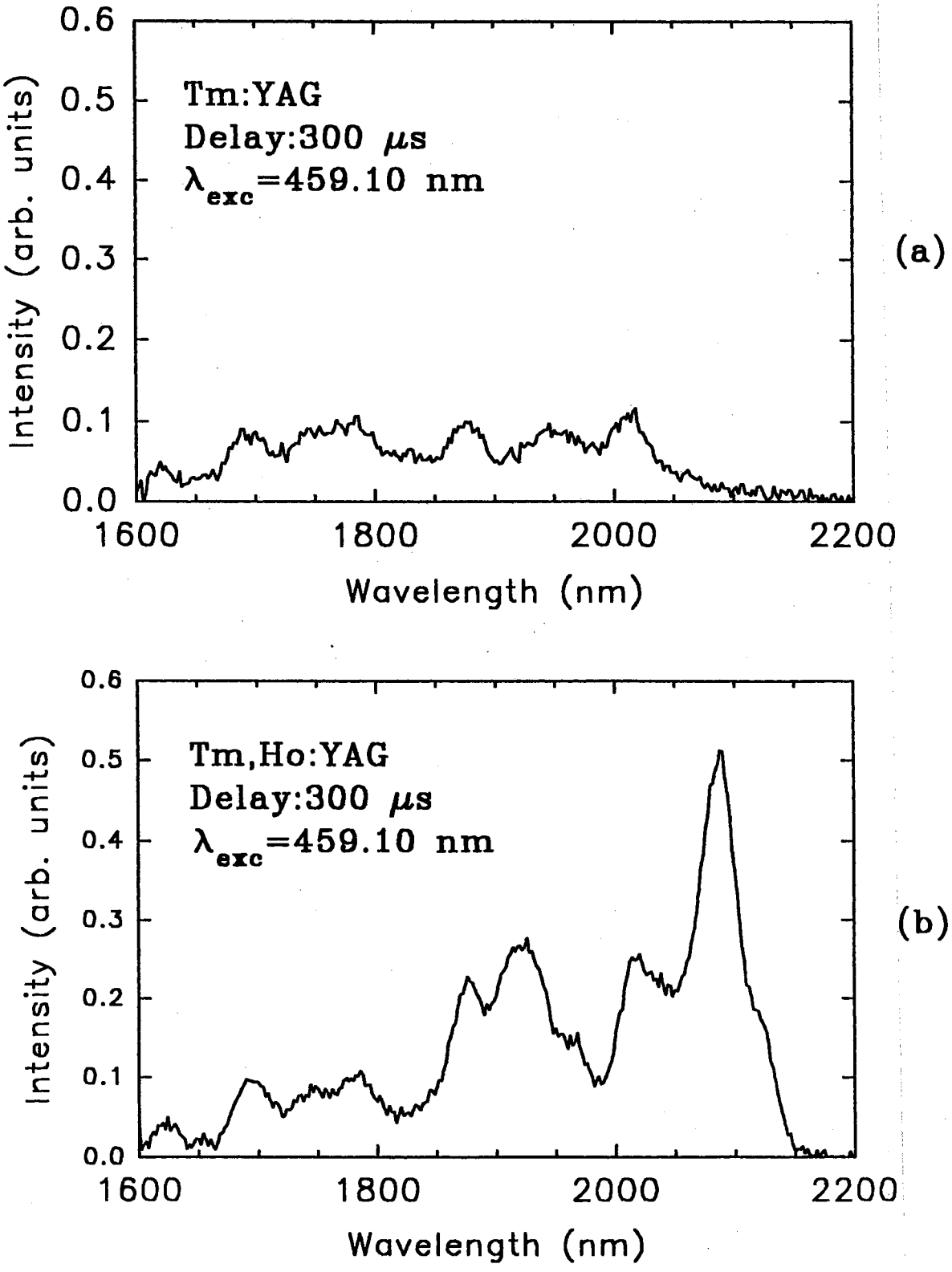

Figure 11. Emission Spectra of Tm:YAG and Tm,Ho:YAG 1600-2200 nm Taken 300 μs After Excitation. (a) Tm:YAG and (b) Tm,Ho:YAG.

The observed concentration quenching is generally attributed to a cross relaxation process in which a Tm^{3+} ion initially in the $^3H_4$ state interacts with a neighboring Tm^{3+} ion initially in the ground state leaving both ions in the $^3F_4$ metastable state. However, a possible additional process for concentration quenching is migration enhanced quenching with energy migration occurring within the $^3H_4$ level and eventual energy loss at a quenching site. The effect of each of these processes is considered here.

Two possible types of ion-ion interactions leading to the quenching of fluorescence from $^3H_4$ are cross relaxation and migration enhanced cross-relaxation mechanisms. The time evolution of the intensity of fluorescence emission from $^3H_4$ can be written as [66]

$$I(t) = I(0)exp[-(A_r t + \gamma t^{1/2} + Wt)] \tag{66}$$

where $I(0)$ is the initial intensity, γ is a parameter describing the ion-ion cross-relaxation without migration and W is a migration assisted enhancement to the cross-relaxation rate. The parameter γ is of the form described by the Forster-Dexter theory for static disordered decay [28,29]

$$\gamma = (4/3)(\pi)^{3/2} n_{Tm} R_{cr}^3 A_r^{1/2}. \tag{67}$$

Here R_{cr} is the critical interaction distance between two Tm^{3+} ions for cross-relaxation and n_{Tm} is the concentration of Tm^{3+} ions. The migration enhanced cross-relaxation rate is of the form determined by Burshtein [37]

$$W = \pi(2\pi/3)^{5/2} R_{cr}^3 R_{mig}^3 n_{Tm}^2 A_r \tag{68}$$

where R_{mig} is the critical interaction distance between Tm^{3+} ions for energy migration. Again it is assumed that electric dipole-dipole interaction is responsible for both the migration and the final cross relaxation quenching step. Equations (67) and (68) above reflect the fact that, for the case of interest here, both the sensitizers and activators are Tm ions.

Following the development in Ref. [66] Equation (66) can be used to obtain an expression for the fluorescence quantum efficiency

$$\eta = [A_r/(A_r + W)][1 - \pi^{1/2} x \exp(x^2)(1 - erf(x)) \quad (69)$$

where

$$x = \gamma/[2(A_r + W)^{1/2}] \quad (70)$$

The only unknown quantities in Equations (67,69) are the critical interaction distances. These critical interaction distances can be determined from spectral overlap data and Equation (32). Figure 12 shows the normalized emission and absorption lineshapes of the $^3H_6 \rightarrow ^3H_4$ and $^3H_4 \rightarrow ^3H_6$ transitions. These are the spectra needed to determine a migration rate for the $^3H_4$ migration process. Using the spectra in Figure 12 and Equation (32), R_{mig} is found to be 10.3 Å. The critical interaction distance for cross-relaxation can be found from Ref. [57], adjusted to correspond to our Equation (32), giving $R_{cr} = 6$ Å. Using these values in Equation (69) gives the predicted values for the fluorescence quantum efficiency shown as the solid line in Figure 8. The broken line in Figure 8 is obtained from Equation (69) with W =0 and represents the theoretical prediction for η if the static cross-relaxation process is considered to be the only process responsible for the quenching of the $^3H_4$ level. Both the theoretical curves are obtained with no adjustable parameters.

The differences in the experimental points from different research groups and from the prediction are partly associated with how accurately the Tm^{3+} concentrations in the samples are known. It is not clear from references [55] and [57] how these concentrations are measured. If the results from all the research groups are treated equally the solid line in Figure 8 best agrees with the data. If the quoted concentrations are those in the initial melt used for crystal growth instead of the values measured in the actual sample, they provide a high estimate of the concentration of Tm in the crystal. If this is the case then the solid line will be in much better agreement than the broken line. In either case it appears that some energy migration is taking place in the $^3H_4$ level of Tm^{3+} and this migration enhances the

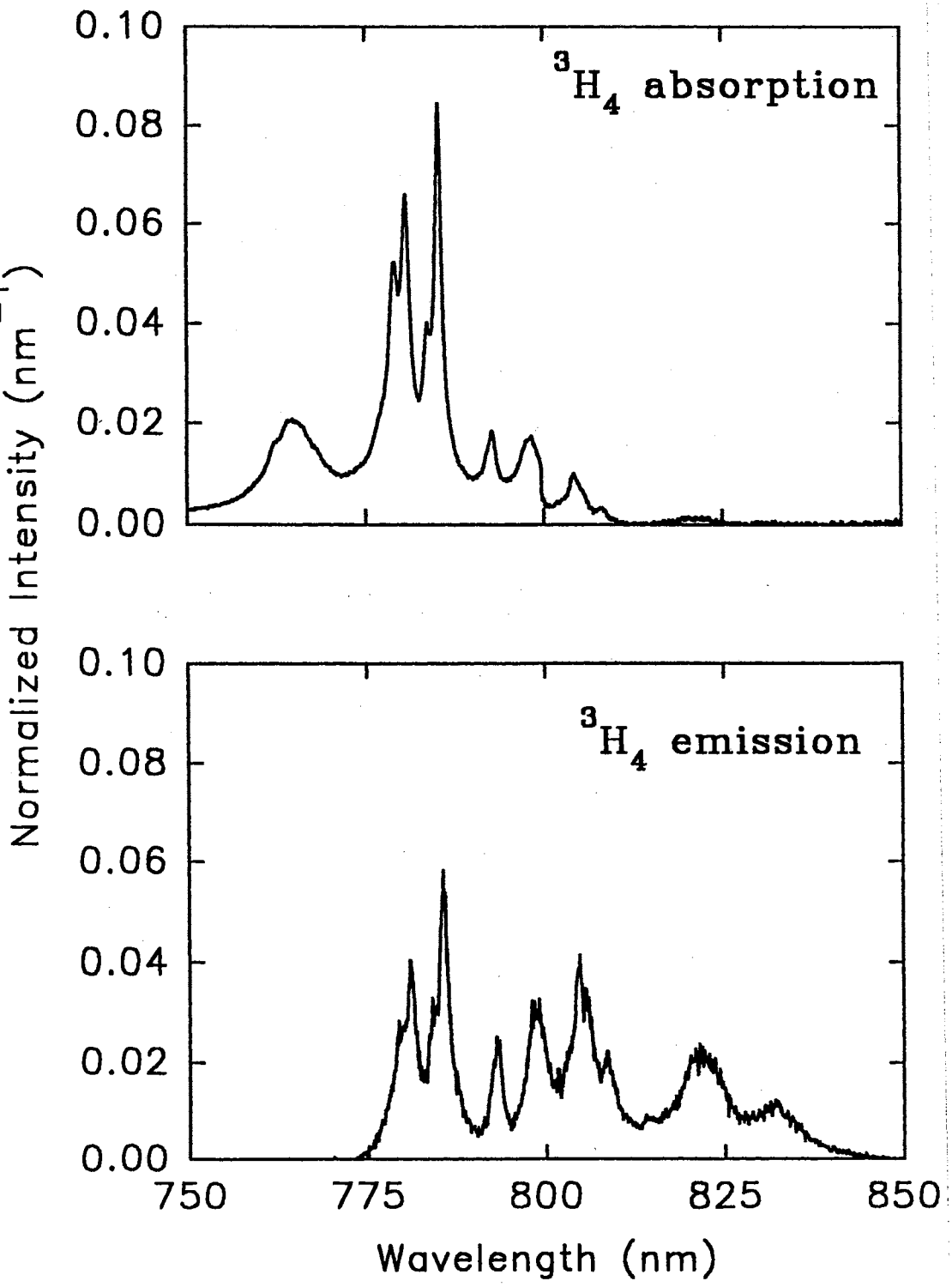

Figure 12. Normalized Absorption and Emission Spectra $^3H_4$,$^3H_6$ Transition.

cross-relaxation quenching of the luminescence from this level, especially at high Tm ion concentrations.

The decay dynamics of the fluorescence emission at 822 nm can be used to determine the effective cross relaxation rate parameter for the $^3H_4 \rightarrow {}^3F_4$, $^3H_6 \rightarrow {}^3F_4$ process in the Tm^{3+} ions, k_{42}. At long times after the excitation, the rate equation for the $^3H_4$ multiplet becomes (ignoring the loss mechanisms)

$$\dot{n}_4 = -k_{42} n_4 n_1 - n_4 \tau_4^{-1} - n_4 W_{43}. \tag{71}$$

Solving for $n_4(t)$ yields

$$n_4(t) = \exp(-t/\tau_m) \tag{72}$$

where τ_m is the measured lifetime. In the limit of low excitation intensity then most of the Tm^{3+} population remains in the ground state, i.e. $n_1 \approx N_{Tm}$ and

$$\tau_m^{-1} = k_{42} N_{Tm} + \tau_4^{-1} + W_{43}. \tag{73}$$

The $^3H_4$ multiplet has a predicted lifetime (including radiative and multiphonon decay),[62] of 790 μs. Using this value, our measured lifetime of 11.5 μs and N_{Tm} = 8.3×10^{20} cm^{-3} yields a value for the rate constant k_{42} of 1.0×10^{-16} cm^3/s.

Information about a second energy transfer process, the Tm^{3+} to Ho^{3+} process is obtained from the dynamics of the fluorescence emission in the near infrared spectral region. A relationship between the rate constants describing the forward and reverse energy transfer processes between the $^3F_4(Tm^{3+})$ and $^5I_7(Ho^{3+})$ multiplets can be found. At some time t_{max}, the excited state population $n_6(t)$ reaches a maximum and begins to decay. At this time (ignoring stimulated emission and the loss mechanisms)

$$\dot{n}_6 = -k_{62} n_6 n_1 + k_{26} n_5 n_2 - n_6 \tau_6^{-1} = 0. \tag{74}$$

Solving for k_{26} and using

$$n_1 = N_{Tm} - n_2 - n_4 \tag{75}$$

$$n_5 = N_{Ho} - n_6 \tag{76}$$

yields

$$k_{26} = \frac{n_6}{n_2}\frac{1}{N_{Ho}}\frac{\tau_6^{-1}}{\left(1-\frac{n_6}{N_{Ho}}\right)}\left[1 + k_{62}N_{Tm}\tau_6\left(1 - \frac{n_2+n_4}{N_{Tm}}\right)\right]. \tag{77}$$

At low levels of excitation, $n_6/N_{Ho} = 0$ and $(n_2 + n_4)/N_{Tm} = 0$ so

$$k_{26} = \frac{n_6}{n_2}\frac{\tau_6^{-1}}{N_{Ho}}\left(1 + k_{62}N_{Tm}\tau_6\right). \tag{78}$$

By determining the ratio of the population of n_6 to n_2 at t_{max}, it is possible to relate the two unknown rate constants. Figure 13 shows the 2.09 μm emission peaks $\approx$300 μs after the excitation pulse. Using the spectra taken at 300 μs (Figure11), correcting for detector and grating response, integrating to find the total emission intensity and multiplying by the upper state lifetimes, the relative populations of the two multiplets can be determined. Substituting this value into Equation (78) gives the relationship between the rate constants for forward and backward energy transfer,

$$k_{62} = 0.128k_{26} - 1.4 \times 10^{-19} cm^3/s. \tag{79}$$

To establish values for the rate constants k_{26} and k_{62} the following rate equations are solved with k_{26} treated as an adjustable parameter and the results fit to the observed spectroscopic data.

$$\begin{aligned}\dot{n}_1 = -R_{14} + R_{41} - k_{42}n_4n_1 - k_{62}n_6n_1 + k_{26}n_5n_2 \\ +n_2\tau_2^{-1} + A_{41}n_4 - A_{31}n_3\end{aligned} \tag{80}$$

$$\begin{aligned}\dot{n}_2 = 2k_{42}n_4n_1 + k_{62}n_6n_1 - k_{26}n_5n_2 \\ -n_2\tau_2^{-1} + A_{42}n_4 + A_{32}n_3 + W_{32}n_3\end{aligned} \tag{81}$$

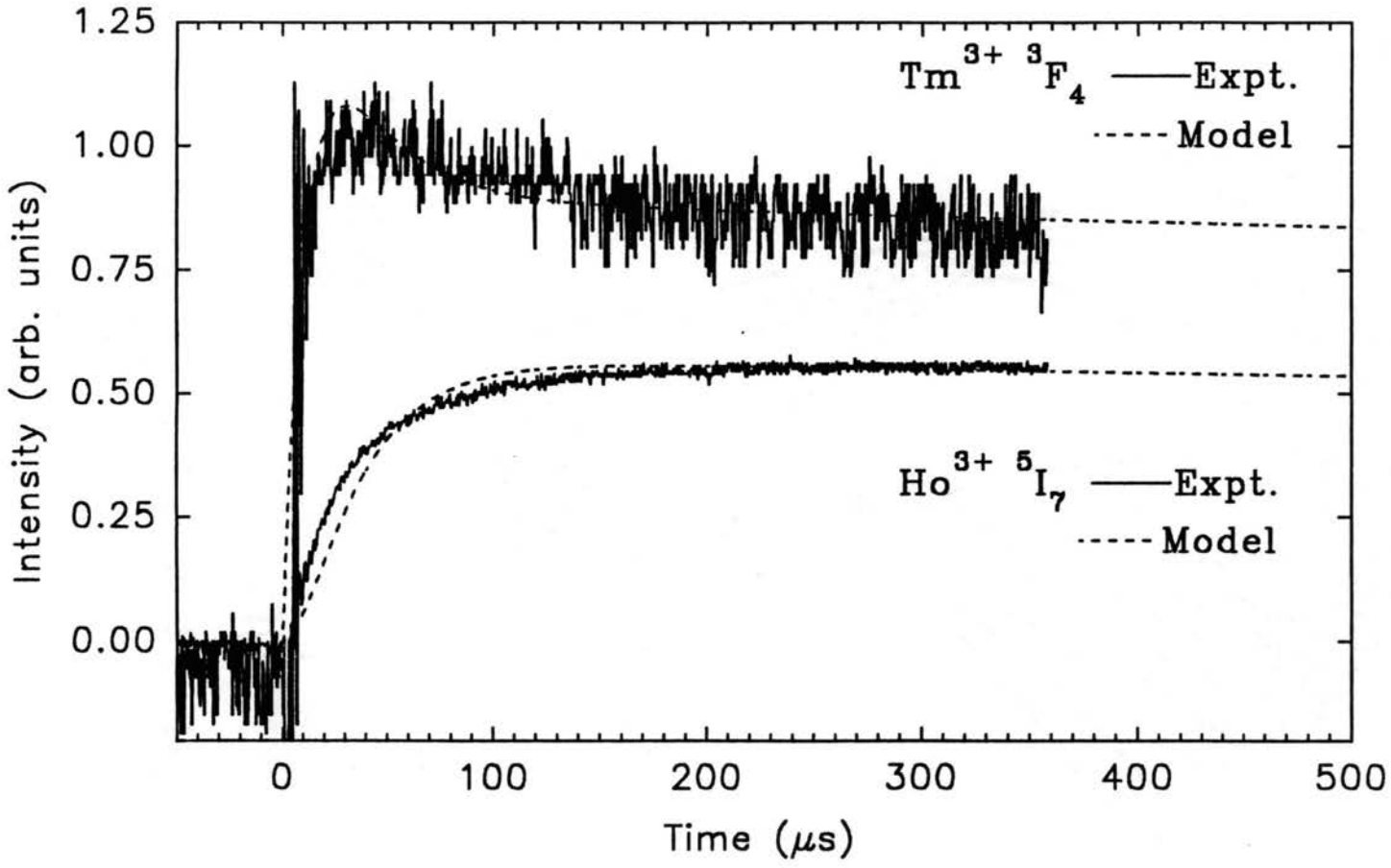

Figure 13. Growth and Decay of Emission in Near Infrared Spectral Region. The Signals are due to Transitions from the Tm^{3+} $^3F_4$ (n_2) and Ho^{3+} $^5I_7$(n_5) Multiplets. The Solid and Dashed Lines are Numerical Fits Using the Rate Equations Given in the Text.

$$\dot{n}_3 = -n_3\tau_3^{-1} + A_{43}n_4 + W_{43}n_4 - W_{32}n_3 \tag{82}$$

$$\dot{n}_4 = +R_{14} - R_{41} - k_{42}n_4n_1 - n_4\tau_4^{-1} - W_{43}n_4 \tag{83}$$

$$\dot{n}_5 = +k_{62}n_6n_1 - k_{26}n_5n_2 + n_6\tau_6^{-1} \tag{84}$$

$$\dot{n}_6 = -k_{62}n_6n_1 + k_{26}n_5n_2 - n_6\tau_6^{-1} \tag{85}$$

The solutions to the rate equations are obtained numerically using a fourth order adaptive step-size Runge-Kutta routine. The values of the parameters used in the equations are listed in Tables II and III. Since no cavity was used in the spectroscopic measurements, $n_p = 0$ for all times. All loss mechanisms are ignored and optically stimulated transitions between $^5I_7$ and $^5I_8$ are ignored. The results of these calculations are compared with the observed rise times of emission from the Tm^{3+} $^3H_4$ and Ho^{3+} $^5I_7$ multiplets. Figure 13 shows the time evolution of the Tm^{3+} metastable state population calculated numerically overlaid on the oscilloscope trace for the 1.77 μm emission. Figure 13 also shows the time evolution of the Ho^{3+} metastable state population determined numerically overlaid on the trace for the 2.09 μm emission. The experimental results are those obtained for excitation at 780.0 nm. The pump flux is 1.53×10^{24} photons/(cm^2 s) corresponding to a pulse energy of 1 μJ with a 10 ns duration and a 290 μm beam radius. The numerical predictions closely approximate the experimental results when $k_{26} = 2.0\times10^{-16}$ cm^3/s.

Modeling of Laser Operation

Now that the rate constants for this system are known, the rate equation model can be used to qualitatively simulate laser operation. Table I lists the additional parameters used in the laser simulation. The relaxation rates, branching

TABLE III

PARAMETERS USED IN RATE EQUATION MODEL FOR DETERMINING k_{26} AND k_{62}

Pump Cross Sections
$\sigma_{14} = 5.8 \times 10^{-21} cm^2$
$\sigma_{41} = 1.36 \times 10^{-22} cm^2$
Energy Transfer Parameters
$k_{42} = 1.0 \times 10^{-16} cm^3 s_{-1}$
$k_{26} = 2.0 \times 10^{-16} cm^3 s_{-1}$
$k_{62} = 2.6 \times 10^{-17} cm^3 s_{-1}$

ratios and energy transfer parameters are the same as those in Tables II and III. The cavity lifetime is determined by considering only output coupler losses. The emission cross sections are calculated from the absorption cross sections using Equation (61). The alexandrite laser pump pulse at 785 nm is modeled using a 60 μs pulse train consisting of a series of 300 ns pulses 1 μs apart.

The rate equations describe a macroscopic model dealing only with the populations of the relevant states and the overall system dynamics. A uniform distribution of excitation within the excited volume of the sample is assumed with this model. The model does not analyze the mode structure of the laser or treat the detailed spatial distribution of excitation in the active medium. In addition, only the emission at $\approx$2.097 μm is modeled. The additional laser emission bands observed at higher pump energies are not considered. Despite these simplifications, the model is a suitable description of the physical processes involved in this laser system and is useful in elucidating how these processes affect some of the properties of laser operation.

Figure 14 shows the numerical predictions for the temporal characteristics of the laser output for different pump energies and Figure 15 shows the experimental results for the observed laser emission reported previously in Ref. [45]. The details of the laser experiments are given in Ref. [45]. The similarities are striking. The time delay between the pump pulse and the laser output at $\approx$2.097 μm is modeled quite accurately. The delay between the pump pulse and the laser emission is observed to decrease with increased pump intensity. Additionally, the relaxation oscillations present in the experimental results are also predicted by the numerical model and the overall pulse shape is similar to that observed.

There are, however, some differences between the modeling and the experimental results. The threshold energy predicted by the numerical simulation is significantly lower than that found experimentally and the decay of the laser output in the simulation is somewhat longer than that observed experimentally. These effects may be attributed to additional loss mechanisms not included in the simplified model, such as the mechanism leading to the green fluorescence from the

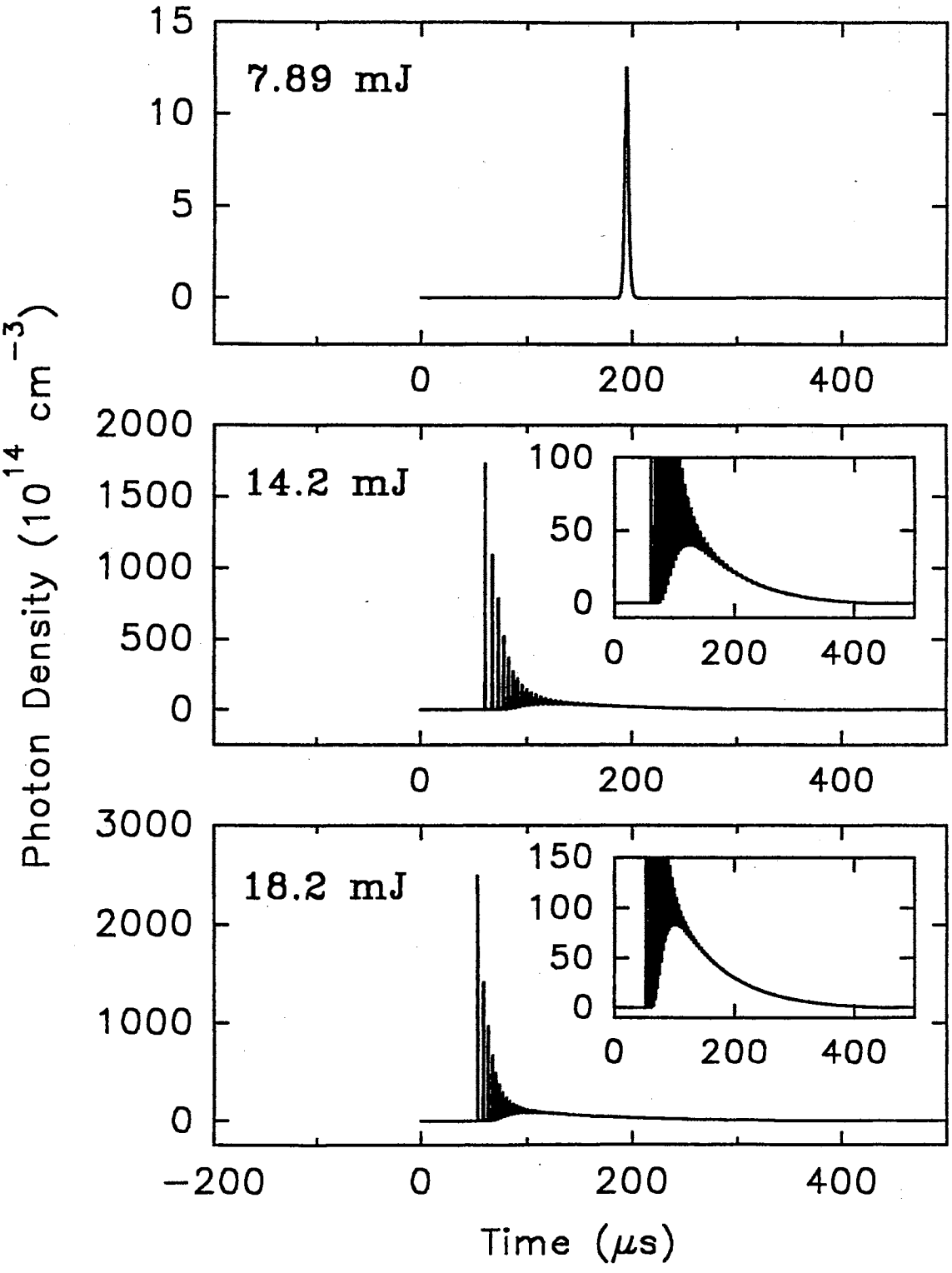

Figure 14. Numerical Modeling Results for a Tm,Ho:YAG Alexandrite Laser Pumped Laser. The insets show the details of the emission.

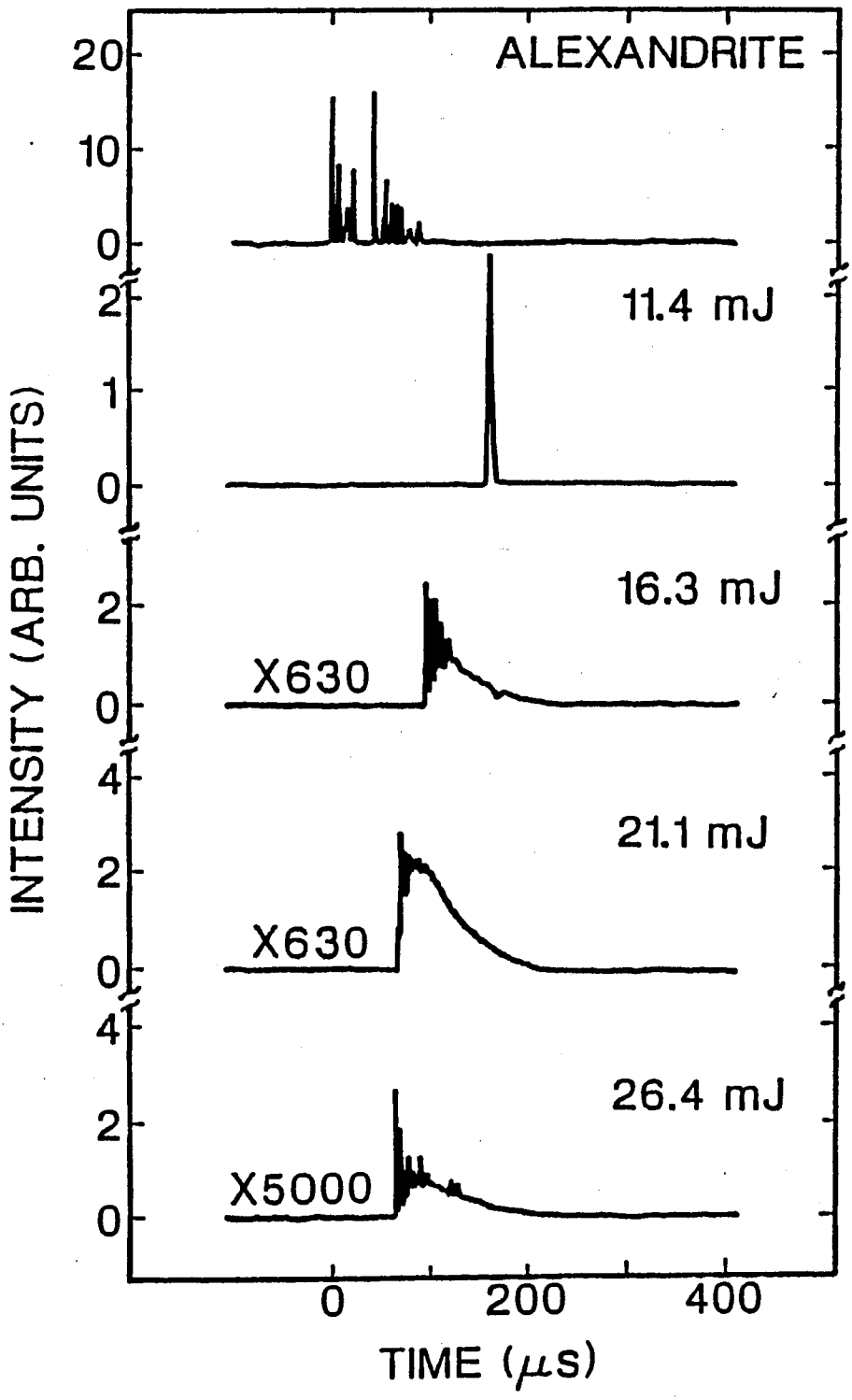

Figure 15. Experimental Results for a Tm,Ho:YAG Alexandrite Laser Pumped Laser. Taken from Ref. [45].

Ho^{3+} $^5S_2$ and $^5F_2$ multiplets to the ground state and the Tm^{3+} $^3F_4$ $\rightarrow$$^3H_6$ Ho^{3+} $^5I_7$ $\rightarrow$$^5I_5$ cross relaxation process often considered in CW systems.[52,54,67] Some of these loss mechanisms are discussed further in the following section. Additionally, thermal effects and cavity losses due to scattering and absorption processes not included in the model may affect the results.

Loss Mechanisms

The effects of three processes not considered above that can produce losses in laser operation of Tm,Ho:YAG are investigated here. The first mechanism considered is the energy transfer process involving the interaction of Tm^{3+} and Ho^{3+} ions that are both in their metastable states. This cross relaxation upconversion process populates the $^5I_5$ multiplet of Ho^{3+}. However, since no emission has been reported from the $^5I_5$ or $^5I_6$ [52] multiplets of Ho^{3+} in YAG, any ion excited to the $^5I_5$ multiplet must rapidly relax to the $^5I_6$ multiplet and then transfer its energy to the $^3H_5$ level of Tm^{3+}. Emission from $^5I_6$ must be very efficiently quenched by this energy transfer to Tm^{3+} since if the process was slow, then emission from $^5I_6$ would be detected. The mechanism is treated in the model as an infinitely fast energy transfer process to simulate this very efficient quenching.

The value of the rate parameter describing the interaction of Tm^{3+} and Ho^{3+} ions in their metastable states has been found either by measuring the temperature dependence of the gain of the $^5I_7$ $\rightarrow$$^5I_8$ transition [51,68] or by measuring the pump power dependence of the emission intensity from the $^5I_7$ [49,67,69] level. Values for k_{26} in the range 2.4-14$\times 10^{-17}$cm^3/s have been found. Note that nearly all of these measurements have been in flashlamp pumped systems and that the analysis used ignored other loss mechanisms mentioned earlier.

When the loss mechanism involving the metastable state interaction is included in laser simulation model described above, the predicted laser threshold increases by $\approx$5-25%. The temporal dynamics of the simulated laser emission do not change significantly.

The loss mechanisms leading to green emission seen during laser operation are not yet included in the model. There are at least two competing processes that can produce this emission: a cross relaxation process involving a $^3H_4 \rightarrow ^3H_6$ transition of a Tm^{3+} coupled with a $^5I_7 \rightarrow ^5F_2, ^5S_2$ transition of a Ho^{3+} ion [50], and the absorption of a pump photon by a Ho^{3+} ion in the metastable state (see Figure 4). The second of these processes is investigated here to determine what excitation conditions will lead to excited state absorption of pump photons.

The excitation spectrum found by observing the 538 nm emission at various alexandrite laser wavelengths is shown in Figure 16. Although the resolution is limited to 2 nm, the essential feature is clearly present. Little or no green emission is observed for alexandrite laser wavelengths greater than 770 nm. To supplement the results of this excitation spectrum, fluorescence emission spectra in the green region obtained for simultaneous excitation at 2.1 μm and each of the three alexandrite laser pump wavelengths used in Ref. [45] (765 nm, 780 nm and 785 nm) are shown in Figure 17. The pump pulse energy is the same for each spectrum. Significant green emission is present only with a 765 nm pump wavelength. If either of the excitation beams is blocked during these measurements, the green emission vanishes completely. Thus for these excitation conditions, the green emission is not due to a complex Ho^{3+} ion-ion upconversion process. Instead the green emission is due to the absorption of an alexandrite laser pump photon by a Ho^{3+} ion previously excited to the metastable state.

This experiment establishes the excited state absorption (ESA) of pump photons by Ho^{3+} ions in the metastable state as one process leading to the green emission often reported for Tm,Ho co-doped materials. However, the lack of green emission for the 780 and 785 nm pump wavelengths in the Ho:YAG sample investigated in this experiment, combined with the observation of green emission in Tm,Ho:YAG at identical pump wavelengths [45], indicates that an additional process involving Tm-Ho ion-ion cross relaxation occurs in Tm,Ho:YAG.

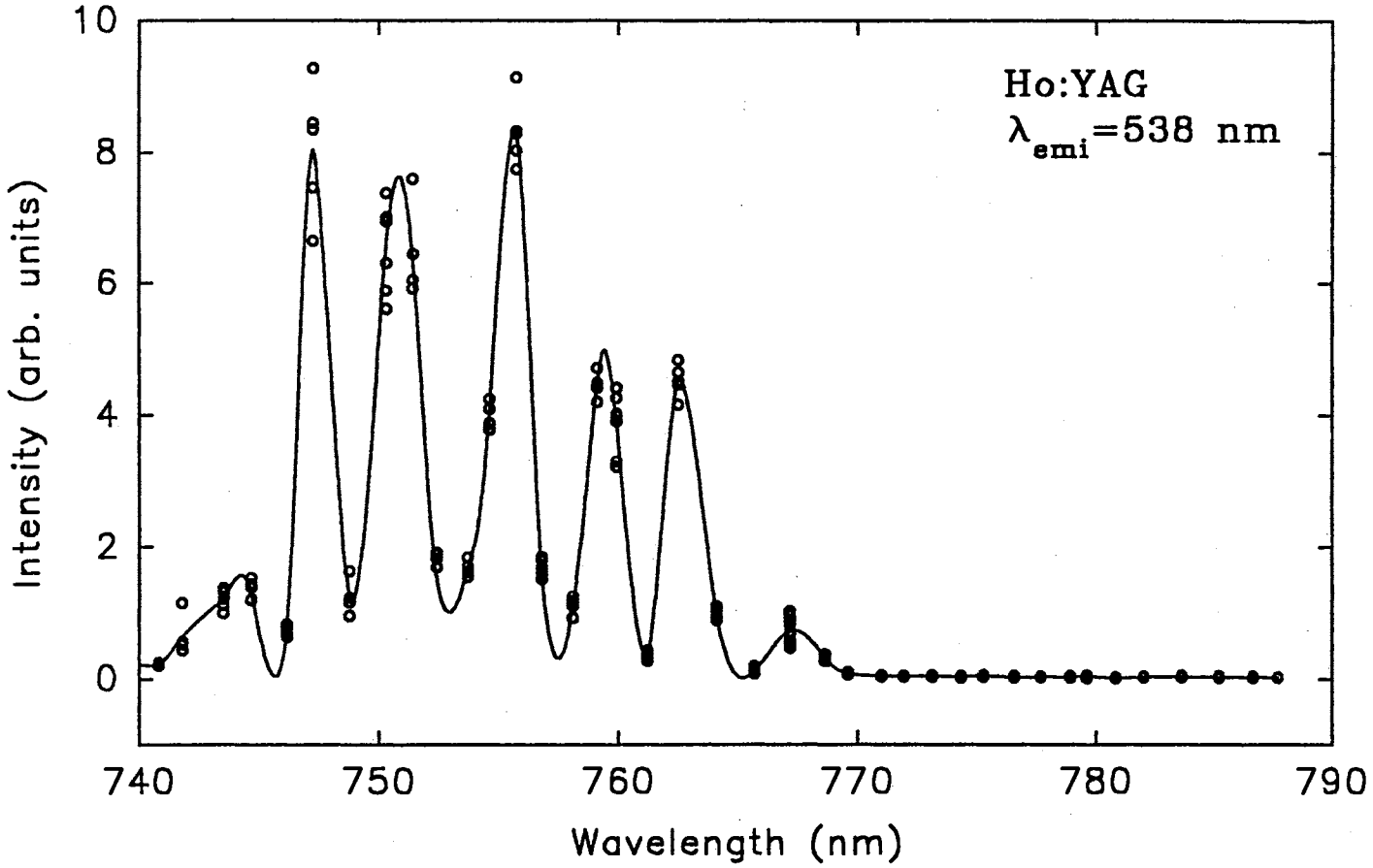

Figure 16. Excitation Spectrum of Ho:YAG. Primary Excitation is at 2.1 μm with a Secondary Excitation Tunable from 700-800 nm. The Open Circles are the Data and the Solid Line is a Spline Fit Drawn Through the Average Value at Each Wavelength

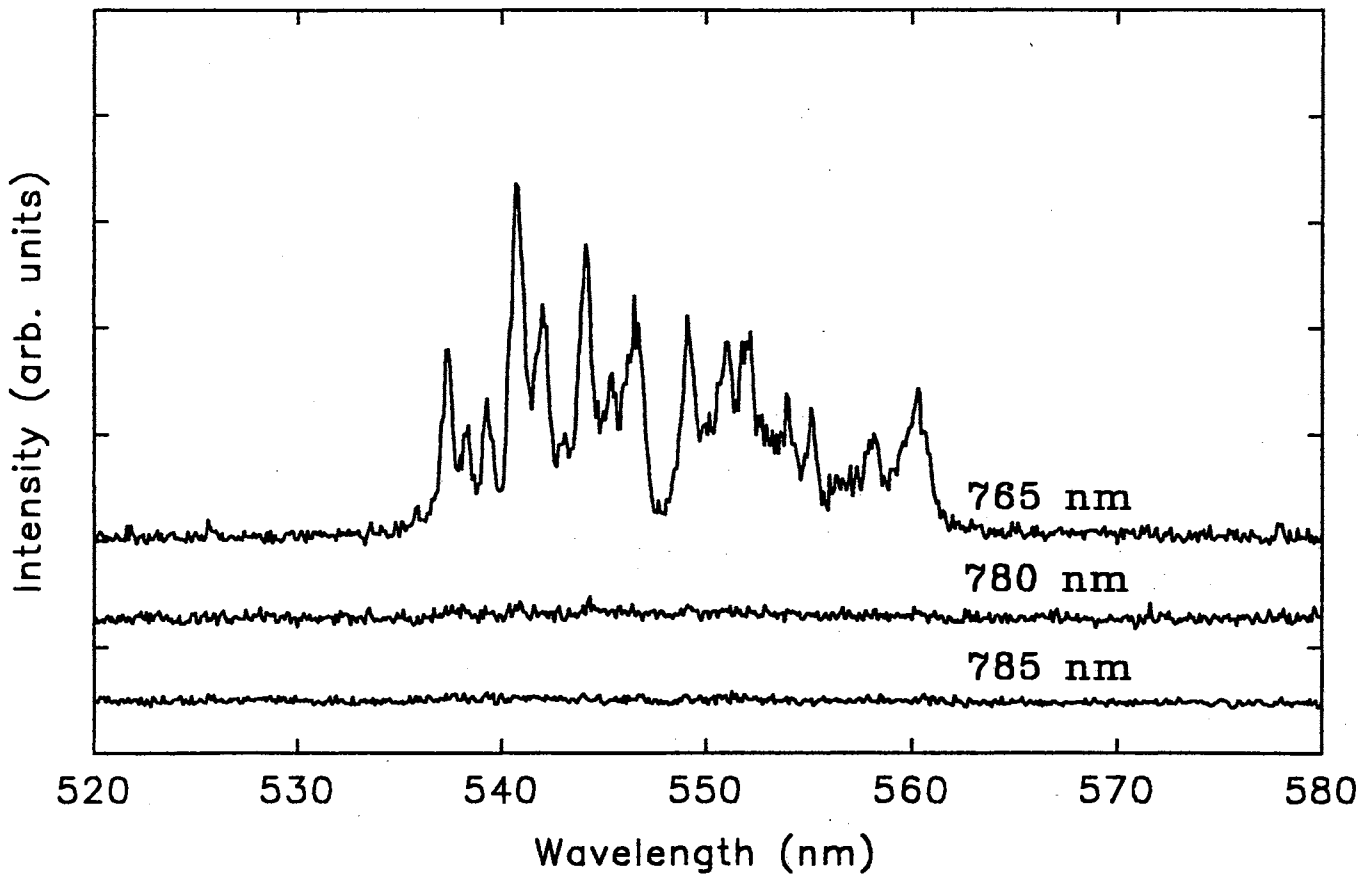

Figure 17. Emission Spectra of Ho:YAG 520-580 nm. Spectra taken at three Different Alexandrite Pump Wavelengths are Shown. The Excitation Pulse Energy is the Same for Each Wavelength.

The effects of both of these mechanisms on the solutions to the rate equations discussed in the previous section need to be considered. Since the rate parameters governing these mechanisms are unknown, order of magnitude estimates are used. Typical values of $\sigma_{68}=1\times10^{-20}\text{cm}^2$and $k_{48}=3\times10^{-17}\text{cm}^3/\text{s}$ are considered. No significant change in the laser threshold predicted by the computer simulation is caused by either the ESA or the ion-ion upconversion mechanisms. In addition, the overall laser output dynamics predicted by the model are not significantly changed. The maximum population of level 8 (Figure 4), the origin of the green emission, is predicted by the computer simulation to be only $\approx$0.1 and 1% of the metastable state populations for the excitation mechanisms of ion-ion interaction and pump photon ESA, respectively. Thus it appears that both of these mechanisms contribute to the observed green fluorescence of the Tm,Ho:YAG laser under the pumping conditions used in [45], but neither significantly effects the overall behavior of the system.

None of the mechanisms described above significantly changed the dynamics of the system predicted by the computer simulation. Specifically, these mechanisms do not explain the large difference in the magnitude of the relaxation oscillations predicted by the numerical model and those observed experimentally. One of the possible causes of this discrepancy may be the spatial distribution of the excitation energy. One of the assumptions in the rate equation model is that of uniform pumping.

Experimentally, nearly 63% of the incident energy was absorbed by the sample, so the pump beam intensity was reduced significantly as it passed through the sample. [45] Thus the sample was not uniformly excited and regions not pumped above threshold act as a loss for the laser emission. These losses have not been accounted for in the model.

Another possible effect of non-uniform pumping is that the upconversion processes may be underestimated. Since these processes involve interactions between two ions in excited states, or an ion an excited state and a pump photon, their effects scale as $(\Phi_p)^2$. Thus regions more strongly excited than the average

value used in the rate equations will have much larger upconversion losses. These effects could be the cause of the differences in the magnitudes of the relaxation oscillations.

Summary and Conclusions

The results of this work are three-fold. First, the values for the energy transfer rate constants in the Tm,Ho:YAG are established from a spectroscopic study of the spectral dynamics of the system. The value of the rate parameter k_{26} determined here, combined with previous experimental work [59,60], gives a more complete understanding of the overall energy migration and energy transfer processes in Tm,Ho-doped materials. The Tm-Ho transfer time using the value for k_{26} is similar to that found by the simple Forster-Dexter[28,29] model of energy transfer, utilizing spectral overlap integrals.[60] This result along with those of a four-wave mixing study [59,60] of energy migration in Tm^{3+}:YAG show conclusively that the overall process consists of two parts, a fast energy migration among Tm^{3+} ions followed by a process of energy transfer from Tm^{3+} to Ho^{3+}. The concentration dependence of the quantum efficiency of the $^3H_4$ emission indicates that this migration occurs in both the initial pump level (the $^3H_4$ multiplet) and in the metastable state (the $^3F_4$ multiplet). A second rate parameter, the rate parameter describing the Tm^{3+} $^3H_4 \rightarrow {}^3F_4$ and $^3H_6 \rightarrow {}^3F_4$ cross relaxation process, is also found from the data presented here. Note, however, that the rate parameters are determined only for the Tm^{3+} and Ho^{3+} concentration used in this work, which is similar to the optimum concentrations determined for Cr,Tm,Ho:YAG flashlamp pumped lasers.[48]

The second result of this work is the development and use of a rate equation model for a computer simulation of Tm,Ho:YAG laser operation. Since the usefulness of such a simulation depends entirely on the accuracy of the parameters used, all the parameters needed in the model are determined independently through analysis of the spectroscopic results and no fitting parameters are used in the simulation. The simulation accurately predicts temporal delays in the laser

output and reproduces the relaxation oscillations seen in this system. Additional effects due to various loss mechanisms in some cases change the predicted threshold for lasing, but do not affect the overall dynamics of the laser output.

Finally, the existence of a second process leading to the green emission reported in Tm,Ho:YAG (and in other hosts) is firmly established. For laser pumped lasers, this process, identified as the excited state absorption of pump photons by Ho^{3+} ions in the metastable state, can be as important as the ion-ion cross relaxation process usually cited. This mechanism is needed to explain the green emission dependence on pump wavelength while the ion-ion cross relaxation process explains the existence of green emission even when no excited state absorption of pump photons is present.

CHAPTER IV

SPECTROSCOPIC AND LASING PROPERTIES OF Nd:YAG AND Nd:GSGG

Introduction

For many years Nd^{3+} doped materials have played an important role in the field of solid state lasers and recently much work has concentrated on diode pumped laser operation [70–73] and simulating diode pumped laser operation with tunable solid state lasers [74–78]. Interest in potential new laser host materials and detailed examination of the dynamics involved in the pump process have spurred many studies. Additionally, studies of upconversion and excited state absorption processes leading to fluorescence [79–84] and laser operation from upper states [34,35] have been undertaken.

Results of a study of the absorption and emission characteristics of two different host materials, yttrium aluminum garnet and gadolinium scandium gallium garnet are presented here in an attempt to further understand the dynamics involved in monochromatically pumped systems. Absorption, fluorescence emission and excitation spectra are used to determine the origin and dynamics involved in the emission of photons in the blue and green spectral regions. Analysis of absorption data using the Judd-Ofelt theory [9,10] is performed and used to predict radiative lifetimes of excited states, branching ratios for radiative decay, and oscillator strengths for excited state absorption transitions. Mechanisms leading to the blue emission often reported in these and similar materials are identified.

Experimental Method

Absorption spectra and fluorescence spectra were obtained for two different Nd^{3+} doped oxide crystals. The following samples were used in the study: yttrium aluminum garnet doped with 1.0 % Nd^{3+} (Nd:YAG) and gadolinium scandium gallium garnet doped with 1.0% Nd^{3+} (Nd:GSGG). A Cary 2400 UV-VIS-NIR spectrophotometer was used to find the absorption spectra. Data was acquired, stored, and analyzed using an IBM-compatible personal computer.

Fluorescence spectra were obtained using a variety of excitation sources and spectrometers. A 0.25 m spectrometer was used for the GSGG sample and some preliminary work on the YAG sample. Additionally a 0.85 double spectrometer was also used for the YAG sample. Various photomultiplier tubes, depending on the spectral range of interest, were used. In all cases a PAR Model 162 boxcar averager was used for signal processing. Output from the averager was then converted to a digital signal and recorded on a computer data acquisition system. An alexandrite laser, tunable from 720 nm-800 nm with a pulse train consisting of 20-40 300 ns pulses, was used as the excitation source.

In addition to absorption and fluorescence spectra described above, excitation spectra were recorded for the GSGG sample. A 0.25 m spectrometer was used to select one of the emission lines. The alexandrite laser was then scanned over the range from 730-780 nm. A photomultiplier tube was used to detect the resulting emission in the visible region and a PbS cell was used to detect the emission for the near infrared emission. Again a PAR Model 162 boxcar averager was used for signal processing and data was stored on a computer. The energy of the alexandrite laser was monitored with a Laser Precision Model 7600 energy meter.

Results and Analysis

The absorption spectra and positions of some important multiplets are shown for the region from 10000-30000 cm^{-1} for Nd:YAG (Figure 18) and Nd:GSGG (Figure 19). Assignment of the term values to the various absorption regions is

based upon the crystal field analysis for Nd:YAG in Refs. [85,86] and for Nd:GSGG in Ref. [87]. Absorption spectra for transitions to the $^2P_{3/2}$ multiplet are shown in Figure 20(a) (Nd:YAG) and Figure 20(b) (Nd:GSGG). The positions of the Stark components of this multiplet may be important in determining the origin of emission seen in this work and previous work, [74,76–79] so the identification of their positions is extremely important. The extremely weak oscillator strength of transitions to this multiplet makes assignment of spectral lines difficult and the positions of both of the Stark components have been previously reported at low temperatures only. [85–87] Here these positions of the Stark components are identified from the splitting of the absorption spectrum as 26042 cm^{-1} and 25997 cm^{-1} for Nd:GSGG. For Nd:YAG, although the peaks are not very well resolved, the positions are identified as 25993 cm^{-1} and 25934 cm^{-1}. The other spectral features are due to transitions from the Stark split components of the ground state to the $^2P_{3/2}$ Stark levels.

The oscillator strengths for transitions originating in the ground state multiplet, those experimentally determined (Equation (18)) and those found from the Judd-Ofelt analysis (Equation (17)), are shown in Table IV for both samples. The Judd-Ofelt parameters determined here and those found by others [88–90] are listed in Table V. In both tables there are two entries for this work, corresponding to different integration limits on Equation (18). Two different groupings of certain multiplets are used for each sample and the results are compared.

The Judd-Ofelt parameters can be used to determine transition probabilities and oscillator strengths for excited state to excited state transitions using Equation (13) and (17). This can be done for all those transitions for which the transition matrix elements are available. For Nd^{3+} [20] gives matrix elements for 21 multiplets yielding 441 transitions. A portion of these results are shown in Tables VI, VII, and VIII.

Fluorescence spectra under excitation at 748.6 nm for Nd:YAG and 734.9 nm for Nd:GSGG in the 375-475 nm region are shown in Figures 21(a) and 21(b) and that in the 475-575 nm region is shown in Figures 22(a) and 22(b). The

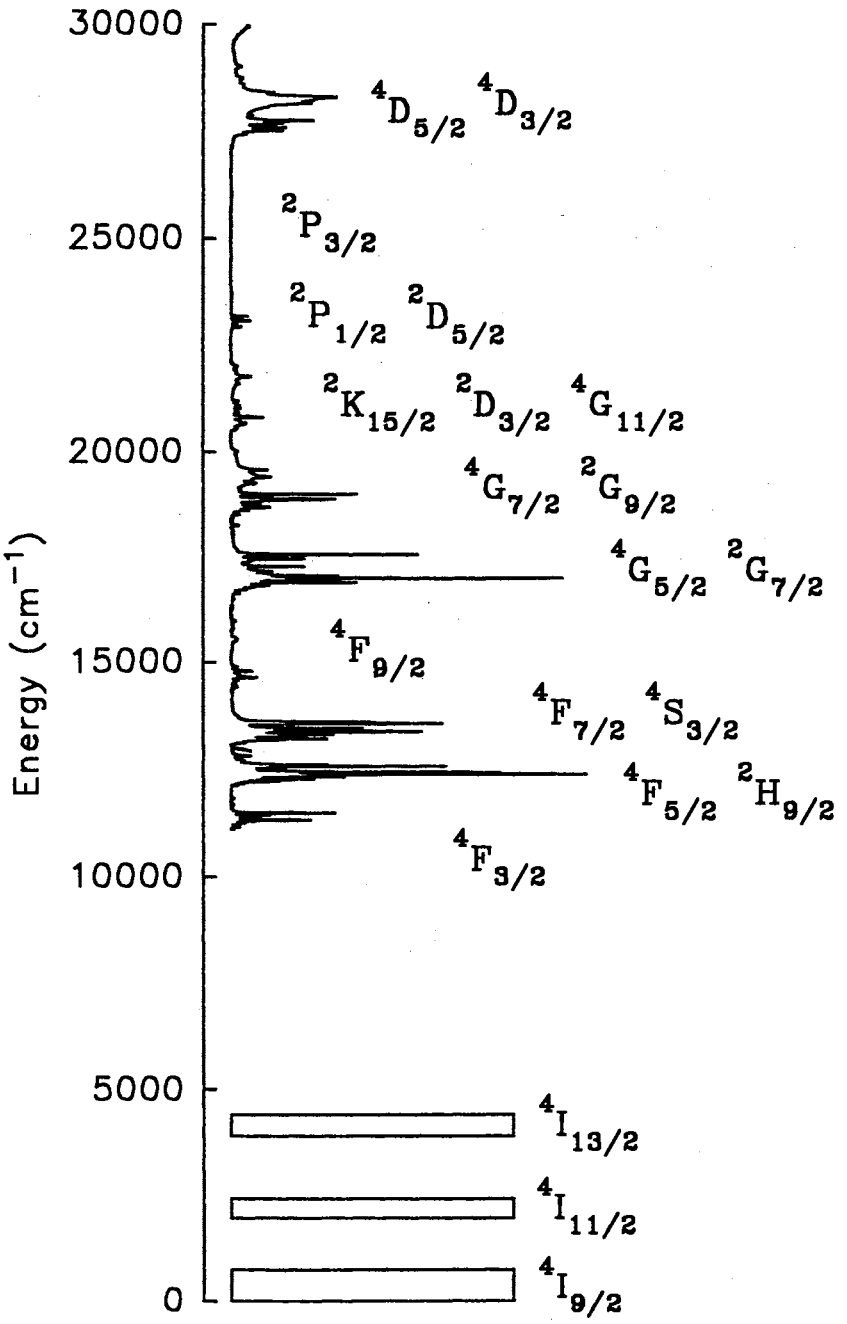

Figure 18. Absorption Spectrum of Nd:YAG. Positions of Lower Levels Taken from Ref. [85].

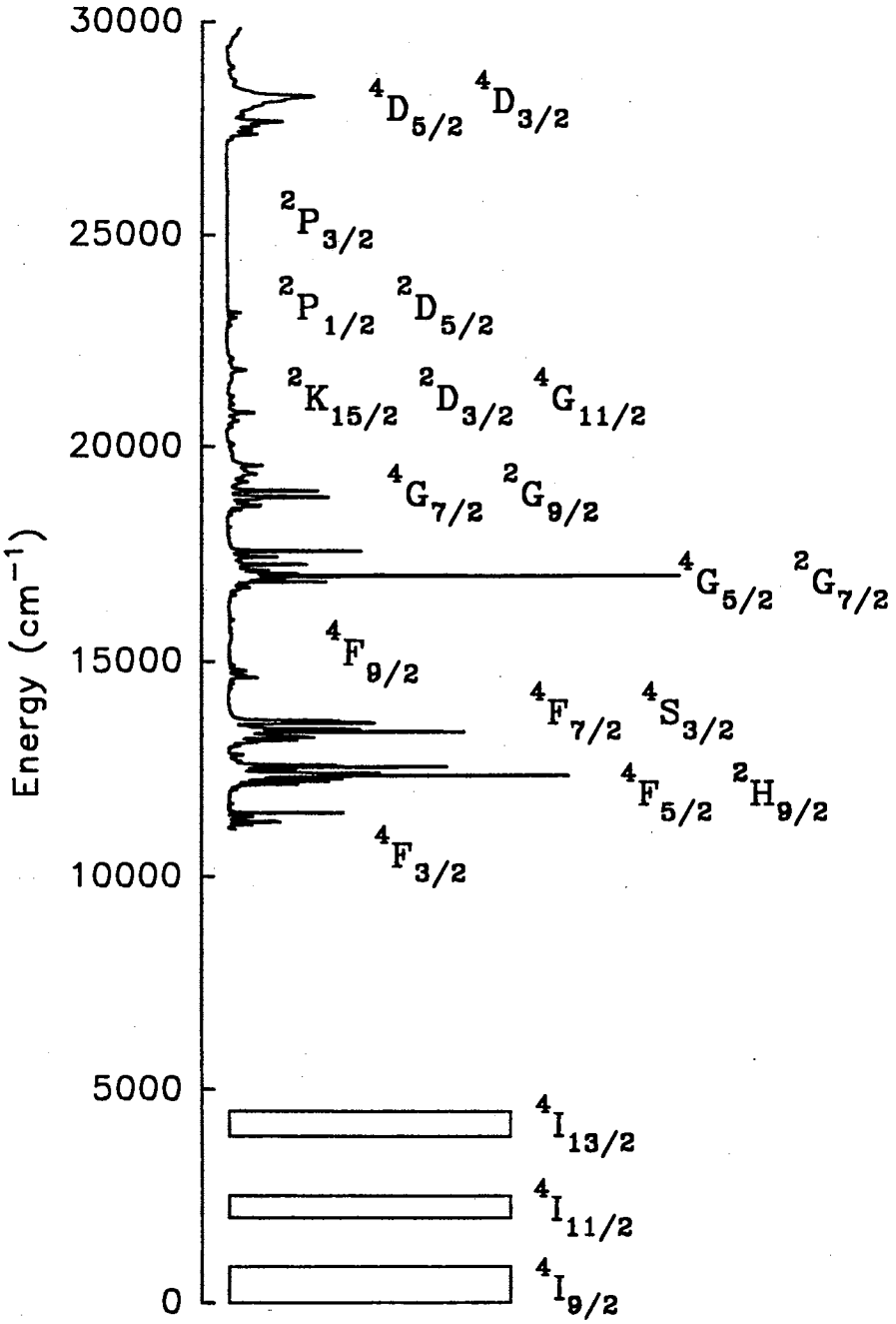

Figure 19. Absorption Spectrum of Nd:GSGG. Positions of Lower Levels Taken from Ref. [86].

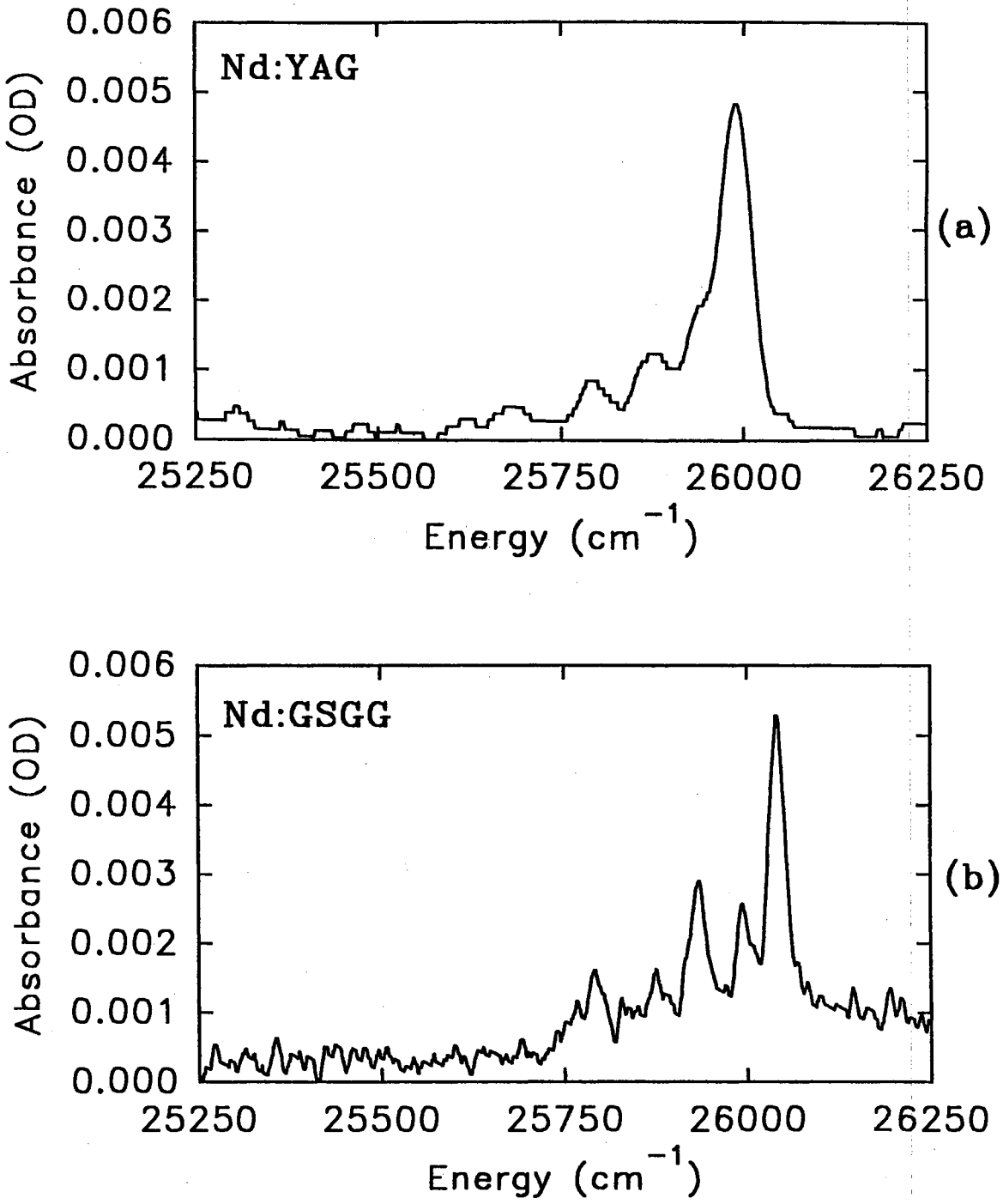

Figure 20. Absorption Spectra of $^2P_{3/2}$ Multiplet. (a) Nd:YAG and (b) Nd:GSGG.

TABLE IV

OSCILLATOR STRENGTHS FOR TRANSITIONS
FROM THE GROUND STATE
Nd:YAG AND Nd:GSGG

Band	Multiplet	Nd:YAG (1)			Nd:YAG (2)			Nd:GSGG (1)			Nd:GSGG (2)		
		λ (nm)	f ($\times 10^{-8}$) expt.	calc.	λ (nm)	f ($\times 10^{-8}$) expt.	calc.	λ (nm)	f ($\times 10^{-8}$) expt.	calc.	λ (nm)	f ($\times 10^{-8}$) expt.	calc.
5	$^4F_{3/2}$	879	126	183	879	126	183	878	139	175	878	139	173
6	$^4F_{5/2},^2H_{9/2}$	806	840	748	806	840	746	806	677	645	806	677	643
7	$^4F_{7/2},^4S_{3/2}$	747	768	867	747	768	865	746	688	720	746	688	722
8	$^4F_{9/2}$	683	69.5	62.9	683	69.5	62.8	681	64.0	53.3	681	64.0	53.3
9	$^2H_{11/2}$	636	34.0	17.5	636	34.0	17.5	641	26.0	14.9	641	26.0	14.8
10	$^4G_{5/2},^2G_{7/2}$	586	749	760	586	749	761	586	796	806	586	796	796
11	$^4G_{7/2}(2),^2K_{13/2}$	525	598	459	525	598	458	527	552	429	530	297	310
12	$^4G_{9/2}$										514	258	116
13	$^2D_{3/2},^2K_{15/2}$	473	220	78.2	481	118	55.7	474	187	71.1	480	112	51.1
14	$^4G_{11/2}$				459	106	22.1				459	87.5	19.5
15	$^2P_{1/2}$	434	32.3	44.9	434	32.3	44.8	433	39.2	49.8	433	39.2	48.8
16	$^2D_{5/2}$	423	2.85	4.14	423	2.85	4.13						
17	$^2P_{3/2}$	385	2.76	2.56	385	2.76	2.56	385	2.14	2.42	385	2.14	2.40
18	$^4D_{5/2},^4D_{3/2}$ $^4D_{1/2},^2I_{11/2}$	355	890	931	355	890	928	354	935	961	354	935	944

TABLE V

JUDD-OFELT PARAMETERS FOR
Nd:YAG AND Nd:GSGG

Material	Ω_2 ($\times 10^{-20}$)	Ω_4 ($\times 10^{-20}$)	Ω_6 ($\times 10^{-20}$)	RMS-Error
Nd:YAG(1)	0.56	2.55	5.03	17
Nd:YAG(2)	0.57	2.54	5.02	15
Nd:YAG[a]	0.20	2.7	5.0	10
Nd:YAG[b]	0.37	2.29	5.97	-
Nd:GSGG(1)	0.65	2.33	3.79	13
Nd:GSGG(2)	0.66	2.29	3.73	9.3
Nd:GSGG[c]	0.35	2.35	3.23	14

a Ref. [88]
b Ref. [89]
c Ref. [90]

TABLE VI

TRANSITION PROBABILITIES AND BRANCHING RATIOS FROM THE $^2P_{3/2}$ MULTIPLET FOR Nd:YAG AND Nd:GSGG

Terminal Multiplet	Nd:YAG			Nd:GSGG		
	λ (nm)	A (s^{-1})	β (%)	λ (nm)	A (s^{-1})	β (%)
$^4I_{9/2}$	385	101	2.55	385	111	2.71
$^4I_{11/2}$	419	652	16.5	420	774	18.9
$^4I_{13/2}$	459	556	14.1	455	570	13.9
$^4I_{15/2}$	501	127	3.21	519	110	2.68
$^4F_{3/2}$	685	4.39	0.111	686	6.55	0.16
$^4F_{5/2}$	737	25.3	0.641	737	30.6	0.747
$^2H_{9/2}$	737	1140	28.9	737	1110	27.1
$^4F_{7/2}$	794	4.09	0.104	796	4.78	0.117
$^4S_{3/2}$	794	7.04	0.178	796	10.3	0.251
$^4F_{9/2}$	882	638	16.1	886	648	15.8
$^2H_{11/2}$	976	131	3.31	964	142	3.47
$^4G_{5/2}$	1120	2.37	0.0599	1120	3.47	0.0848
$^2G_{7/2}$	1120	0.00	0.00	1120	0.00	0.00
$^4G_{7/2}$	1440	5.64	0.143	1430	7.2	0.176
$^4G_{9/2}$	1440	161	4.07	1430	171	4.17
$^2K_{13/2}$	1440	392	9.92	1430	390	9.52
$^2D_{3/2}$	2070	0.326	0.00825	2050	0.502	0.0122
$^4G_{11/2}$	2070	1.23	0.0311	2050	1.48	0.036
$^2K_{15/2}$	2070	4.28	0.108	2050	4.24	0.104
$^2P_{1/2}$	3410	0.0755	0.00191	3470	0.109	0.00266
$^2D_{5/2}$	4290	0.0513	0.00130	3470	0.151	0.00369

TABLE VII

SUMMARY OF RADIATIVE LIFETIMES AND BRANCHING RATIOS TO THE ^4I_J MULTIPLETS FOR Nd:YAG AND Nd:GSGG

Terminal Multiplet	Nd:YAG			Nd:GSGG		
	λ (nm)	τ μs	β (%)	λ (nm)	τ μs	β (%)
$^4I_{11/2}$	4760	58600		4620	51700	
$^4I_{13/2}$	2380	15500		2510	19900	
$^4I_{15/2}$	1670	19000		1490	10100	
$^4F_{3/2}$	879	270	100	878	264	100
$^4F_{5/2}$	806	200	99.8	806	197	100
$^2H_{9/2}$	806	1250	100	806	1300	100
$^4F_{7/2}$	747	180	100	746	190	100
$^4S_{3/2}$	747	152	100	746	162	100
$^4F_{9/2}$	683	230	99.7	681	239	99.7
$^2H_{11/2}$	636	3780	91.3	641	3830	92.3
$^4G_{5/2}$	586	104	98.6	586	88	98.5
$^2G_{7/2}$	586	237	97.2	586	212	97.4
$^4G_{7/2}$	525	146	92	527	127	93
$^2K_{13/2}$	525	915	47.9	527	968	48.9
$^4G_{9/2}$	525	131	94.6	527	119	95
$^2D_{3/2}$	473	397	76.8	474	393	77.2
$^4G_{11/2}$	473	99.1	90.7	474	93.6	90.8
$^2K_{15/2}$	473	681	33.6	474	693	33
$^2P_{1/2}$	434	235	64.7	433	202	62.2
$^2D_{5/2}$	423	443	30.7	433	490	31.8
$^2P_{3/2}$	385	253	36.3	385	244	38.2

TABLE VIII

OSCILLATOR STRENGTHS FOR TRANSITIONS
TO THE $^2P_{3/2}$ MULTIPLET FOR
Nd:YAG AND Nd:GSGG

	Nd:YAG			Nd:GSGG		
Initial Multiplet	λ (nm)	f ($\times 10^{-8}$)	ΔE (cm^{-1})	λ (nm)	f ($\times 10^{-8}$)	ΔE (cm^{-1})
$^4F_{3/2}$	685	0.924	-1230	686	1.20	-972
$^4F_{5/2}$	737	4.11	-200	737	4.33	-200
$^2H_{9/2}$	737	111	-200	737	94.4	-200
$^4F_{7/2}$	794	0.579	775	796	0.598	1040
$^4S_{3/2}$	794	1.99	775	796	2.57	1040

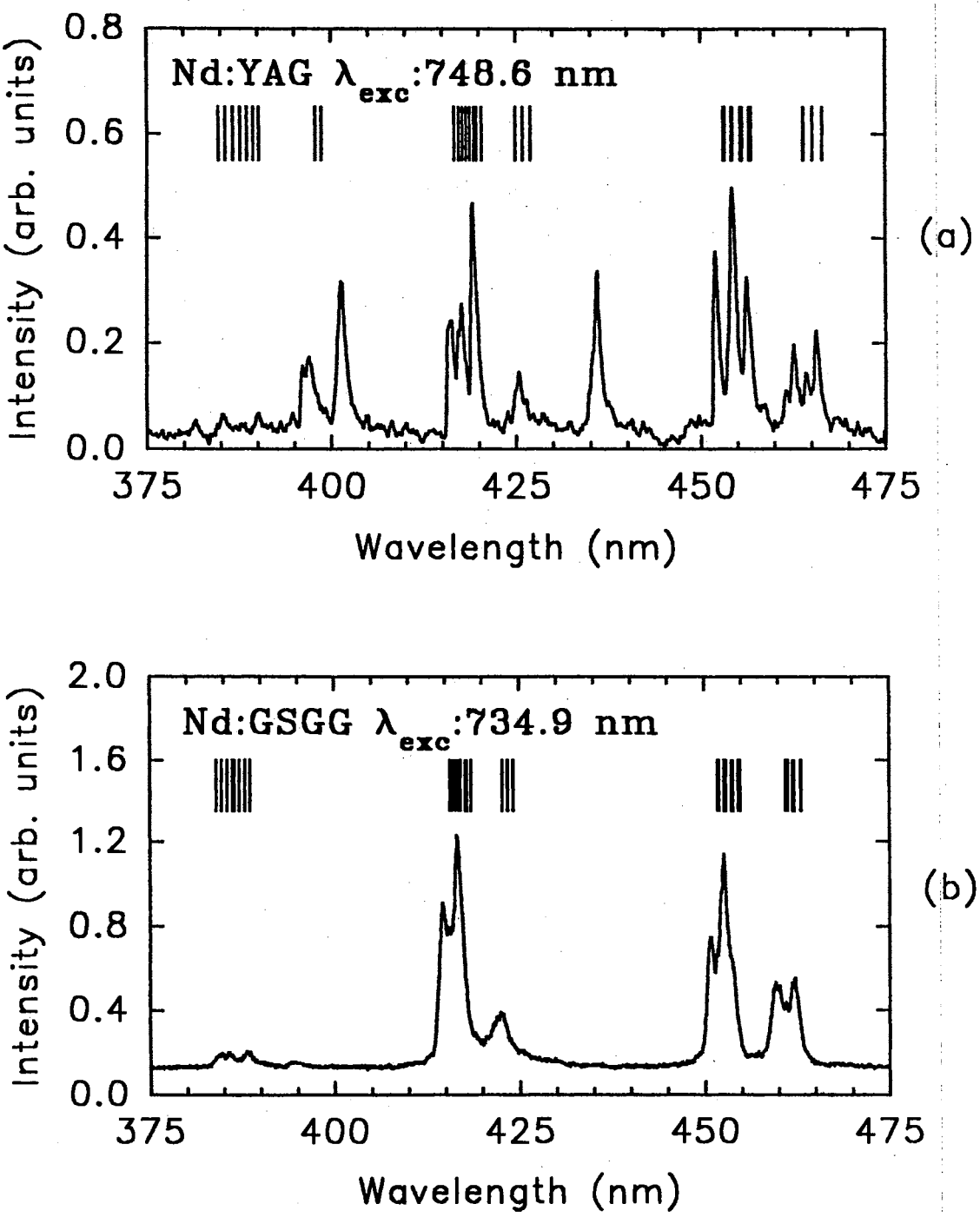

Figure 21. Fluorescence Spectra in 375-475 nm Spectral Range. (a) Nd:YAG and (b) Nd:GSGG. The Vertical Lines Indicate Emission Wavelengths Predicted by the Positions of the Stark Components of the $^2P_{3/2}$ and ^4I_J Multiplets.

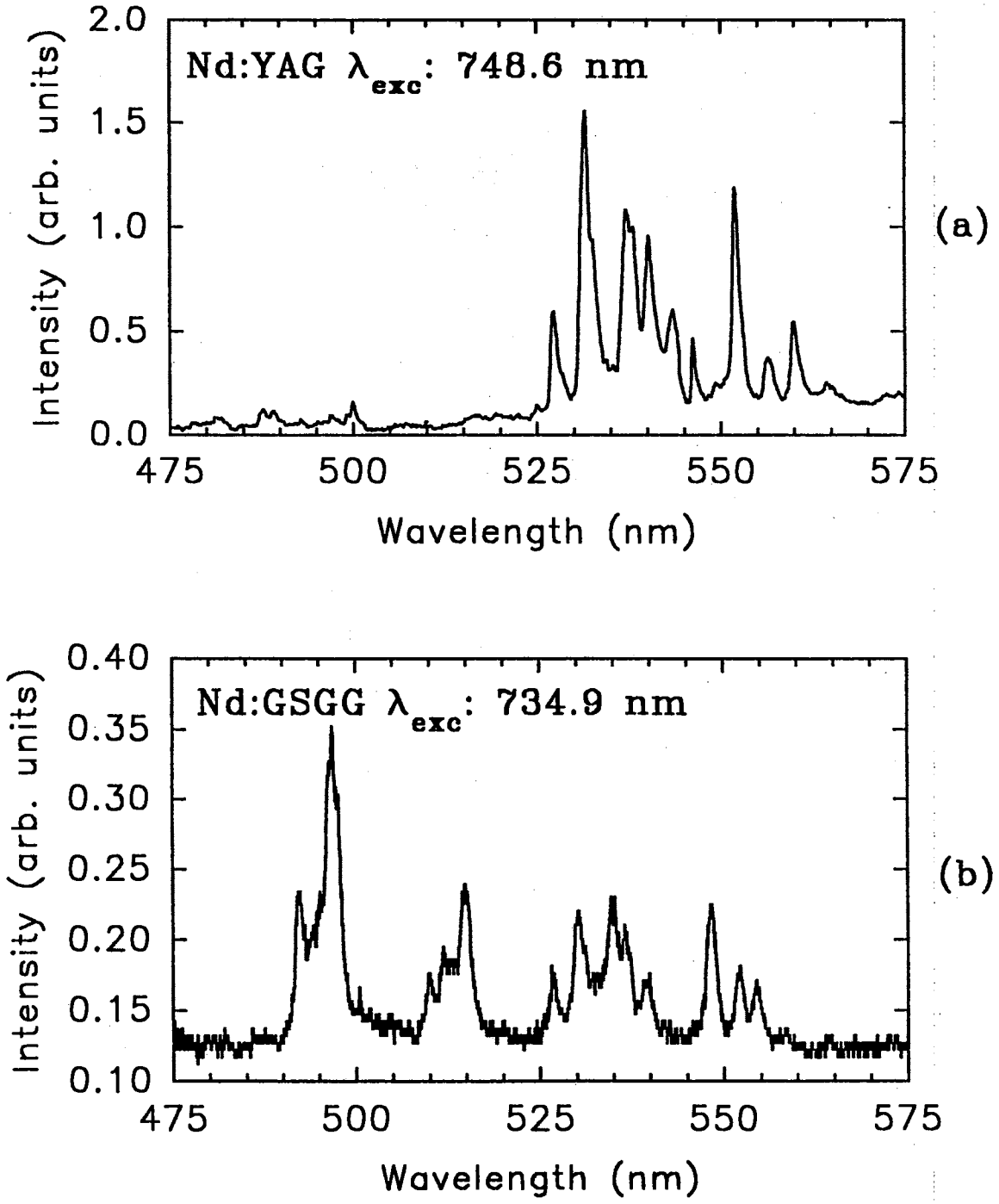

Figure 22. Fluorescence Spectra in 475-575 nm Spectral Range. (a) Nd:YAG and (b) Nd:GSGG.

alexandrite pump wavelengths for the samples differ slightly but in both cases the absorption band corresponding to the $^4F_{7/2} + {}^4S_{3/2}$ is excited directly. The presence of emission at higher energies than that of the pump photons indicates some type of multiple body process, ion-ion energy transfer upconversion, reabsorption of emitted photons, or excited state absorption of pump photons, occurs.

Determining the exact dynamics involved in this process would be extremely difficult considering the number and location of the multiplets present in the system. To help in determining the processes involved, excitation spectra for some of the emission peaks observed in the GSGG sample are presented in Figure 23. Excitation spectra for the 417 nm line, the 536 nm line, and the 1064 nm line are shown along with the absorption spectrum for transitions originating on the ground state in this spectral region. The 417 nm excitation spectrum contains peaks not seen in the other spectra. Additionally, the spectrum for the 417 nm emission line cuts off much more rapidly at wavelengths larger than 760 nm. The 536 nm and 1064 nm excitation spectra closely resemble the standard absorption spectrum for the region. These results are similar to those previously reported for Nd:YAG in [77].

Discussion of Results

Absorption

The results of the Judd-Ofelt analysis leads to some interesting conclusions. Two different sets of results and parameters found in the analysis for each sample along with previous results are listed in Tables IV and V. The two different sets of results and parameters in this work correspond to different methods of grouping the various multiplets when using Equation (18). For the entries labeled A the term assignments used are those found in Hua et al.[85]. An alternative grouping of the multiplets is used for the entries labeled B. In both cases for both samples an error within the 5-20 % usually encountered in these calculations is found.

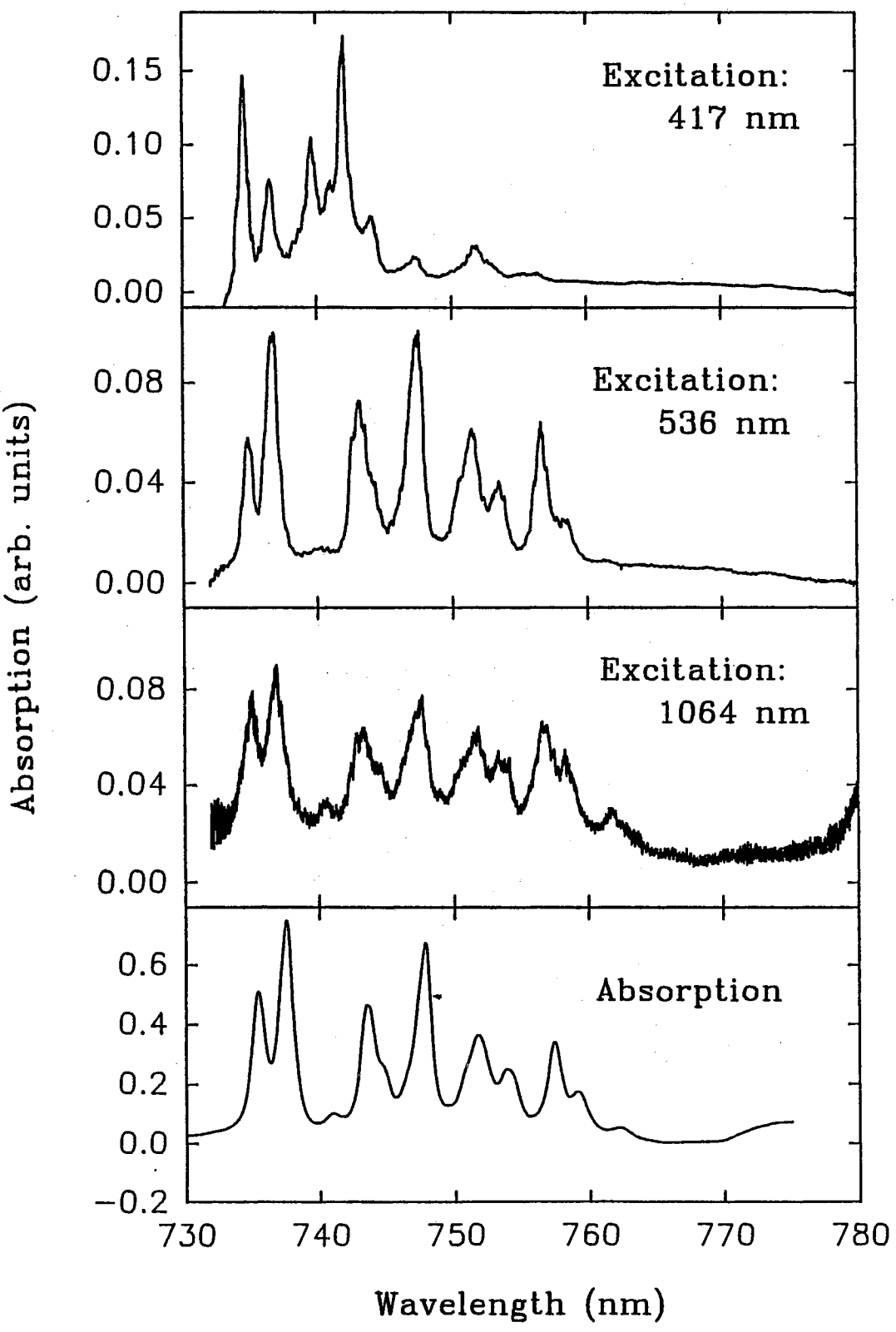

Figure 23. Nd:GSGG Excitation and Absorption Spectra 730-780 nm. Emission at (a) 417 nm, (b) 536 nm, (c) 1064 nm, and (d) Absorption Spectrum.

The Judd-Ofelt parameters determined are very close to those found previously by other authors. [88–90]

The grouping used for the results labeled A differs slightly from that used by others, especially in the region of 440-500 nm. This region of the absorption spectra for both samples is shown in Figure 24. This region corresponds to absorption by the $^2D_{3/2}$, $^2K_{15/2}$, and $^4G_{11/2}$ multiplets.

In the past, the absorption in this region was broken into two regions, one below and one above $\approx$ 470 nm. Term values were assigned to each of these regions individually.

These terms are not separated in the entries labeled A because of the extensive mixing of the Stark components of the three multiplets in this region [85–87] and the absorption spectra in the region. As seen from the spectra, determining the exact location to place the limits on the integration found in Equation (18) is difficult. The same problem is encountered in the 500-550 nm region for Nd:GSGG. For comparison. to previous work, the results of the analysis for the case in which these bands are separated are also listed (case B).

Comparison of the results for both cases and to those found previously show little difference. Although the rms-error is slightly reduced in case B, the differences between the measured and predicted oscillator strengths remain essentially the same. The increase in the number of transitions used in the second method does not lead to a significant reduction in the overall error associated with the calculation or lead to a significant change in the Judd-Ofelt parameters. When comparing these results to those found for these materials by others, the only significant difference is in the Ω_2 parameter. The value found here seems consistently larger than that reported elsewhere. For Nd^{3+} doped materials, the Ω_t parameter is not as reliable as the Ω_4 and Ω_6 parameters.[88] Ω_2 only depends on one absorption band, the $^4G_{5/2} + {}^2G_{7/2}$ band. The ratio of this oscillator strength to that of the $^4F_{5/2} + {}^4S_{3/2}$ band found here is larger than that found by others: 1.18 vs. 0.79 for GSGG and 0.89 vs 0.45 for YAG. This leads to a higher value for Ω_2. If this band is completely eliminated from the analysis and Ω_2 set to 0.00, as done by Krupke [88],

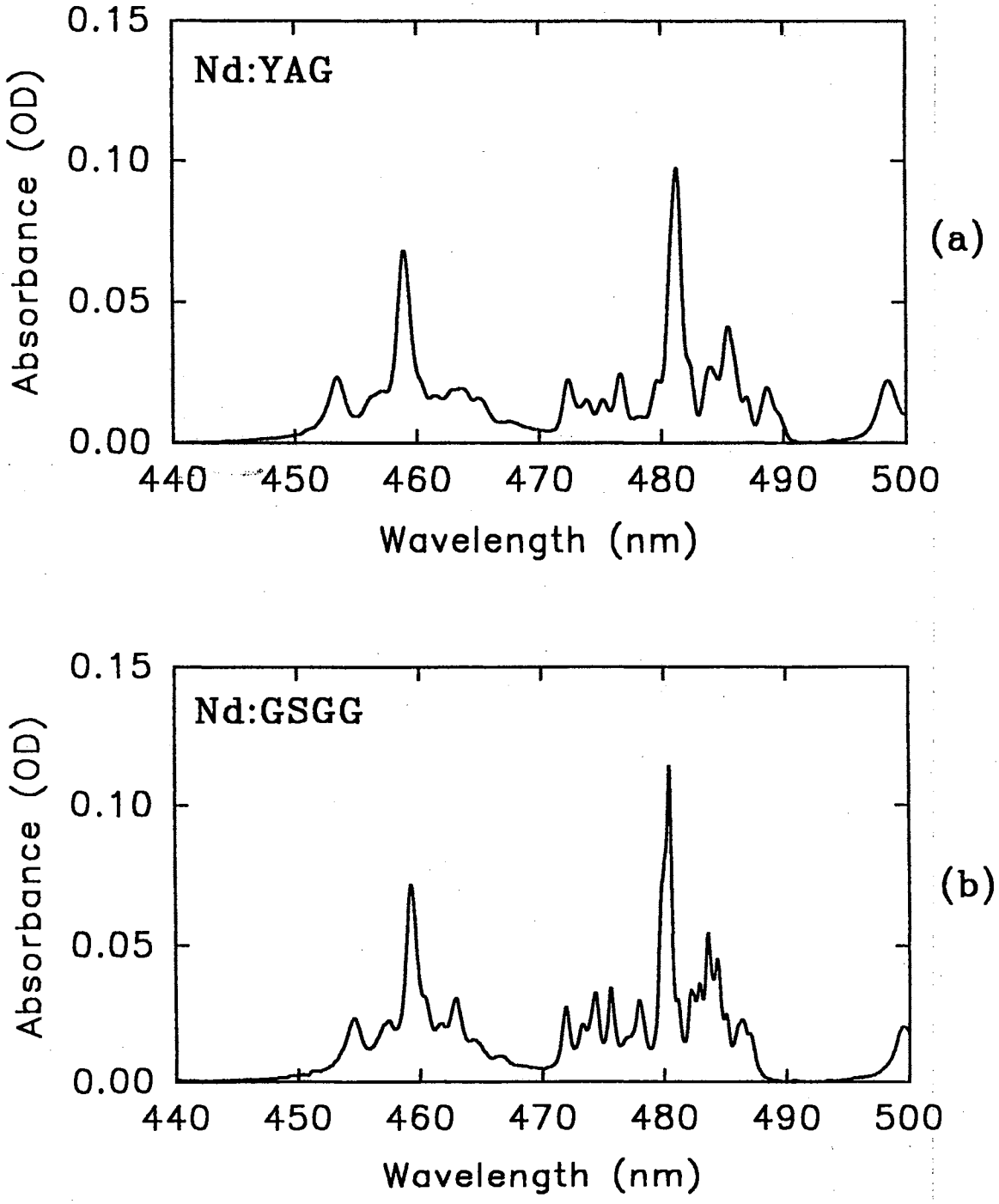

Figure 24. Absorption Spectra in 440-500 nm Spectral Range. (a) Nd:YAG and (b) Nd:GSGG.

the results for Ω_4 and Ω_6 remain essentially unchanged. Analysis of the various doubly reduced unit tensor matrix elements indicates that slight differences in Ω_2 will not greatly affect any of the important transitions in the system.

Tables VI-VIII summarize much of the information acquired through the application of Equations (13, 16, and 17). In Table VI the transition probability rates for all transitions originating on the $^2P_{3/2}$ multiplet are listed along with the predicted branching ratios. Analysis of these values shows that a significant portion of the radiative emission occurs to states above the metastable state. From these states ions can either cascade non-radiatively to the metastable state or radiatively decay to a still lower level. In all cases, only a fraction of the ions excited to states above the metastable state bypasses the metastable state via fluorescence to the ^4I_J multiplets. Table VII summarizes the radiative lifetimes and the branching ratio to states below the metastable state. For those cases in which the lifetime has been experimentally measured [23–25,81,91] the measured lifetimes are significantly shorter than those listed here. This indicates that the non-radiative decay path for ions excited to these states is the dominant relaxation process.

In Table VIII the oscillator strengths for transitions between excited states that may be responsible for the excited state absorption of pump photons are listed. The ΔE noted is the energy deficiency (excess) involved in a transition terminating on the $^2P_{3/2}$ originating on one of these levels. It is interesting to note that the oscillator strength for a transition originating on the $^4F_{5/2} + {}^2H_{9/2}$ band is $\approx$100 times larger than that originating on the metastable state for both materials. A complexity in quantitatively determining the absorption cross sections for transitions in the spectral corresponding to these transitions is that the actual transition involved in an absorption process would be a Stark level to Stark level transition and not a multiplet to multiplet transition as calculated here. Calculation of Stark level to Stark level oscillator strengths is possible [92,93] but requires detailed knowledge of the radial wavefunctions for individual Stark levels which is not generally available.

Fluorescence

Analysis of the emission spectra in Figures 21 and 22 can be used to establish the origin of the blue emission observed here. The emission is broken into three main bands for each sample, corresponding to emission from the $^2P_{3/2}$ to the $^4I_{13/2}$, $^4I_{11/2}$, and $^4I_{9/2}$ multiplets. The vertical lines in Figure 21 are the wavelengths of predicted emission from the $^2P_{3/2}$ multiplet determined from the positions of the Stark levels identified earlier and the Stark level positions for the lower multiplets in Ref. [85,87]. Most of the lines observed correspond well with the predicted emission. The absence of large numbers of additional lines indicates little contribution from other higher lying multiplets, especially in the GSGG sample.

Previous work [34,74,76–80,82,83] has attributed the blue fluorescence in the 380 nm, 420 nm, 450 nm, and 460 nm regions to transitions originating on the $^4D_{5/2}$, $^4D_{3/2}$, and $^2P_{3/2}$ multiplets. The mechanisms cited for populating the upper state was excited state absorption (ESA) from the metastable state (either of pump or fluorescence photons) and ion-ion energy transfer upconversion (ETU) involving ions in the metastable state.

Some of these mechanisms are shown in Figure 25. Figure 25(a) shows possible ESA processes and Figure 25(b) shows possible ETU processes. The origin and dynamics of the blue and green emission is difficult to determine exactly. There are a number of different mechanisms which could lead to this emission and a number of possible upper states that could be the origin level. From experimental evidence and energy considerations, a number of these are shown to be less probable than others. Results indicate that processes involving the metastable state may not be the important process and ETU involving the pump and intermediate levels and/or ESA of pump photons from an intermediate state, process II in Figures 25(a) and 25(b), are the dominant mechanisms leading to blue emission.

The spectra in Figure 21 shows emission in the 380 nm region. The energy of a 735 nm pump photon alone is not large enough to excite an ion in the metastable state to the proposed upper state. (see ΔE in Table VIII) It is possible that the

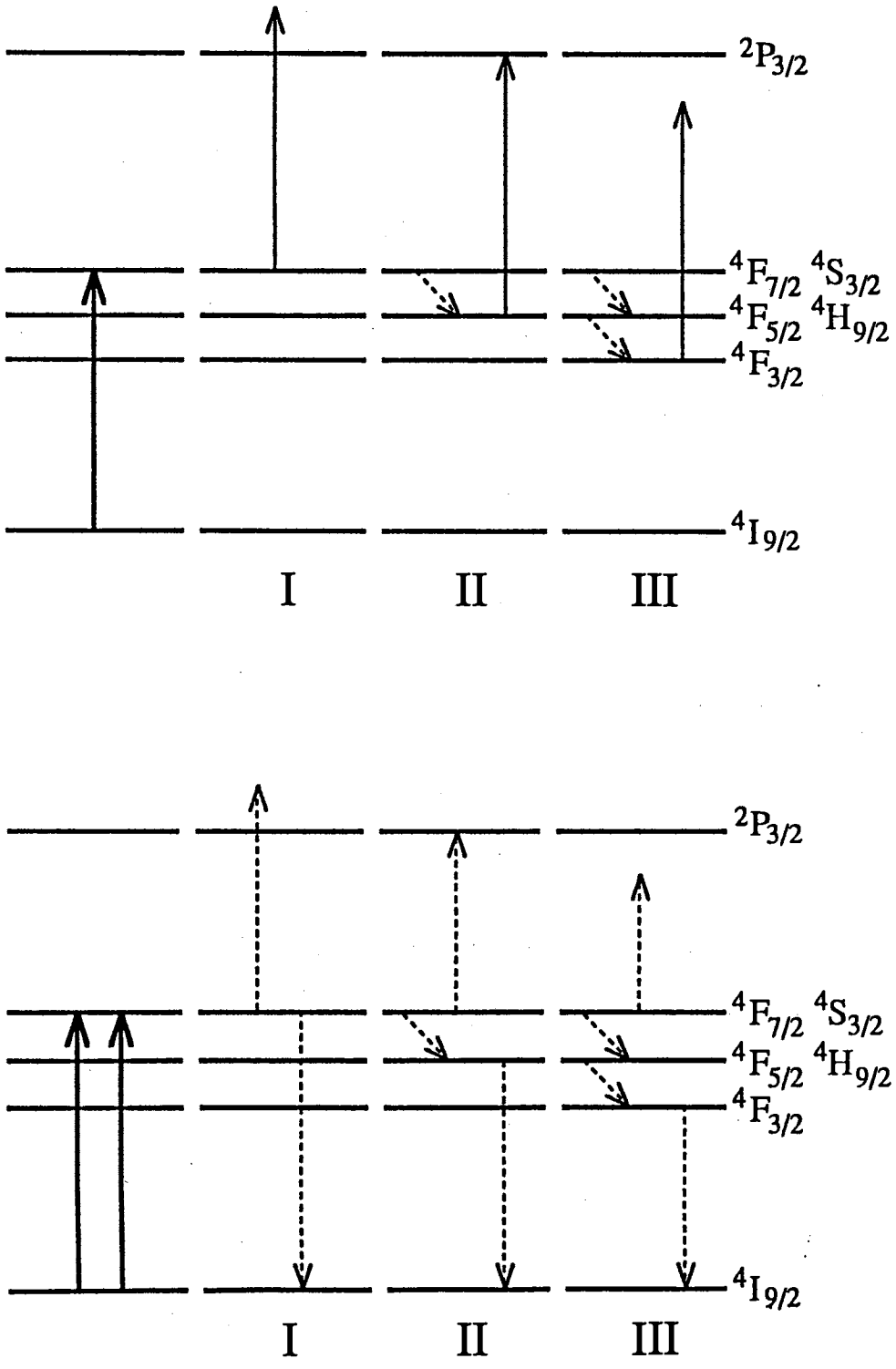

Figure 25. Possible Upconversion Processes. The Top Portion Shows Three Different Excited State Absorption Processes and the Lower Portion Shows Three Different Ion-Ion Energy Transfer Processes.

transition is phonon assisted but this requires absorption of a phonon with an energy of ΔE 1000 cm^{-1} . Although such high energy phonons may be present, at room temperature their number should be small. Additionally, the oscillator strength for the transition determined from the Judd-Ofelt analysis is much smaller than that for other transitions (Table VIII). Energy conservation also indicates that ETU involving ions in the metastable state is not the dominant process. Energy conservation for a transition involving the interaction of a metastable state ion with that of another metastable state ion or an ion in the intermediate band or pump band requires phonons with energy between 1000-3000 cm^{-1} .

Energy transfer upconversion involving ions in the pump and intermediate states could be a resonant process (Figure 25 II). Additionally, ESA of pump photons from the intermediate level (the $^4F_{5/2} + {}^2H_{9/2}$ levels) is also a resonant process. If energy transfer upconversion is the dominant process then dramatic differences between the ground state absorption spectra and the excitation spectra for the emission are not expected. As long as ions are present in the Stark components of the multiplets involved the process occurs and emission is present.

Excitation spectra for GSGG for the emission at 417 nm is found to be much different than the ground state absorption spectra for the pump region (Figure 23). This is similar to the behavior that was found in YAG [77]. In both cases there are pump wavelengths for which there is strong absorption of the pump photons by the ground state but weak blue fluorescence and regions of weak ground state absorption with strong blue fluorescence. This suggests that the process is very sensitive to pump wavelength and indicates the dominant process is ESA of pump photons rather than ETU.

The Judd-Ofelt analysis can be used to help confirm the identity of the upper level involved in the blue emission by comparing predicted and measured branching ratios. It is known from the Judd-Ofelt analysis that emission from the $^2P_{3/2}$ manifold occurs at wavelengths throughout the visible and near infrared spectral regions. Emission from lower manifolds will overlap this emission in many cases. Thus determining the total integrated intensity of emission and the absolute

branching ratios from the $^2P_{3/2}$ multiplet is not possible. The integrated intensities and relative branching ratios for some of the transitions originating on the $^2P_{3/2}$ multiplet can be determined from Figure 21 and 22. Table IX shows these results and the predicted branching ratios. Only the emission to the three lowest multiplets found in Nd:YAG and Nd:GSGG is considered. It is assumed that the emission to $^4I_{13/2}$ is the amount predicted by the Judd-Ofelt analysis. This value is then used to find the total integrated intensity allowing the branching ratios to the other two lower multiplets to be calculated and compared to those determined from the Judd-Ofelt analysis. Note that the results for GSGG are closer to those predicted than those for YAG. Analysis of the emission from YAG (Figure 21 and 22)) shows a number of lines that can not be assigned to the $^2P_{3/2}$ multiplet. The strong line near 401 nm is the best example of this and has been assigned to the $^2L_{17/2}$ [94]. Additional lines in the spectrum not attributed to $^2P_{3/2}$ are not included in the integrated intensity calculation. However, it is possible that some of the emission in the regions associated with the $^2P_{3/2}$ emission is actually originating on higher lying states and affects the results. The similarities, however, between the predicted and experimentally determined branching ratios indicates the accuracy of the assignment of the $^2P_{3/2}$ manifold as the origin level.

Figure 22 shows emission in the 475-575 nm region. The generation of this green emission is usually attributed to ETU or ESA of NIR photons involving metastable state ions. The excitation spectra of green emission does not show the same wavelength dependence as the blue emission (Figure 21) and is nearly identical to the excitation spectra for the NIR emission and ground state absorption spectra. Energetically, ETU involving ions in the metastable state or ESA of photons at the NIR laser wavelength by metastable state ions can produce excited ions in the multiplets from which green emission is likely to occur. The fact that this emission occurs at pump wavelengths where the blue emission is absent indicates a separate mechanism than that yielding blue emission is responsible. The number of possible upper states and processes involved is such that a detailed assignment of the dynamics is not feasible.

TABLE IX

INTEGRATED INTENSITIES AND COMPARISON OF BRANCHING RATIOS

Initial Multiplet:	$^2P_{3/2}$		
Terminal Multiplet:	$^4I_{9/2}$	$^4I_{11/2}$	$^4I_{13/2}$
Nd:YAG			
Integrated Intensity	13.4	119	84.3
Measured Branching Ratio	1.59	14.1	9.99
Predicted Branching Ratio	2.55	14.1	16.5
Nd:GSGG			
Integrated Intensity	34.2	255	233
Measured Branching Ratio	2.54	18.9	17.3
Predicted Branching Ratio	2.71	18.9	13.9

Summary and Conclusions

In summary, the combination of a detailed Judd-Ofelt analysis with fluorescence emission and excitation experiments allows for a more detailed analysis of the dynamics involved in monochromatically pumped Nd^{3+} materials. The results of both methods of performing the band groupings in the Judd-Ofelt analysis are similar. The analysis using the multiplet positions from the recent crystal field study by [85–87] is as accurate as that performed previously. Separation of the various manifolds in regions where the Stark components are highly interleaved is shown to be unnecessary.

The origin of a significant portion of the blue emission seen under alexandrite laser excitation is also established. Accurate positions of the Stark components for the upper state and the terminal levels allow for a detailed comparison of observed and predicted emission peaks. This information, combined with comparison of predicted to measured branching ratios, leads to the assignment of the $^2P_{3/2}$ manifold as the origin level for much of the blue emission. The observation of emission at wavelengths not able to be assigned to transitions originating in this state indicates that additional levels and processes are also involved in some cases.

The dynamics involved in producing emission at energies greater than those of the pump photons are also identified here. There are two separate mechanisms, one leading to emission in the 375-475 nm region and one leading to emission in the 475-575 nm region. Emission in the 475-575 nm region shows little pump wavelength dependence and involves energies that are reachable by ion-ion interactions involving metastable state ions or the absorption of photons at NIR wavelengths by metastable state ions. The emission in the shorter wavelength region shows a dramatically different pump wavelength dependence and the energies involved are such that it is unlikely that the metastable state is involved. Additionally, the oscillator strength for excited state absorption of pump photons from the $^4F_{5/2}$,$^2H_{9/2}$ multiplets is found to be 100 times weaker than that from the level immediately

above it. This transition is also found to be nearly resonant at the pump wavelengths producing blue emission and non-resonant for pump wavelengths not producing blue emission. Thus it seems likely that the upconversion process involved in generating blue emission originates on this intermediate band and not on the metastable state.

CHAPTER V

SPECTROSCOPIC AND LASING PROPERTIES OF Nd:ZBAN

Introduction

Another material for use in diode pumped laser systems is Nd^{3+} doped fluoride glass. Although laser systems based on rare-earth doped heavy metal fluoride glasses, both in bulk and fiber form, have been reported previously, [95–97] the lasing properties of Nd^{3+} in this type of host have been reported only in a fiber configuration. The results of a study of the spectroscopic and laser properties of Nd^{3+} doped heavy metal fluoride glass in bulk form, including the results of a Judd-Ofelt analysis, are reported here. An alexandrite laser, to simulate diode laser pumping, is used to investigate the laser operation of this material. Two different methods are used to determine the emission cross section of the $^4F_{3/2}$-$^4I_{11/2}$ transition and the results are compared to those reported for an oxide glass, an oxide crystal, and a fluoride crystal host.

Blue and green emission from levels above the metastable state, common in Nd^{3+} doped materials, is observed here and is found to be associated with excited state absorption (ESA) of pump photons. The oscillator strengths for the various excited state absorption transitions that could produce this emission are determined from a Judd-Ofelt analysis in an effort to understand the processes producing this emission. The effect of one of these processes on the slope efficiency is modeled using a rate equation approach [98] and the results provide information on the importance of the excited state absorption on monochromatically pumped Nd:ZBAN laser systems. This model is also used to qualitatively discuss the effects

of the ESA mechanism on the efficiency of laser systems based on other Nd^{3+} materials.

Results and Analysis: Spectroscopic Properties

Spectroscopic measurements were made on a sample of Nd^{3+} in ZBAN fluoride glass of dimensions 0.945 × 0.720 × 0.335 cm. The sample used in the study had a mole % composition as follows: 53.33% ZrF_4; 19.84% BaF_2; 3.14% AlF_3; 18.70% NaF; and 5.0% NdF_3 (ZBAN:Nd). The room temperature absorption spectra covering the spectral ranges of 250-2500 nm and 2500-3600 nm were measured using a Perkin-Elmer 330 Spectrophotometer and a Beckman Model 4240 Spectrophotometer, respectively. The absorption spectra and corresponding energy levels are shown in Figure 26. They agree well with earlier results for Zr-Ba-Nd based fluoride glass [99]. The widths of the energy levels shown in Figure 26(c) are determined from the full width half maximum (FWHM) of the corresponding absorption peaks and are associated with the unresolved Stark levels of the upper and lower multiplets involved in the transition. Figure 26(b) is an enlargement of the room temperature absorption spectrum shown in Figure 26(a) and exhibits the positions of the $^2P_{3/2}$, $^2D_{5/2}$, and $^4D_{3/2}$ multiplets. These levels have been found to be involved with excited state absorption of pump photons when monochromatically pumping into the $^4S_{3/2}$+$^4F_{7/2}$ and $^2H_{9/2}$+$^4F_{5/2}$ levels of Nd^{3+} doped materials [77,80,82–84]. The absorption spectrum of Nd^{3+} in ZBAN glass covering the spectral range of 720-820 nm is shown in Figure 27. This corresponds to the spectral range of a tunable alexandrite laser.

Emission spectra and lifetime measurements were made using a nitrogen laser-pumped dye laser system. The dye laser contained Rhodamine 590 dye lasing at 575 nm and had a pulse duration of 10 ns. Emission from the sample over the spectral range of 760-1180 nm was focused into a 1 m Spex monochromator and detected by an RCA 7102 photomultiplier tube. The emission spectrum was recorded with the use of a PAR Model 164 Boxcar Integrator and a strip chart

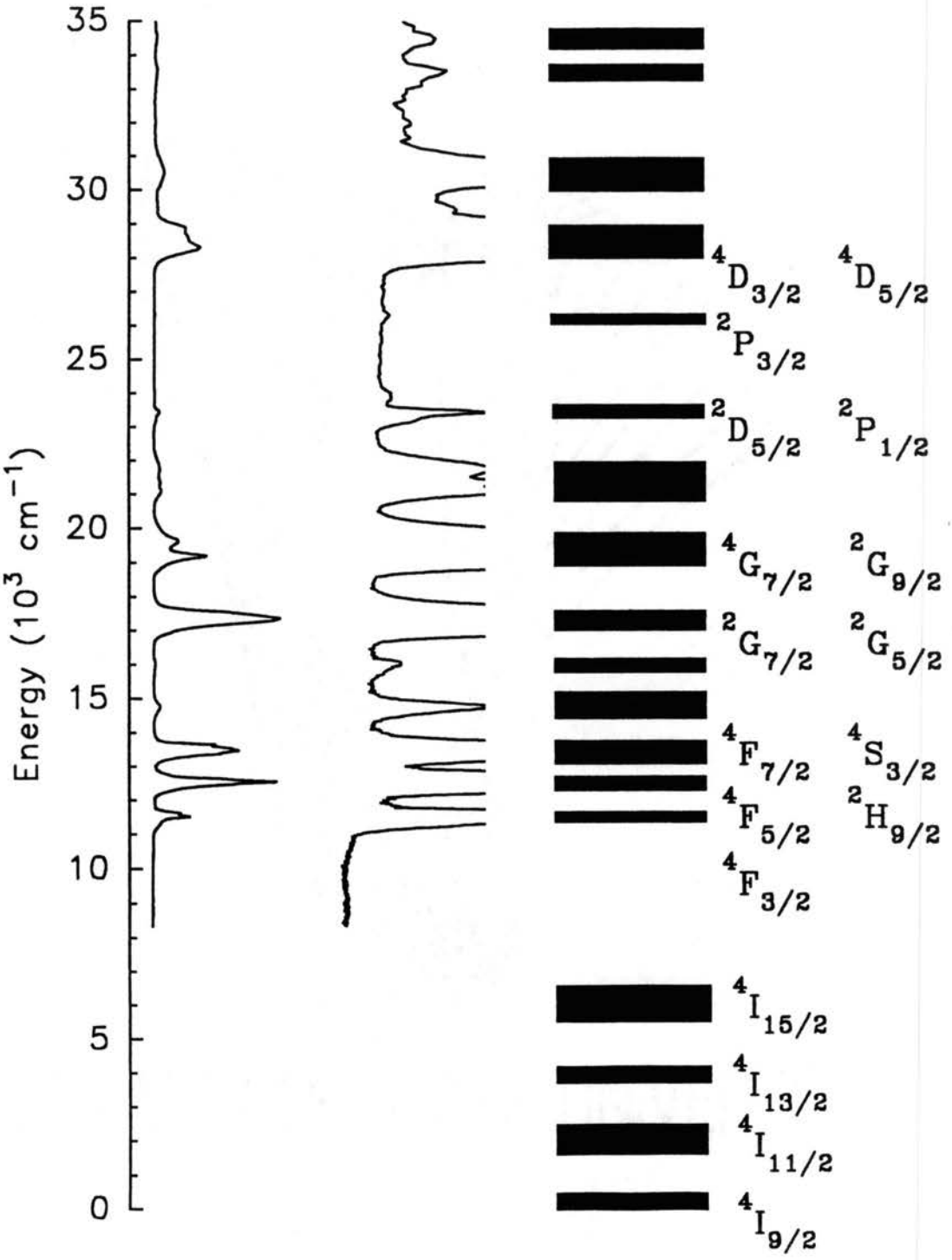

Figure 26. Absoption Spectra and Energy Level Diagram in Nd:ZBAN. (a) Absorption Spectrum of Nd:ZBAN.(b) The Absorption Spectrum in (a) Expanded to Show Details. (c) Energy Level Diagram of Nd:ZBAN with Widths Calculated from the FWHM of the Absorption Spectra.

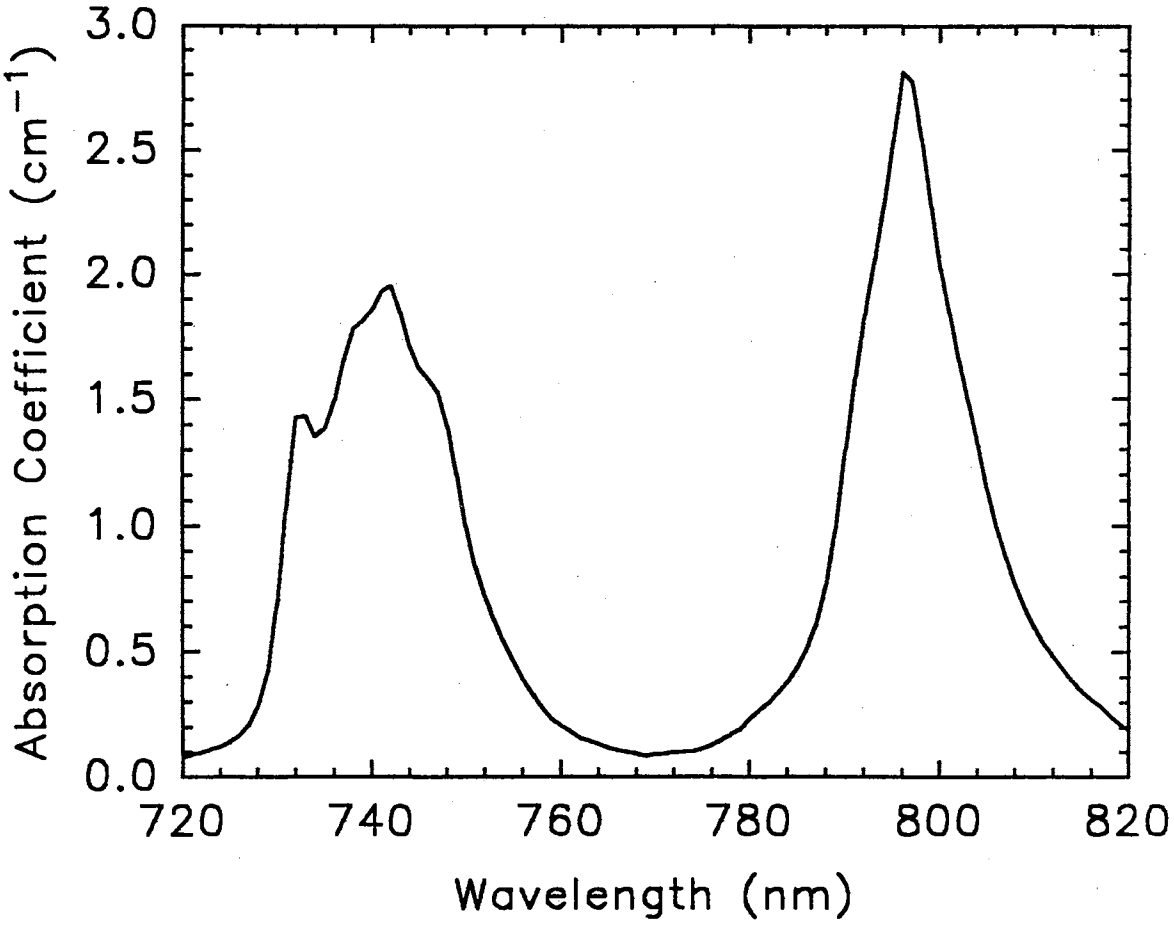

Figure 27. Absorption Spectrum of Nd:ZBAN in the Spectral Region of Alexandrite Laser Output.

recorder. For lifetime measurements an EG&G Model 4402-4420 boxcar averager signal processor combination was used.

The emission from the $^4F_{3/2}$ level of Nd^{3+} is shown in Figure 28 and can be used to determine the spectral width of the ground state manifold and the spectral location of the $^4I_{11/2}$ level shown in Figure 26. An effective linewidth of the $^4F_{3/2}$-$^4I_{11/2}$ transition, $\Delta\nu_{eff}$, can be determined by numerically integrating the emission line shape. A value for $\Delta\nu_{eff}$ of 278.8 cm^{-1} is obtained. The temperature dependence of the fluorescence lifetime is shown in Figure 29. The lifetime increases from 130 μs at room temperature to $\approx$ 400 μs at 10 K.

Table X contains the oscillator strengths determined experimentally and those calculated using the Judd-Ofelt theory along with the Judd-Ofelt parameters. The value of n for each transition was based upon that in Ref. [16]. A value of 1×10^{-6} was found for the rms deviation. For many of the weaker transitions the experimentally determined values differ significantly from those predicted from the model and in most cases the measured values for these transitions are larger than those predicted. The Judd-Ofelt parameters found here correspond well with those found in other fluoride glasses. [99–101] The Judd-Ofelt parameters can be used to calculate the oscillator strengths for excited state to excited state transitions also. Results of these calculations for transitions to the $^2P_{3/2}$ multiplet are listed in Table XI. Table XII lists the transition rates and branching ratios for emission from this multiplet. The lack of reduced matrix elements for transitions between the $^2D_{5/2}$ and $^4D_{3/2}$ multiplets and other excited states prohibits similar calculations for these multiplets.

The stimulated emission cross section can be determined from spectroscopically determined parameters using

$$\sigma_e = \frac{\lambda_p^2}{8\pi n^2 c} g(\nu)\, A\left[{}^4F_{3/2};{}^4I_{11/2}\right] \tag{86}$$

where λ_p is the peak emission wavelength, n is the index of refraction of the material, $g(\nu)$ is the lineshape of the transition, and $A[^4F_{3/2};^4I_{11/2}]$ is the radiative transition probability for this transition. The radiative transition probability is

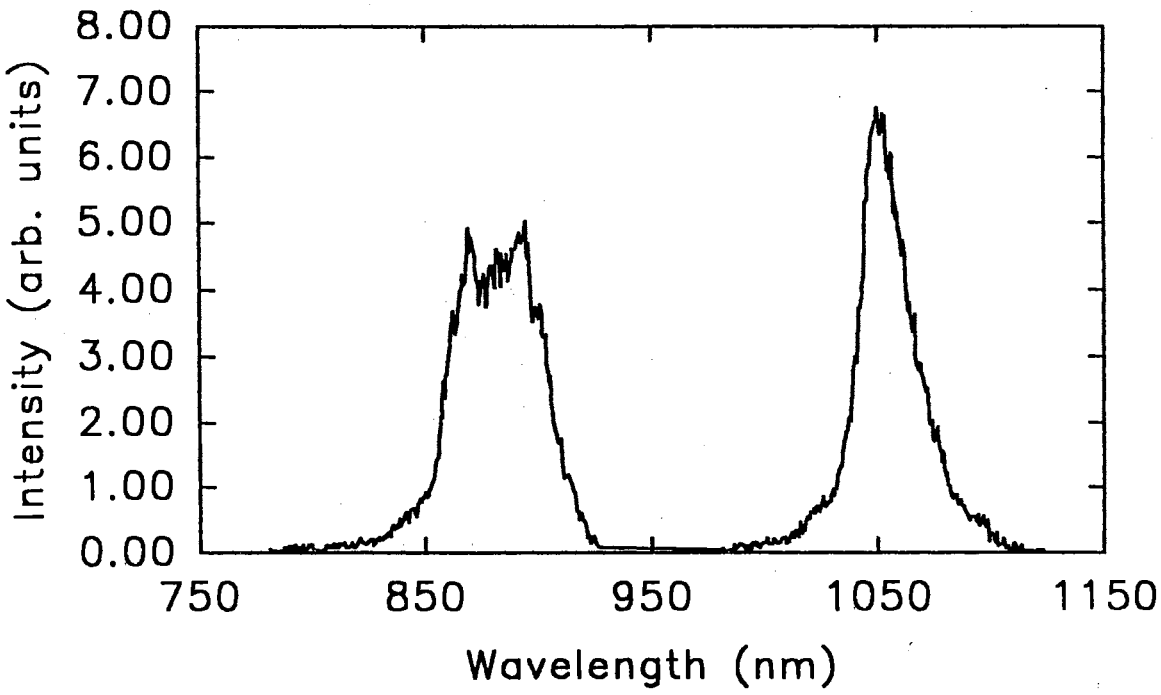

Figure 28. Room Temperature Emission Spectrum of Nd:ZBAN. Excitation at 575 nm. The effective linewidth of the $^4F_{3/2}$-$^4I_{11/2}$ transition is 278.8 cm^{-1}.

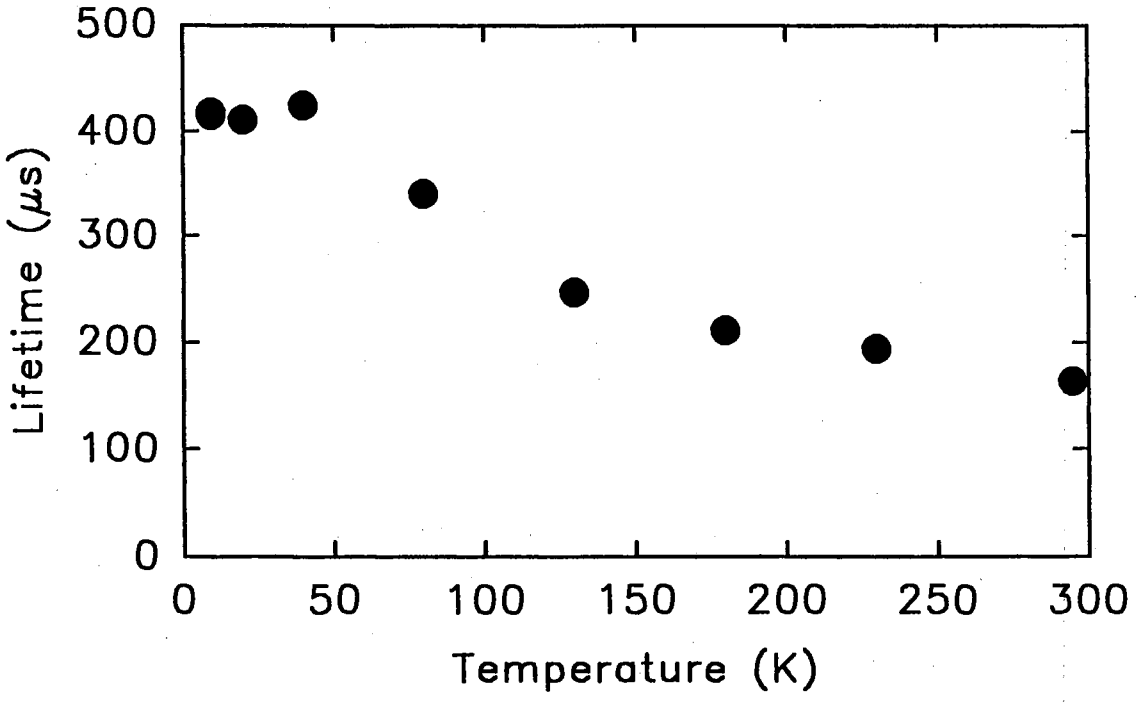

Figure 29. Temperature Dependence of the Metastable State Lifetime of Nd:ZBAN.

TABLE X

OSCILLATOR STRENGTHS FOR TRANSITIONS
FROM THE GROUND STATE
FOR Nd:ZBAN

Band	Wavelength (nm)	Oscillator Strength ($\times 10^{-8}$) Measured	Calculated	Residuals ($\times 10^{-8}$)
1	868	227.1	195.3	31.7
2	796	752.9	719.1	33.8
3	708	753.0	823.7	-70.7
4	677	102.2	58.6	43.5
5	624	35.4	16.4	19.0
6	576	1389.0	1401.0	-12.0
7	521	659.7	510.3	149.4
8	474	203.6	76.1	127.4
9	427	59.2	53.9	5.3
10	380	11.2	2.5	8.6
11	353	935.5	990.4	54.9
12	328	241.1	52.5	188.6

$\Omega_2 = 3.09 \times 10^{-20}$

$\Omega_4 = 3.65 \times 10^{-20}$

$\Omega_6 = 5.74 \times 10^{-20}$

Radiative Lifetime of the $^4F_{3/2}$-$^4I_{11/2}$ Transition

Measured	Calculated
420 μs	360 μs

TABLE XI

TRANSITION PROBABILITIES AND BRANCHING RATIOS FROM THE $^2P_{3/2}$ MULTIPLET FOR Nd:ZBAN

Terminal	λ (nm)	A (s^-1)	β (%)
$^4I_{9/2}$	380	68.8	2.73
$^4I_{11/2}$	411	370.3	14.71
$^4I_{13/2}$	445	508.5	20.20
$^4I_{15/2}$	491	81.3	3.23
$^4F_{3/2}$	675	13.6	0.54
$^4F_{5/2},^2H_{9/2}$	727	770.1	30.59
$^4F_{7/2},^4S_{3/2}$	822	22.5	0.89
$^4F_{9/2}$	866	457.4	18.17
$^2H_{11/2}$	972	88.3	3.51
$^4G_{5/2},^2G_{7/2}$	1117	7.0	0.28
$^4G_{7/2},^4G_{9/2},^2K_{13/2}$	1404	123.7	4.91
$^2D_{3/2},^4G_{11/2},^2K_{15/2}$	1916	5.8	0.23
$^2P_{1/2},^2D_{5/2}$	3452	0.5	0.01

Total Transition Probablity Rate: 2517.8 s^{-1}

TABLE XII

OSCILLATOR STRENGTHS FOR TRANSITIONS TO THE $^2P_{3/2}$ MULTIPLET FOR Nd:ZBAN

Initial Multiplet	λ (nm)	f ($\times 10^{-8}$)
$^4F_{3/2}$	676	4.01
$^4F_{5/2}$	727	6.32
$^2H_{9/2}$	727	101
$^4F_{7/2}$	820	0.78
$^4S_{3/2}$	820	8.26

difficult to determine directly but the probability rate for an electric dipole transition from the $| (S, L)J >$ manifold to the $| (S', L')J' >$ manifold can be obtained from the results of the Judd-Ofelt analysis. From Equation (13) a value for the radiative transition probability can be determined. For $\lambda_p = 1048$ nm the important rate is $A[^4F_{3/2};^4 I_{11/2}]$ and has a value of 1380 s^{-1}. Using Equation (86) yields a stimulated emission cross section of 3.2×10^{-20} cm^2 at this wavelength.

The fluorescence lifetime at room temperature is $\approx$130 μs which is much shorter than that predicted by the Judd-Ofelt analysis using Equation (15). Concentration quenching in Nd doped heavy metal fluoride glasses, previously reported [101–103], can account for this difference. The lifetime measured here at room temperature corresponds well with that determined in others glasses with similar concentrations of Nd^{3+}. The process responsible for this quenching is most likely a cross relaxation process in which a metastable state ion relaxes to the $^4I_{15/2}$ multiplet exciting a nearby ion from the ground sate to the $^4I_{15/2}$ multiplet. The longer lifetime found at low temperatures, nearly that predicted by the Judd-Ofelt theory and that found in low concentration glasses where cross relaxation is less important, indicates that the cross relaxation process is less important at low temperatures.

The emission cross section reported here for a Nd:ZBAN glass is slightly greater than that reported in ED-2, a standard oxide glass host, and much less than that in either crystal.(Table XIII) It is typical of that previously reported in a number of fluorozirconate glasses. [99,101,100,104] The radiative lifetime of the metastable state, determined from the Judd-Ofelt analysis, is nearly that reported for ED-2 and is close to that reported for other fluoride glasses.

Results and Analysis: Laser Properties

The emission of an alexandrite laser was used to side and end pump the sample in an optical cavity. The 30 cm long cavity consisted of a high reflector with a 50 cm radius of curvature and flat output couplers with varying transmittances. When end pumping a high reflector coated for high transmission over the pumping

TABLE XIII

COMPARISON OF Nd^{3+} EMISSION CROSS SECTIONS AND RADIATIVE LIFETIMES IN DIFFERENT HOSTS

	ED-2[a]	YAG[b]	YLF[c]	ZBAN
Emission Cross Section ($\times 10^{-20} cm^2$)	2.7	30.0	18	3.20
Raditive Lifetime μs	359	250	570	420
Peak Wavelength (nm)	1062	1064	1047	1048
Effective Linewidth (cm^{-1})	305	-	-	278

a From Ref. [105]
b From Ref. [5]
c From Ref. [106]

range was used. Laser output was monitored while the alexandrite pump laser was tuned over the range 735-760 nm. No lasing of the sample was detected for pump wavelengths outside this spectral range. The transverse pump geometry shown in Figure 30 was used to investigate the time resolved and emission properties of the Nd:ZBAN sample under alexandrite pumping. Time-resolved measurements were made of the output of the alexandrite laser and the output of the Nd:ZBAN glass laser using photodiodes and a Tektronix Model 2440 Digital Oscilloscope. A 2.0 neutral density filter was used in order to avoid saturation of the detector by the alexandrite pump pulse. The emission from the Nd:ZBAN sample was monitored while the material was lasing at 1.048 μm using a 0.25 m spectrometer and a C31034 photomultiplier tube which is sensitive in the visible spectral range. The signal was analyzed with a PAR model 164 boxcar averager and recorded on a strip chart recorder. Appropriate filters were used to eliminate scattered light from the alexandrite laser.

Measurements of the threshold energies and slope efficiencies with various output couplers were made using the experimental set-up shown in Figure 31. The pump beam was focused within the lowest order cavity mode using a convex lens. Simultaneous measurements of the average pulse energies of the alexandrite laser incident upon the sample and of the laser emission of the Nd^{3+} ions in the ZBAN glass were made using a dual probe energy meter.

Figure 32(a) shows the results of the the time-resolved measurements of the 1.048 μm laser emission and the alexandrite laser emission averaged signal over 256 pulses. The upper trace is the alexandrite pump pulse and the lower trace is the corresponding laser output of the Nd:ZBAN glass. Figure 32(b) shows the behavior of both the pump laser and the laser output from the sample for a single pump pulse. The short delay of the output from the sample with respect to the pump pulse is the time needed to establish the population inversion. After the short delay the traces show the relaxation oscillation and spiking characteristic of many solid state laser systems.

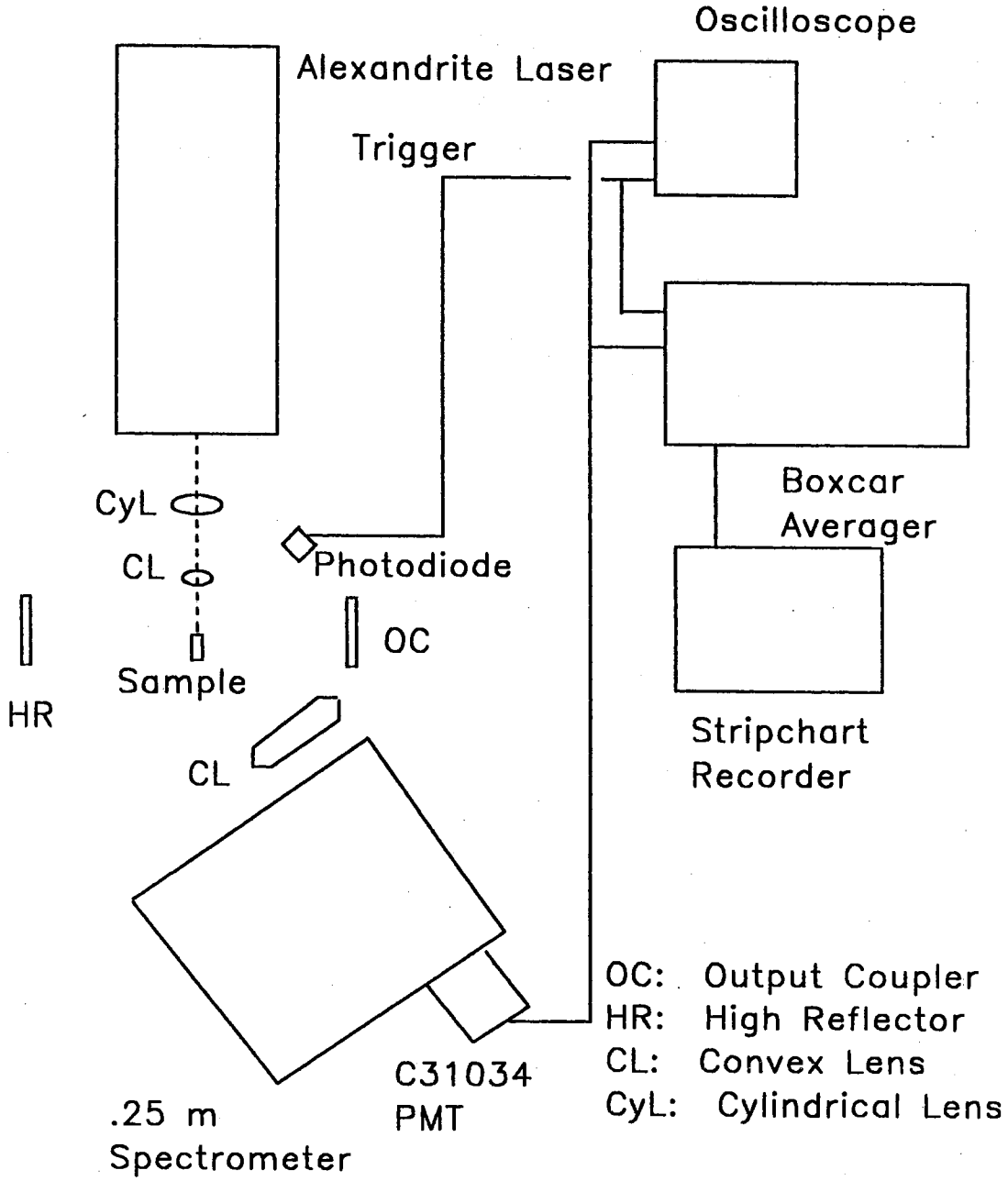

Figure 30. Experimental Set-Up for Transverse Laser Pumped Laser Experiments.

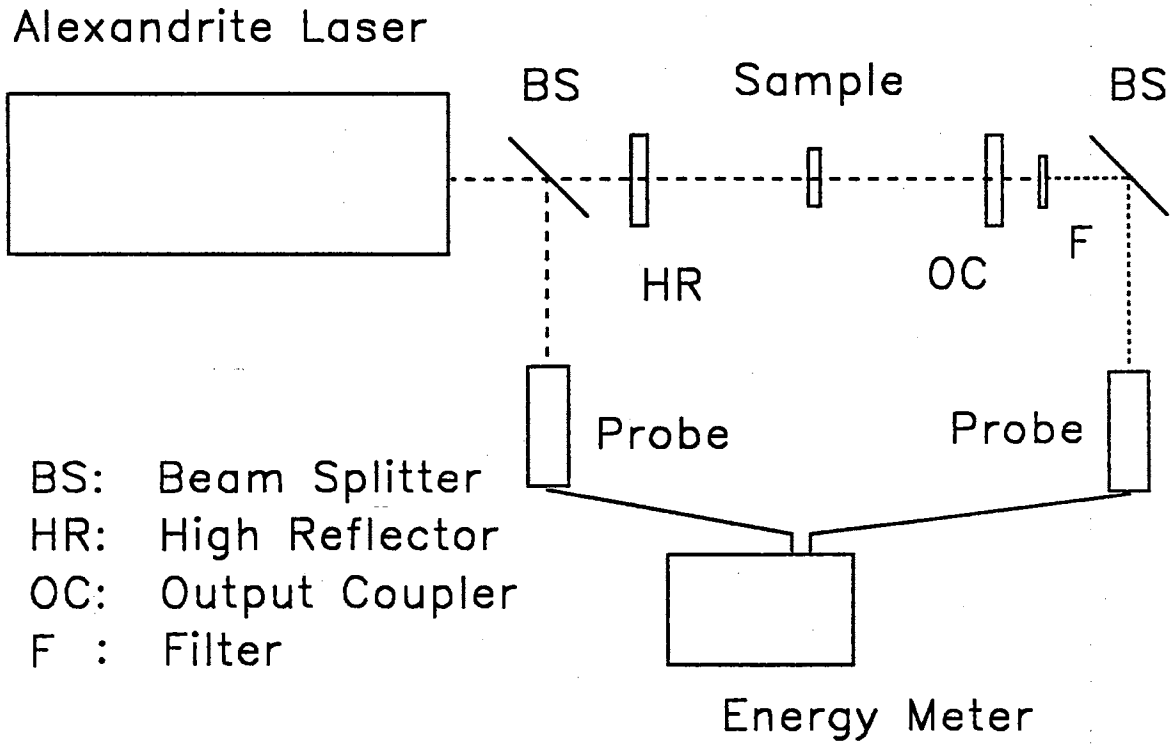

Figure 31. Experimental Set-Up for Longitudinal Laser Pumped Laser Experiments.

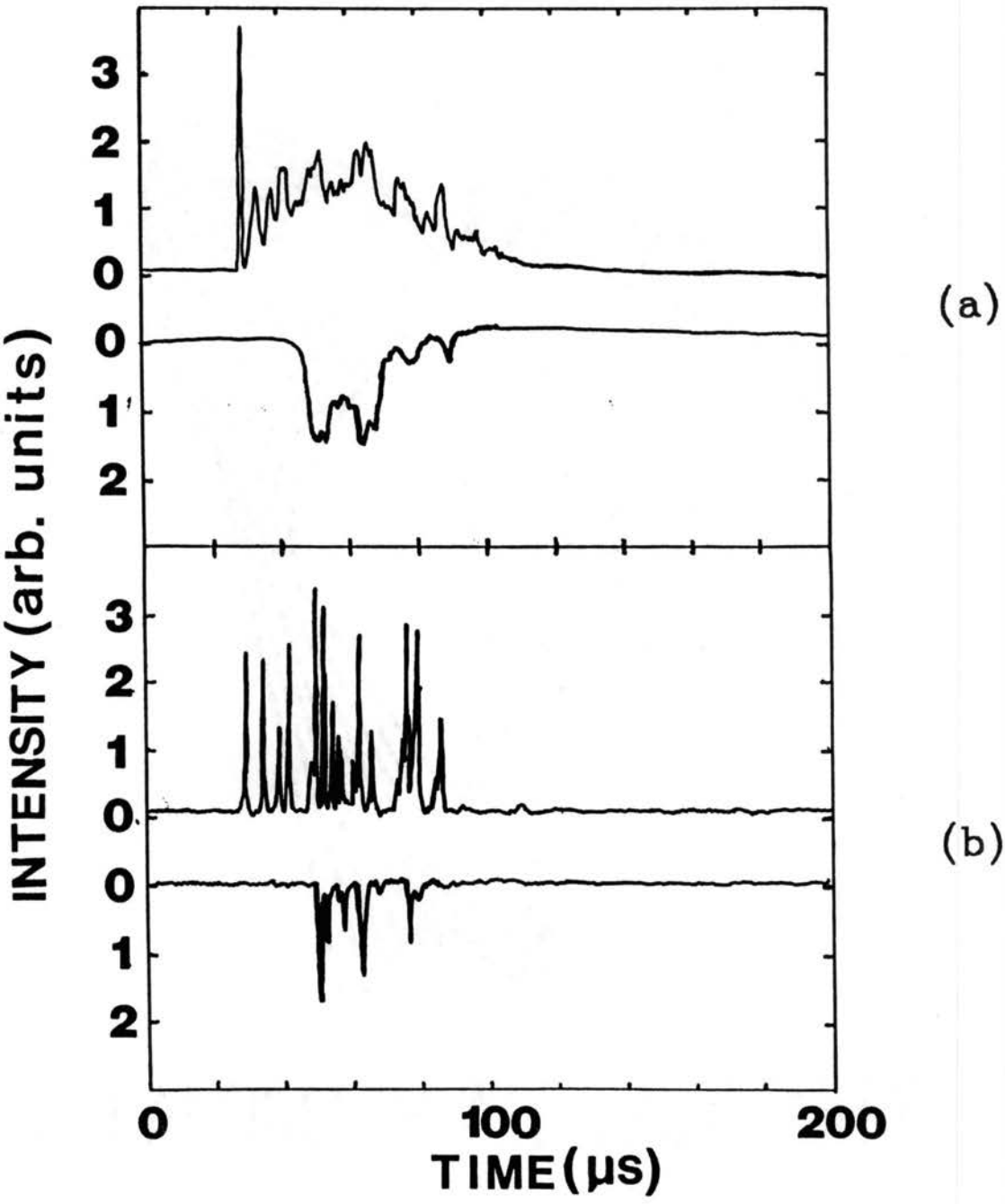

Figure 32. Temporal Output of Alexandrite Laser and Nd:ZBAN Laser (a) Output Intensity of Pump (Upper Trace) and Nd:ZBAN (Lower Trace) Averaged over 256 Pump Pulses. (b) Single Shot Time Resolved Output of the Pump Pulse (Upper Trace) and Nd:ZBAN Lasing Pulse (Lower Trace).

Figure 33 shows examples of the results obtained for measurements of the laser energy output as a function of pump energy absorbed. The deviation from a straight line relationship at high levels of power absorbed is due to several effects including saturation and thermal lensing.

The lasing thresholds and slope efficiencies can be obtained from the data above. Table XIV summarizes the results for the various pump wavelengths and output couplers. From these results, values for the passive losses in the system, the emission cross section and the relative effects of excited state absorption of pump photons on laser efficiency are determined.

The emission cross section is related to the threshold energy and mirror reflectivities by the expression [107,108]

$$-\ln(R) = M_e E_T - L \tag{87}$$

where E_T is the absorbed energy at threshold, L is the passive loss per pass through the cavity at the laser wavelength, R is the product of the effective reflectivities of the cavity mirrors, and M_e is the slope of the E_T *vs.*$\ln 1/R$ plot. R is given by [107,109]

$$R = R_{hr}\left(\frac{R_f^{1/2} + R_{oc}^{1/2}}{1 + (R_f R_{oc})^{1/2}}\right) \tag{88}$$

where R_f is the Fresnel reflection coefficient of the sample surface, R_{oc} is the reflectivity of the output coupler and R_{hr} is the reflectivity of the high reflector. The slope M_e can be written as [108]

$$M_e = \frac{8 f_B \sigma_{eff} \eta_p}{h\nu_p \pi d^2} \tag{89}$$

where η_p is the pump efficiency, f_B is the fraction of the population in the lower Stark component of the metastable state, $\pi d^2/4$ is the area of the pump beam, $h\nu_p$ is the energy of a pump photon, and σ_{eff} is the effective emission cross section. The effective emission cross section is defined as $\sigma_e - \sigma_{EA}$ where σ_e is the emission cross section and σ_{EA} is the excited state absorption cross section for photons at

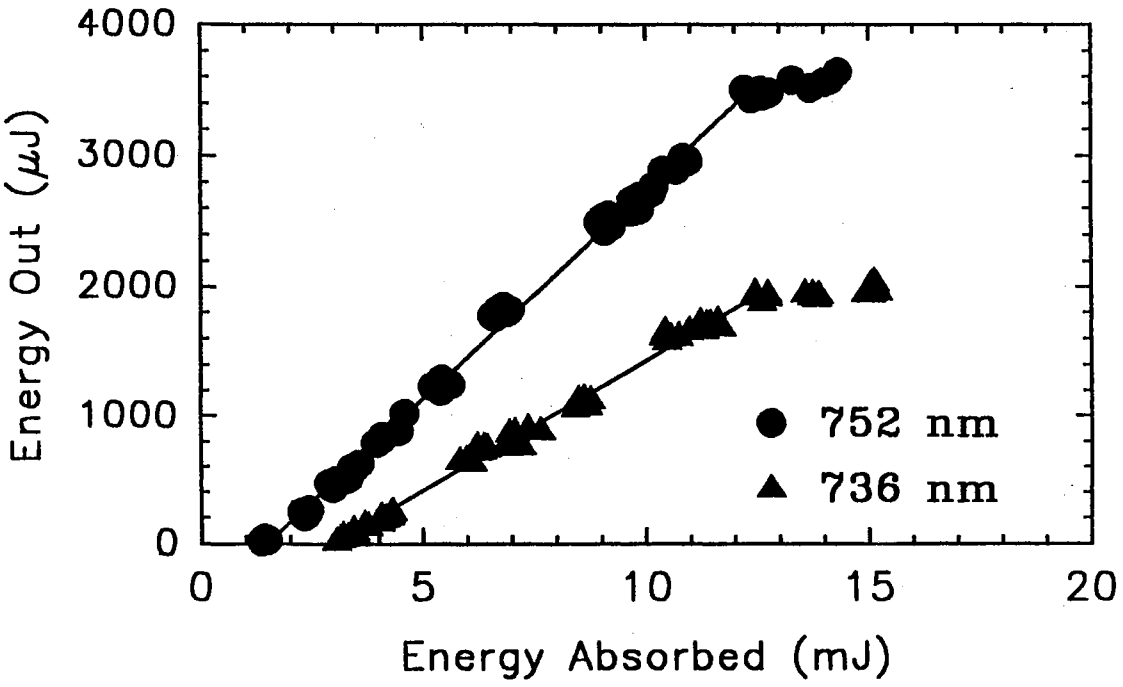

Figure 33. Nd:ZBAN Energy Out vs. Alexandrite Energy Absorbed. Data Shown for Pump Wavelengths of 752 nm (circles) and 736 nm (triangles). The Lines are a Best Fit to the Data.

TABLE XIV

SUMMARY OF THRESHOLD ENERGY AND SLOPE EFFICIENCY MEASUREMENTS

Run	Pump Wavelength (nm)	Output Coupler	R	ET (mJ)	η_s %
1	752	2	0.93	1.08	36.4
2	752	3	0.85	2.73	20.8
3	752	1	0.93	1.49	32.2
4	752	2	0.93	1.74	31.8
5	736	1	0.93	2.95	20.2
6	736	2	0.93	2.28	33.1
7	736	3	0.85	4.44	16.0

the laser wavelength. Output couplers 1 and 2 have the same value of R_{oc} to within experimental error. Figure 34 shows a plot of $-\ln R$ *vs.* threshold energy absorbed. The lines drawn in Figure 34 pass through the average threshold energy of runs 1, 3, and 4 for the 752 nm case and runs 5 and 6 for the 736 nm case. From these plots values for M_e of 72/J and 51/J and values for L of 0.034 and 0.063 were obtained for 752 nm and 736 nm pump wavelengths respectively.

Rewriting Equation (89) yields

$$\eta_p \sigma_{eff} = \frac{h\nu_p \pi d^2 M_e}{8 f_B}. \tag{90}$$

The fractional Boltzmann population of the lower Stark component of the $^4F_{3/2}$ can be found from

$$f_B = \left[\exp\left(\frac{-\Delta E}{k_B T}\right) + 1\right]^{-1} \tag{91}$$

where ΔE is the Stark splitting of the metastable state, k_B is Boltzmann's constant, and T is the temperature in Kelvin. ΔE was approximated as 90 cm^{-1}, typical of the crystal field splitting for the $^4F_{3/2}$ multiplet. At room temperature $k_B T$ is 207 cm^{-1} giving a value for f_B of 0.61. The area of the pump beam was measured to be $\approx$0.001 cm^2. The effective emission cross section and pump efficiency for each wavelength used can be found from Equation (90)

$$\eta_p^{752} \sigma_{eff} = 1.57 \times 10^{-20} cm^2 \tag{92}$$

$$\eta_p^{736} \sigma_{eff} = 1.13 \times 10^{-20} cm^2 \tag{93}$$

where the superscripts label the pump wavelength.

It is possible to relate the measured slope efficiencies to $\eta_p \sigma_{eff}$. In the limit of low output coupling [110,111]

$$\eta_s = \frac{\lambda_p}{\lambda_l} \frac{\eta_p \sigma_{eff}}{\sigma_e} \frac{C_o}{C + L} \tag{94}$$

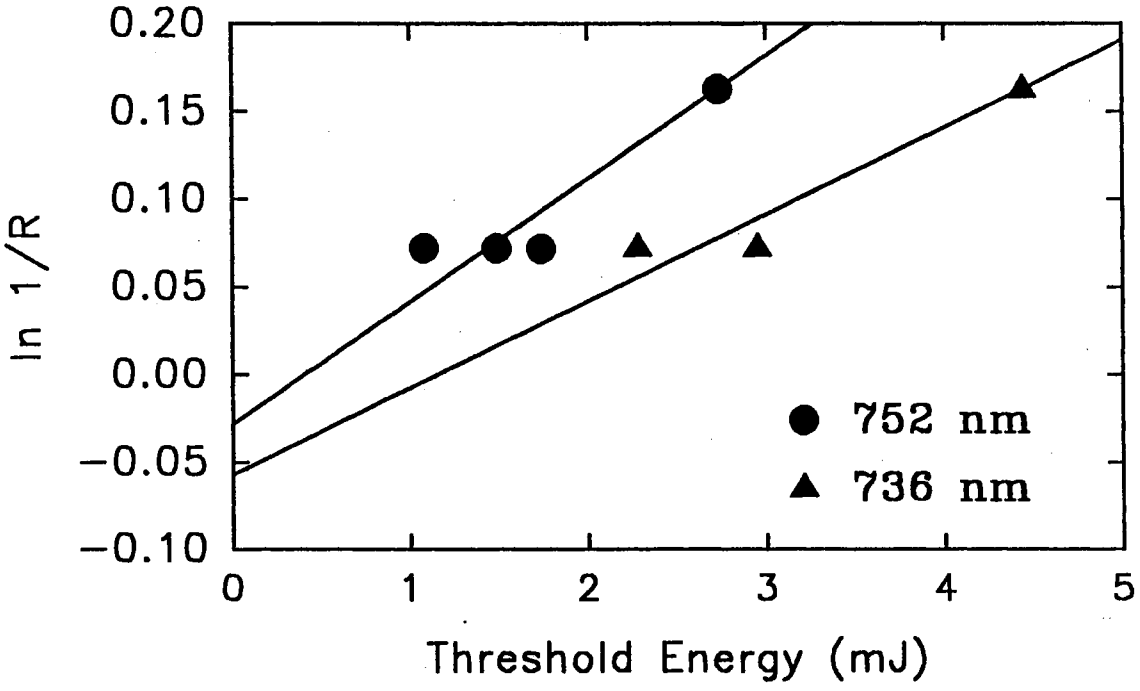

Figure 34. Plot of ln 1/R vs. Threshold Energy Absorbed. The y Intercepts are the Passive Losses in the System and the Slopes are Related to the Emission Cross Section. Data Shown for Pump Wavelengths of 752 nm (circles) and 736 nm (triangles).

where η_s is the slope efficiency, λ_p and λ_l are the pump and laser wavelengths respectively, C_o is the effective output coupling, C is the total transmission of the mirrors and the other parameters have their previous meanings. Rewriting and solving for σ_e gives

$$\sigma_e = \frac{\lambda_p}{\lambda_l}\frac{\eta_p \sigma_{eff}}{\eta_s}\frac{C_o}{C+L}. \tag{95}$$

Restricting the analysis to the lower transmission output couplers (1 and 2) and letting $C = C_o$ ($R_{hr} = 1$) values for σ_e of 2.25×10^{-20} cm^2 and 1.56×10^{-20} cm^2 are found from the parameters for 752 nm and 736 nm respectively.

One possibility that would produce different emission cross sections for different pump wavelengths is a change in pump efficiency with wavelength. Comparison of the values for $\eta_p\sigma_{eff}$ at the two different pump wavelengths indicates that the pump efficiency at 736 nm is less than that at 752 nm if the cross sections are wavelength independent. The effective emission cross section should be independent of pump wavelength giving ${\eta_p}^{736} = 0.72\ {\eta_p}^{752}$. An increase in the energy absorbed for threshold and a lower slope efficiency at the 736 nm pump wavelength lead to the calculation of a reduced pump efficiency for this wavelength using Equations (87), (89), and (94).

Alternatively, the difference between the emission cross sections calculated from the slope efficiency measurements at the two wavelengths could be an indication of the uncertainties in the calculation. In this case the pump efficiencies are similar. Since the emission cross section should be independent of pump wavelength, differences between the values for 752 nm and 736 nm would be attributed to the uncertainties in the measured slope efficiencies, threshold energies and in the extrapolation used to find the passive losses.

Figure 35(a) shows an example of the emission spectra with an excitation wavelength of 755 nm and the emission spectra in Figure 35(b) is that for a pump wavelength of 735 nm. Note the similarities to the spectra observed for Nd:YAG and Nd:GSGG in Chapter IV. The analysis in this case is made more difficult by the broadened absorption and emission peaks in the fluoride glass and the lack

of detailed knowledge of the Stark level positions. The two green peaks centered at 530 nm and 595 nm have been reported earlier in other Nd^{3+}-doped materials [77,80,82–84] and can be attributed to transitions from the $^4G_{7/2}$ and $^2G_{9/2}$ energy levels to the ground state and the $^2G_{7/2}$ and $^2G_{5/2}$ levels to the ground state, respectively. The transitions leading to the blue (365-460 nm) emission spectra observed under alexandrite laser excitation (Figure 35) cannot be definitely identified but from conservation of energy arguments transitions from the $^2P_{3/2}$, $^4D_{3/2}$, and $^4D_{5/2}$ to the ^4I_J levels seem to be the most probable. The upper state could be populated via resonant excited state absorption of pump photons from the $^4F_{3/2}$, $^4F_{5/2}$, $^2H_{9/2}$ or $^4F_{7/2}$, $^4S_{3/2}$ multiplets. The oscillator strength for ESA process involving the $^2P_{3/2}$ and the $^4F_{5/2}$, $^2H_{9/2}$ multiplets is much larger than that for transitions originating on either the metastable level or the pump level, similar to the results for Nd:YAG and Nd:GSGG. (Table XII) However, other transitions to $^4D_{3/2}$ and $^4D_{5/2}$ multiplets from the pump level and to the $^2P_{3/2}$ from the metastable state are nearly resonant for the 735 nm pump wavelength. Both of these transitions are resonant to within 500 cm^{-1}, the energy of a high energy phonon in fluoride glasses [102,103], and will assist in populating the upper states. For the 755 nm pump wavelength the transition from the pump level to the $^2P_{3/2}$ multiplet is nearly resonant but the other transitions are not.

A comparison of Figures 35a and 35b leads to the following conclusions. At shorter pump wavelengths the blue emission is the most intense. As the excitation wavelength is shifted to lower energies the blue emission decreases and the green emission becomes more intense. This decrease in the blue emission can be attributed to the loss of resonance between the pump photon energy and the energy difference between the $^4F_{5/2}$,$^2H_{9/2}$ and $^2P_{3/2}$ multiplets and between the $^4D_{3/2}$ and $^4D_{5/2}$ multiplets and the pump level. The increase in intensity of the green emission may be due to nonresonant excited state absorption of pump photons with the energy mismatch compensated for by phonon emission and to increased output of the alexandrite laser at 755 nm as compared to 735 nm. The important observation, however, is the pump wavelength dependence of the emission. The

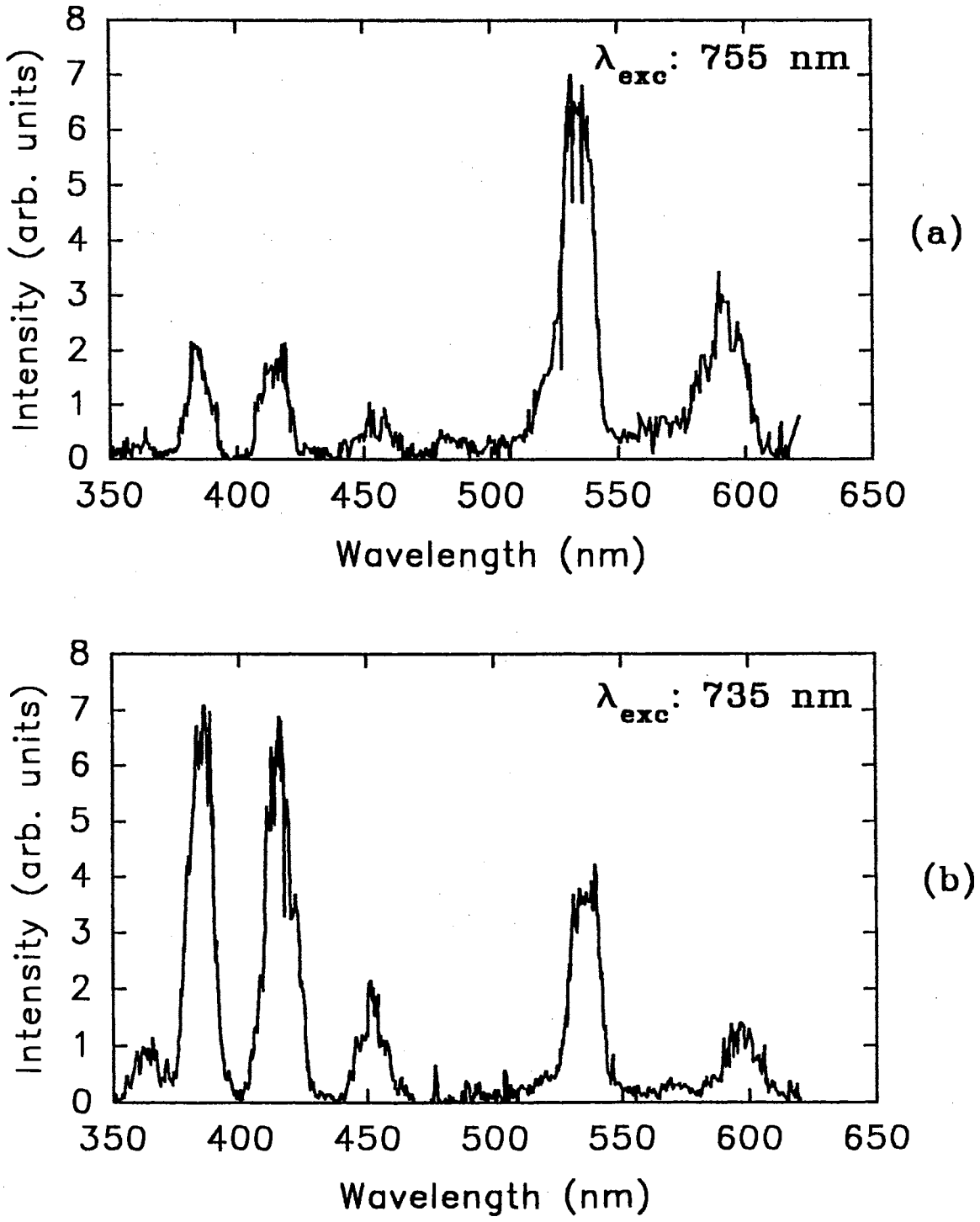

Figure 35. Emission Spectra of Nd:ZBAN in the Blue-Green Spectral Region with Alexandrite Excitation. Pump Wavelength of (a) 755 nm and (b) 735 nm.

relative intensities of the blue and green emission change with pump wavelength. Therefore the process leading to the emission is pump wavelength dependent and, of the processes that could lead to blue emission, only ESA of pump photons is pump wavelength dependent.

Excited State Absorption Model

Excited state absorption of pump photons (ESA) may be a loss mechanism in Nd^{3+} doped laser hosts.[77,84] Here a model which describes the effects of ESA on both the metastable state population and the total energy circulating in the cavity at the output wavelength is presented. The model used is a modified version of the standard Nd^{3+} four level model and is shown in Figure 36. Two additional levels are added, an intermediate level between the pump level and the metastable state and a second level at a higher energy than the pump level. The second level is located such that it is in resonance with the added intermediate level at the pump energy. Since the transition between levels 4 and 6 is in resonance with the pump laser it is possible for excited state absorption of pump photons to occur.

The rate equations describing this model are written as follows:

$$\dot{n}_1 = -R_{15} + R_{51} + A_{61}n_6 + A_{31}n_3 + W_{21}n_2 - W_{12}n_1 \tag{96}$$

$$\dot{n}_2 = +R_{32} - R_{23} + A_{32}n_3 - W_{21}n_2 + W_{12}n_1 + W_{eff}n_3 \tag{97}$$

$$\dot{n}_3 = -R_{32} + R_{23} - \tau_3^{-1}n_3 + A_{63}n_6 + W_{43}n_4 - W_{34}n_3 - W_{eff}n_3 \tag{98}$$

$$\dot{n}_4 = -R_{46} + R_{64} + A_{64}n_6 - W_{45}n_4 + W_{54}n_5 - W_{43}n_4 + W_{34}n_3 \tag{99}$$

$$\dot{n}_5 = +R_{15} - R_{51} + A_{65}n_6 + W_{45}n_4 - W_{54}n_5 \tag{100}$$

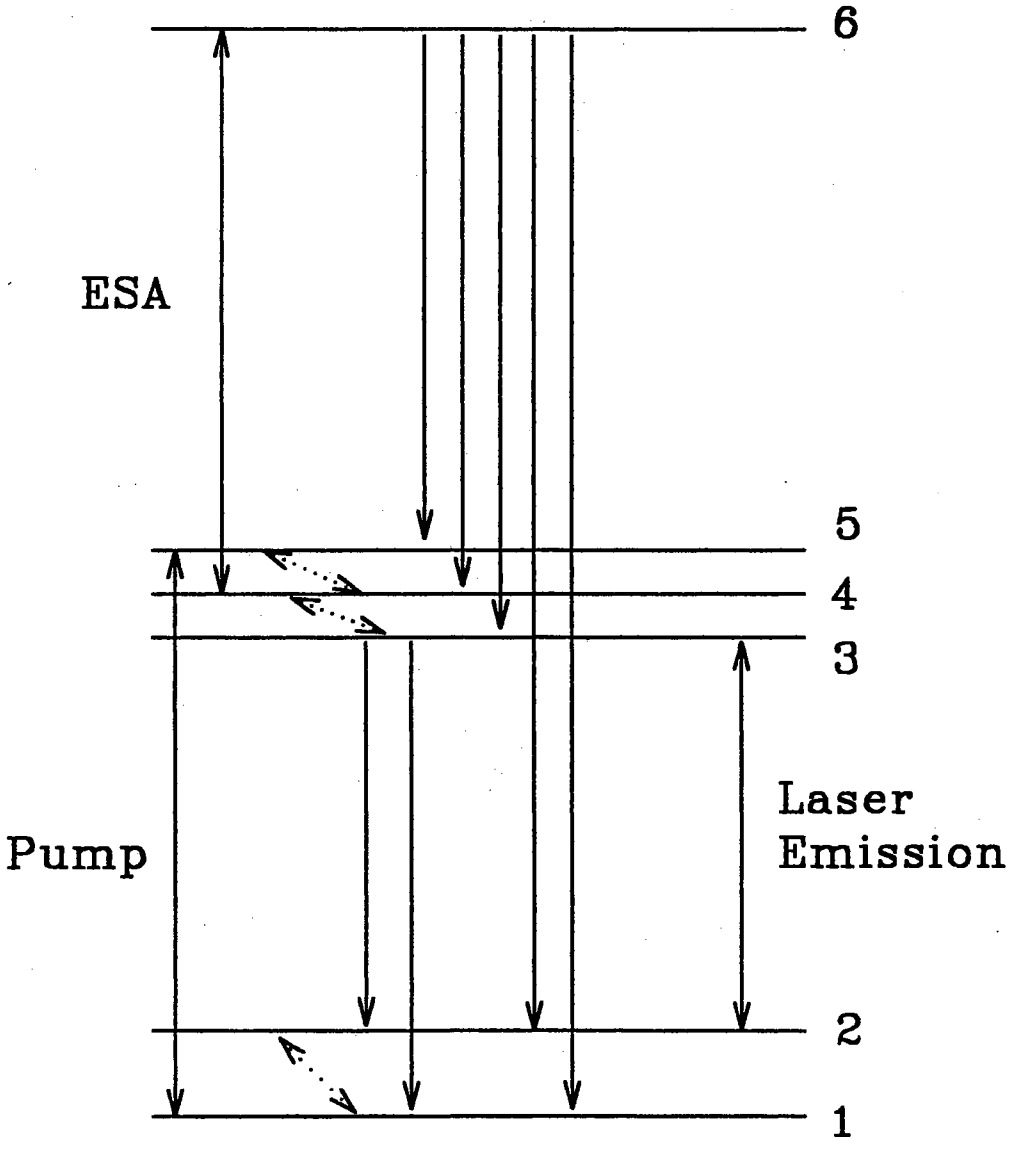

Figure 36. Model of Nd:ZBAN Laser System.

$$\dot{n}_6 = +R_{46} - R_{64} + \tau_6^{-1} n_6 \tag{101}$$

$$\dot{n}_p = +R_{32} - R_{23} - \tau_c^{-1} n_p + \omega_{el} n_3 \tag{102}$$

For transitions resonant with either the pump laser wavelength or the output laser wavelength both stimulated emission and absorption are included. Fluorescence is allowed from the metastable state to both the ground state, level 1, and the first excited state, level 2. Fluorescence from the upper excited state (6) can occur to each of the excited states and the ground state. Levels 2, 4, and 5 are assumed to decay only non-radiatively.

The population of each level and the photon density is determined from a numerical solution of the rate equations by a fourth order adaptive Runge-Kutta method. The parameters used are listed in Table XV and are representative of those for Nd^{3+} in a fluoride glass host. Non-radiative ion-ion cross relaxation, which reduces the lifetime of the metastable state, is modeled simply as an additional relaxation process (W_{eff}) populating the terminal laser level. The emission cross section for the pump transition is found from the measured absorption cross section and Equation (61). This equation and the spectroscopically determined emission cross section for the laser wavelength are used to find the absorption cross section at the output laser wavelength. Since the exact positions of the Stark levels are not known for the fluoride glass, Z_l and Z_u are approximated by their values in other Nd^{3+} materials.[5,86,87,112] Values for Z_l for the lower level of the pump transition vary from $\approx$2.1 to $\approx$2.7 and values for Z_u for the upper level of the pump transition vary from $\approx$3.0 to $\approx$3.8. A value for Z_l/Z_u for the pump transition used here is 0.7. For the laser transition, values for Z_l vary from $\approx$3.0 to $\approx$4.0 and values for Z_u vary from $\approx$1.6 to $\approx$1.8. This gives a value for Z_l/Z_u of 2 for the laser transition. The zero line energy, E_{zl}, is approximated as the energy of the transition so that $E_{zl} - h\nu$ is zero for both cases. The non-radiative rates listed in the table labeled by A are representative non-radiative decay rates in fluoride glasses found from the energy gap law, Equation (22), using values for

the parameters C and α found in Ref. [113]. The second set of rates, labeled B, are representative of rates much faster than those predicted by the energy gap law as suggested by recent measurements of small energy gap multiphonon rates. [24,27,91] The relaxation rate for the lower laser level is approximated based on recent measurements in a variety of materials. [24,26,27,91] The alexandrite pump laser pulse is modeled with a series of 300 ns pulses of constant flux separated by $\approx$4 μs in a 40 μs envelope. The flux used used corresponds to an incident energy of 17 mJ per 40 μs pulse train focused within the lowest order mode of the cavity.

The results of the numerical solution for the metastable state population and the photon density over the first 400 ns using the smaller multiphonon rates are shown in Figure 37. The solid line and long-dashed line represent the metastable state population for the cases $\sigma_{46} = 0$ (no excited state absorption) and $\sigma_{46} = 5\times10^{-18}$ cm^2, respectively (for simplicity, the emission cross section for this transition is assumed to be equal to the absorption cross section). The photon density with no ESA is shown by a short-dashed line while that with ESA is shown by a dotted line.

These results qualitatively display some of the effects of excited state absorption of pump photons on laser dynamics. When ESA of pump photons is possible the population of the metastable state grows significantly more slowly than when there is no ESA possible. In Figure 37 the population of level 3 when ESA is present rises more slowly than that when there is no ESA. The time at which lasing occurs is also shifted due to excited state absorption. The photon density in the cavity peaks at 298 ns when there is no ESA but doesn't peak until 342 ns when ESA is allowed. There are no significant differences between the ESA and no ESA cases when the larger multiphonon relaxation rates are used. For excited state absorption to be important, the metastable state population and the photon density must remain significantly below the values achieved when no ESA is possible.

It is possible to determine the loss in available output energy from the photon density. The stored energy in the cavity is related to the photon density by

TABLE XV

PARAMETERS USED IN Nd:ZBAN
RATE EQUATION MODELING

$A_{61} = 1029s^{-1}$ $A_{62} = 0s^{-1}$
$A_{63} = 14s^{-1}$ $A_{64} = 770s^{-1}$
$A_{65} = 705s^{-1}$ $A_{31} = 978s^{-1}$
$A_{32} = 1828s^{-1}$

$\sigma_{15} = 1.37 \times 10^{-20}cm^2$ $\sigma_{32} = 5.00 \times 10^{-20}cm^2$
$\sigma_{46} = 5.00 \times 10^{-18}cm^2$

A=0.7 B=0.5 C=1.0

$\tau_c^{-1} = 6.00 \times 10^7 s^{-1}$
$\Phi_p = 4.0 \times 10^{26} photons/cm^2 s$

$W_{21} = 1 \times 10^8 s^{-1}$ $W_{12} = 6.9 \times 10^4 s^{-1}$
$W_{eff} = 5000s^{-1}$

A[a]	B
$W_{54} = 2.9 \times 10^7 s^{-1}$	$W_{54} = 2.9 \times 10^9 s^{-1}$
$W_{45} = 9.7 \times 10^5 s^{-1}$	$W_{45} = 9.7 \times 10^7 s^{-1}$
$W_{43} = 1.9 \times 10^7 s^{-1}$	$W_{43} = 1.9 \times 10^9 s^{-1}$
$W_{34} = 4.1 \times 10^5 s^{-1}$	$W_{34} = 4.1 \times 10^7 s^{-1}$

a From Ref. [113]

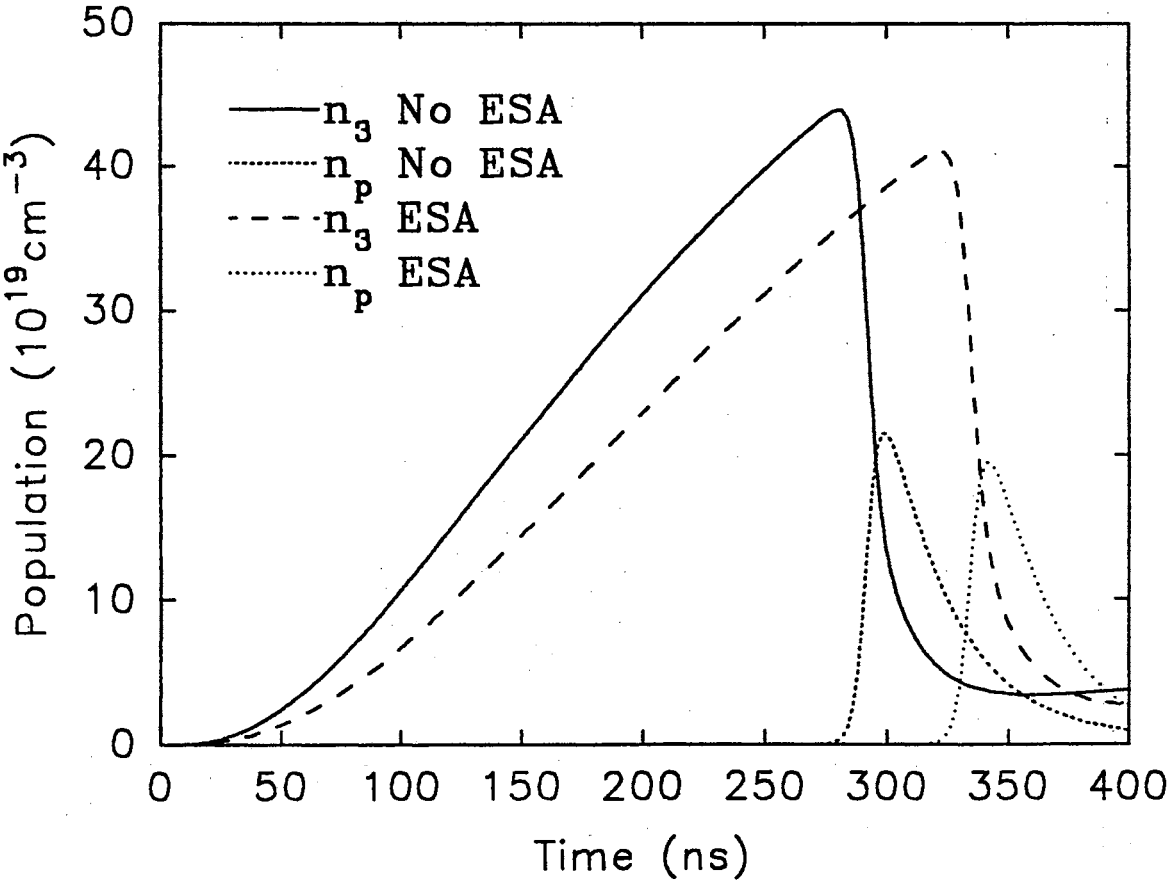

Figure 37. Plot of Metastable State Population and Photon Densities Predicted by the Rate Equation Model. The Solid Line and Long- Dashed Lines are the Metastable State Population Densities with and without ESA, Respectively, and the Short-Dashed Line and Dotted Lines are the Photon Densities with and without ESA, Respectively.

$$Energy \propto A \int n_p(t)dt$$

where A includes the energy per photon, the speed of light , and the area of the cavity mode. The value of $\int n_p(t)dt$ is determined by numerically integrating the photon density. For the case with the smaller non-radiative multiphonon rates, excited state absorption causes this value to decrease from 9.64×10^{13} to 8.32×10^{13} photons s/cm^3 , a reduction of $\approx$ 14%, reducing the available energy by a similar amount. Note that only one of the possible ESA processes is considered here and the additional processes mentioned earlier will further reduce the energy at the output wavelength.

The importance of ESA of pump photons is especially dependent on two sets of system parameters. One of the these sets are the branching ratios for emission from the upper state involved in the ESA transition. If the branching ratio for transitions from this state to levels below the metastable state is larger than that to levels above the metastable state the effects of ESA will be more important. Those ions that participate in ESA are lost to the metastable state since they radiatively decay to lower levels. If the reverse is true and transitions to states above the metastable state are more likely then the effects of ESA will be reduced since ions excited to upper states will relax back to the metastable state. In Nd:ZBAN the $^2P_{3/2}$ state is one of the upper state involved in ESA. The Judd-Ofelt analysis performed (Table XII) predicts that nearly 60% of the emission from the $^2P_{3/2}$ state occurs to levels above the metastable state. The effects of ESA in this system will be different in materials where these branching ratios are significantly different. If more of the emission from the upper level occurs to levels below the metastable state then ESA may be more important while if more of the emission occurs to levels above the metastable state ESA will be less important. Also, if non-radiative multiphonon decay depopulates the upper state, the effects of ESA will be reduced.

The second set of parameters which determines the importance of ESA is the combination of the non-radiative decay rate from the level from which ESA is occurring and the product of the flux and the absorption cross section for the process. This can easily be seen by examining Equation (99), governing the population of the intermediate level from which ESA is occurring and Equation (101) governing the decay of the upper excited state. Although values for the non-radiative decay rates W_{54} and W_{43} are difficult to determine, the energy gap law can be used to give approximate values. Using the energy gap law and one set of parameters for C and α a non-radiative rate of 1.92×10^7 s^{-1} is obtained for the $^4F_{5/2}$-$^4F_{3/2}$ transition. The second set of parameters yields a much larger rate. For ESA to be an important loss mechanism the product of Φ_p and σ_{46} must be of at least the same order of magnitude as W_{43}, so the effects are expected to be smaller when the non-radiative multiphonon rates are larger. The lack of significant changes in the metastable state population density and photon density when the larger relaxation rates are used is evidence of this. Additionally, since more transitions are resonant or nearly resonant for a 736 nm pump wavelength compared to 752 nm pump wavelength the effective cross section for the former transition is expected to be higher than that for the latter. Thus the effects of ESA are larger for a 736 nm pump wavelength than that for 752 nm. This seems to be indicated by the analysis of the pumping efficiencies.

For reasonable values of the absorption cross section for the ESA transition, the requirement that $\Phi_p\sigma_{46} \approx W_{43}$ requires the high fluences encountered only when using a high peak power pulsed laser as a pump source. As shown in Figure 32 the output of the alexandrite laser used here is not a smooth pulse. The spiking in the pump laser due to relaxation oscillations provides the high fluences necessary for ESA to be important. The non-radiative decay rates in fluoride glasses are known to be lower than those in many other laser materials.[101–104] Thus the requirement above is more easily met in fluoride glasses than in other materials, such as Nd:YAG. Previously reported wavelength dependent slope efficiency changes in Nd:YAG [77] can be attributed to difficulties in determing the energy

absorbed in the cavity mode of the system. Even in the fluoride glasses, however, if the actual non-radiative rates are closer to the larger values used here or are much faster than those predicted by the energy gap law, as recently found in other Nd^{3+} doped materials for small energy gaps, [24,27,91] then the effects of ESA will be reduced. In this case, additional mechanisms such as sequential two photon absorption and non-resonant transitions originating on the metastable state will be much more important in any explanation of a decrease in slope efficiency with pump wavelength.

Summary and Conclusions

The two different methods used to calculate to stimulated emission cross section yield different results, the spectroscopic method producing a result which is larger than that found by using the measured laser properties. A very critical factor in the latter method is the determination of f_B. It is assumed here that the upper level for the lasing transition is the lower Stark component of the $^4F_{3/2}$ manifold. If the laser transition actually originates on the upper Stark component, as found in many Nd^{3+} doped systems, then the value of f_B would be a factor of two smaller, effectively doubling the values calculated using the method based on laser efficiency measurements and bringing them closer to that determined spectroscopically. The difference between the emission cross sections calculated from the slope efficiency measurements at the two wavelengths arises from two possibilities: either uncertainties in the measured slope efficiencies, threshold energies and the extrapolation used to find the passive losses or changes in pump efficiency with wavelength.

Excited state absorption of pump photons is identified as a possible mechanism for reducing the pumping efficiency at certain wavelengths. The wavelength dependence of the blue emission under alexandrite excitation provides evidence for an ESA process. Although the exact transitions involved and the actual dynamics of the system are not definitively identified, evidence indicates that the $^2P_{3/2}$ multiplet is one of the multiplets involved in the blue emission. A model of

the ESA process quantitatively shows that this process can be an important loss mechanism under certain conditions. If high peak power pulsed lasers are used as pump sources, if the multiphonon decay rate from the intermediate level is slow and if the branching ratios for emission from the upper state involved are such that much of the emission from the upper state bypasses the metastable state then ESA is important. The results presented here indicate that excited state absorption of pump photons should be considered in the selection of host materials to insure the criteria for this effect to be important are not met.

CHAPTER VI

SUMMARY AND FUTURE WORK

Summary

Problems relevant to three different rare-earth ion based laser materials have been discussed. In the first material, Tm,Ho:YAG, the energy transfer processes leading to 2.1 μm laser emission after diode laser pumping were investigated. Two of the energy transfer processes, the Tm→Tm cross relaxation process and the Tm→Ho energy transfer process, were characterized. Enhancement of the Tm→Tm cross relaxation process by energy migration in the $^3H_4$ multiplet was observed. The rate parameter for the overall process was established. Rate parameters describing the Tm→Ho energy transfer process were also determined. These parameters were then used in a numerical solution of a rate equation model of the laser system. Since the parameters were determined spectroscopically, there were no adjustable parameters in the simulation. This model accurately predicted the previously observed delay between the pump laser pulse and emission at 2.1 μm and the relaxation oscillations. Additionally, a new loss mechanism involving excited state absorption of pump photons was identified and found to contribute significantly to the observed green emission.

Three Nd^{3+} based laser materials were also investigated. In each material, an excited state absorption mechanism leading to blue emission was identified. For the crystalline systems studied, the $^2P_{3/2}$ multiplet was identified as the upper multiplet involved in the emission from a comparison of the predicted and observed emission wavelengths. Energy conservation considerations led to the conclusion that one of the processes populating the $2P_{3/2}$ multiplet was a resonant excited

state absorption process originating on the $^4F_{5/2}$ and $^2H_{9/2}$ multiplets. A Judd-Ofelt analysis was also performed and showed that this transition had a larger oscillator strength than transitions originating on either the pump or metastable levels. Although the situation involved in the fluoride glass was found to be much more complex, the same transitions and processes were identified as contributing to the emission observed in this material. The overall effect of this excited state absorption process on laser efficiency was also considered. A rate equation model was used to identify the important parameters controlling the effects on the energy stored in the metastable state. The relative sizes of the non-radiative decay rates and the rate of excited state absorption were found to be very important. Excited state absorption was found to be more important in materials with slower non-radiative relaxation rates, such as fluoride glasses, than in materials with fast non-radiative decay, such as garnets. Evidence from laser efficiency measurements indicated a wavelength dependent pump efficiency in a Nd:ZBAN fluoride glass laser, possibly an effect of this excited state absorption process.

Future Work

Although the overall dynamics of the Tm,Ho:YAG laser system are now well understood, a few questions still remain to be investigated. The concentrations of Tm^{3+} and Ho^{3+} for optimum diode laser pumped performance remain to be determined. This will require a better understanding of the overall dependence of Tm→Ho energy transfer process on the concentration of both dopants. Additionally, the effects of the loss mechanisms need to be considered carefully since two of the loss mechanisms involve ion-ion interactions. The concentration dependencies of both ion-ion energy transfer processes must be determined and balanced against the need for fast Tm→Tm cross relaxation and energy migration. The new mechanism identified here, excited state absorption of pump photons by ions in the Ho^{3+} metastable state, may be important in systems where the excited state population density is large, as in Q-switched systems. Further work also should consider a more complex model of the system, accounting for emission at multiple

wavelengths and spatial effects. The extension of the model to different material systems would be worthwhile in the identification of potential new host materials.

Further work in Nd^{3+} laser materials includes a number of problems that must be addressed. The origin of the additional blue emission lines observed in the Nd:YAG system, not attributable to emission originating on the $^2P_{3/2}$ multiplet, need to be identified. These lines are most likely due to emission from states at higher energies than the $^2P_{3/2}$ multiplet which cannot be excited by single photon absorption from the pump, intermediate, or metastable levels. The non-radiative relaxation rates involving multiplets separated by small energy gaps need to be determined much more accurately than presently known. These relaxation rates play an important role in determining the effects of loss mechanisms that populate states above the metastable state and need to be established before further quantification of the effects of loss mechanisms. Additionally, their understanding will lead to a more complete understanding of non-radiative relaxation in rare-earth ion laser materials. For the fluoride glass material, further study of the processes leading to blue emission and the wavelength dependence of the pumping efficiency need to be considered. In this material the non-radiative relaxation rates may be slow enough for excited state absorption to be a loss mechanism. Alternatively, optimization of the excited state absorption process may prove to be useful for diode pumped upconversion laser operation in the blue spectral region.

BIBLIOGRAPHY

1. A. L. Schawlow and C. H. Townes, Phys. Rev. **112**, 1940 (1958).
2. T. H. Maiman, Nature **187**, 493 (1960).
3. P. P. Sorokin and M. J. Stevenson, IBM J. Res. Dev. **5**, 56 (1961).
4. L. F. Johnson and K. Nassau, Proc. IRE **49**, 1704 (1961).
5. A. A. Kaminskii, **Laser Crystals 2ed** (Berlin, Springer-Verlag, 1990).
6. G. H. Dieke, **Spectra and Energy Levels of Rare Earth Ions in Crystals** (Interscience, New York, 1968).
7. B. G. Wybourne, **Spectroscopic Properties of Rare Earths** (Interscience, New York, 1965).
8. L.A. Riseberg and M.J. Weber, in **Progress in Optics Vol. 14**, ed. E. Wolf (North Holland, New York, 1976) p89.
9. B.R. Judd, Phys. Rev. **127**, 750 (1962).
10. G.S. Ofelt, J. Chem. Phys. **37**, 511 (1962).
11. H. W. Moos, J. Lumin. **1**, 106 (1970).
12. M. J. Weber, Phys. Rev. **157**, 262 (1967).
13. T. Miyakawa and D. L. Dexter, Phys. Rev. B **1**, 2961 (1970).
14. J. C. Wright, in **Topics in Applied Physics Vol. 15**, ed. F. K. Fong (Springer-Verlag, Berlin, 1976) p239.
15. F. Auzel, Proc. IEEE **61**, 758 (1973).
16. R. Reisfeld and C.K. Jorgensen, **Lasers and Excited States of Rare Earths** (Berlin, Springer-Verlag, 1977).
17. B. Di Bartolo, **Energy Transfer Processes in Condensed Matter** (Plenum, New York, 1984).
18. B. R. Judd, **Operator Techniques in Atomic Spectroscopy** (McGraw-Hill, New York, 1963).

19. R. D. Peacock, in **Structure and Bonding Vol.22**, ed. J. D. Dunitz, P. Hemmerich, R. H. Holm, J. A. Ibers, C. K. Jorgensen, J. B. Neilands, D. Reinen, and R. J. P. Williams (Springer-Verlag, New York, 1975) p83.

20. W.T. Carnall, H. Crosswhite, and H.M. Crosswhite, Energy Level Structure and Transition Probabilities of the Trivalent Lanthanides in LaF_3 , The Johns Hopkins University Reasearch Report, unpublished.

21. A. Kiel, "Multiphonon Spontaneous Emission in Paramagnetic Crystals", in **Quantum Electronics Vol. 1**, ed. P. Grivet and N. Bloembergen (Columbia University Press, New York, 1964) p765.

22. L. A. Riseberg and H. W. Moos, Phys. Rev. **174**, 429 (1968).

23. T. Kushida, S. Kinoshita, T. Ohtsuki, and T. Yamada, Solid State Comm. **44**, 282 (1982).

24. T.T. Basiev, A. Yu. Dergachev, Yu. V. Orlovskii, Rev. Roum. Phys. **34**, 789 (1989).

25. J. Cruz, G. Giuliani, and H. M. van Driel, Opt. Lett. **15**, 282 (1990).

26. K. Palambo, S. Matthews, S. Sheldrake, and D. Capps, in **Advanced Solid State Lasers and Compact Blue-Green Lasers Technical Digest, 1993** (Optical Society of America, Washington, D.C., 1993), **Vol. 2**, p61.

27. C. Bibeau, S. A. Payne, and H. T. Powell, in **Advanced Solid State Lasers and Compact Blue-Green Lasers Technical Digest, 1993** (Optical Society of America, Washington, D.C., 1993), **Vol. 2**, p64.

28. T. Forster, Ann. Phys. (Liepzig) **2**, 55 (1948).

29. D. L. Dexter, J. Chem. Phys. **21**, 836 (1953).

30. M. Inokuti and F. Hirayama, J. Chem. Phys. **43**, 1978 (1965).

31. C. M. Lawson, R. C. Powell, and W. K. Zwicker, Phys. Rev. B **26**, 4836 (1982).

32. J. K. Tyminski, R. C. Powell, and W. K. Zwicker, Phys. Rev. B **29**, 6074 (1984).

33. R. C. Powell, S. A. Payne, L. L. Chase, and G. D. Wilke, Phys. Rev. B **41**, 8593 (1990).

34. R. M. Macfarlane, F. Tong, A. J. Silversmith, and W. Length, Appl. Phys. Lett **52**, 1300 (1988).

35. W. Length and R. M. Macfarlane, J. Lumin. **45**, 346 (1990).

36. W. J. C. Grant, Phys. Rev. B **4**, 648 (1971).

37. A. I. Burshstein, Sov. JETP Phys. **35**, 882 (1972).

38. S. Chandrasekhar, Rev. Mod. Phys. **15**, 1 (1943).

39. H. B. Rosenstock, Phys. Rev. **187**, 1166 (1969).

40. V. M. Kenkre, Phys. Rev. B **18**, 4064 (1978).

41. M. Yokota and O. Tanimoto, J. Phys. Soc. Japan **22**, 779 (1967).

42. H. C. Chow and R. C. Powell, Phys. Rev. B **21**, 3785 (1980).

43. A. E. Siegman, **Lasers** (University Science Books, Mill Valley, Ca., 1986).

44. A. Yariv, **Quantum Electronics 3ed** (John Wiley, New York, 1989).

45. M. G. Jani, R. R. Reeves, R. C. Powell, G. J Quarles, and L. Esterowitz, J. Opt. Soc. Am. B **8**, 741 (1991).

46. L. F. Johnson, J. E. Guesic, and L. G Van Uitert, Appl. Phys. Letters **7**, 127 (1965).

47. L. F. Johnson, J. E. Guesic, and L. G. Van Uitert, Appl. Phys. Letters **8**, 200 (1966).

48. G. J. Quarles, A. Rosenbaum, C. L. Marquardt, and L. Esterowitz, Appl. Phys. Letters **55**, 1062 (1989).

49. T. Y Fan, G, Huber, R. L. Byer, and P. Mitzerlich, Optics Letters **12**, 678 (1987).

50. J. C. Tyminski, D. M. Franich, and M. Kokta, J. Appl. Phys. **65**, (1989).

51. B. M. Antipenko, V. A. Buchenkov, A. S. Glebov,T. I. Kiseleva, A. A. Nikitichev, and V. A. Pismennyi, Opt. Spectrosc. (USSR) **64**, 772 (1988).

52. T. Y. Fan, G. Huber, R. L. Byer, and P. Mitzerlich, IEEE J. Quantum Electron. **JQE-24**, 924 (1988).

53. G. Huber and P. Mitzerlich, J. Luminescence **40-41**, 509 (1988).

54. K. Y. Kim, Y. S. Choi, R. V. Hess, C. H. Blair, P. Brockman, N. P. Barnes, G. W. Henderson, and M. Kokta, in **Digest of Conference on Advanced Solid State Lasers** (Optical Society of America , Washington, D.C. , 1990), paper WB3.

55. T. Becker, R. Clausen, G. Huber, E. W. Duczyski, and P. Mitzerlich, in **Proceedings of Tunable Solid State Lasers Conference 5** (Optical Society of America, Washington, D.C., 1989), p. 150.

56. G. Armagan, A. M. Buoncristiani, and B. Di Bartolo, J. Luminescence **48-49**, 171 (1991).

57. G. Armagan, A. M. Buoncristiani, and B. Di Bartolo, Opt. Mater. **1**, 11 (1991)

58. T. Becker and G. Huber, **Proc. of the Conf. on Lasers and Electro-optics** (Optical Society of America, Washington, D.C., 1991), paper CTuO3.

59. V. A. French and R. C. Powell, Optics Letters **16**, 666 (1991).

60. V. A. French, R. R. Petrin, R. C. Powell, and M. Kokta, Phys. Rev. B **46**, 8018 (1992).

61. S. A. Payne, L. L. Chase, L. K. Smith, W. L. Kway, and W. F. Krupke, to be published.

62. J. B. Gruber, M. E. Hills, R. M. Macfarlane, C. A. Morrison, G. A. Turner, G. J. Quarles, G. J. Kintz, and L. Esterowitz, Phys. Rev. B. **40**, 9464 (1989).

63. J. B. Gruber, M. E. Hills, M. D. Seltzer, S. B. Stevens, C. A. Morrison, G. A. Turner, and M. R. Kokta, J. Appl. Phys. **69**, 8183 (1991).

64. J. A. Caird, L. G. DeShazer, and J. Nella, IEEE J. Quantum Electron. **QE-11**, 874 (1975).

65. M. Kh. Ashurov, Yu. K. Voron'ko, E. V Zharikov, A. A. Kaminskii, V. V. Osiko, A. A. Sobol', M. I. Timoshechkin, V. A. Fedorov, and A. A. Shabaltai, Inorg. Mater. **15**, 979 (1979).

66. J. A. Caird, A. J. Ramponi, and P. R. Staver, J. Opt. Soc. Am. B **8**, 1391 (1991).

67. G. Kintz, I. D. Abella, and L. Esterowitz, **Proc. of the International Conference on Lasers, LASERS '87**, 398 (1987).

68. A. A. Nikitichev, Sov. J. Quantum Electron. **18**, 918 (1988).

69. S. R. Bowman, M. J. Winnings, R. C. Y. Auyeung, J. E. Tucker, S. K. Searles, and B. J. Feldman, IEEE J. Quantum Electron. **JQE-27**, 2142 (1991).

70. T.Y. Fan and R.L. Byer, IEEE J. Quantum Electron. **QE-24**, 895 (1988).

71. F. Hanson and D. Haddock, Apll. Optics **27**, 80 (1988).

72. D.P. Caffey, R.A. Utano, and T.H. Allik, Appl. Phys. Lett. **56**, 808 (1990).

73. R.A. Fields, M. Birnbaum, and C.L. Fincher, Appl. Phys. Lett. **51**, 1885 (1987).

74. T.H. Allik, M.J. Ferry, R.J. Reeves, R.C. Powell, W.W. Hovis, D.P. Caffey, R.A. Utano, L. Merkle, and C.F. Campana, J. Opt. Soc. Am. B. **7**, 1190 (1990).

75. M.J. Ferry, M. L.Kliewer, R.J. Reeves, R.C. Powell, and T.H. Allik, J. Appl. Phys. **68**, 6372 (1990).

76. T.Y. Fan and M.R. Kokta, J. Quantum Electron. **QE-25**, 1845 (1989).

77. M.L. Kliewer and R.C. Powell, IEEE J. Quantum Electron. **QE-27**, 850 (1989).

78. R. R. Petrin, M. L. Kliewer, J. T. Beasley, R. C. Powell, I. D. Aggarwal, and R. C. Ginther, IEEE J. Quantum Electron. **QE-27**, 1031 (1991).

79. B.R. Reddy and P. Venkateswarlu, J. Chem. Phys. **79**, 1519 (1983).

80. T.Y. Fan and R.L. Byer, J. Opt. Soc. Am. B **11**, 1519 (1986).

81. G.E. Venikuoas, G.J. Quarles, J.P. King, and R.C. Powell, Phys. Rev. B **30**, 2401 (1984).

82. J. A. Mares, B. Jacquier, C. Pedrini, and G. Boulon, Mat. Phys. Chem. **21**, 237 (1989).

83. M. Malinowski, B. Jacquier, M Bouazoui, M. F. Joubert, and C. Linares, Phys. Rev. B **41**, 31 (1990).

84. J. H. Schloss, L. L. Chase, and L. K. Smith, J. Lumin. **48-49**, 857 (1991).

85. D. Hua, Z. Song, S. Wang, and Z. Rong, J. Chem. Phys. **89**, 5398 (1988).

86. J. B. Gruber, M. E. hills, T. H. Allik, C. K. Jayasankar, J. R. Quagliano, and F. S. Richardson, Phys. Rev. B **41**, 7999 (1990).

87. J. B. Gruber, M. E. hills, C. A. Morrison, G. A. Turner, and M. R. Kokta, Phys. Rev. B **37**, 8564 (1988).

88. W.F. Krupke, J. Quantum Electron. **QE-7**, 153 (1971).

89. A.A. Kaminskii and L. Lui, Phys. Status Solidi A **26**, K21 (1974).

90. W.F. Krupke, M.D. Shinn, J.E. Marion, J.A. Caird, and S.E. Stockman, J. Opt. Soc. Am. B **3**, 102 (1986).

91. L.L. Chase (private communication).

92. J.D. Axe, J. Chem. Phys. **39**, 1154 (1963).

93. W.F. Krupke and J.B. Gruber, Phys. Rev. **139**, A2008 (1968).

94. Z. Song, D. Hua, S. Wang, and Y. Gui, J. Chem. Phys. **89**, 5404 (1988).

95. S.A. Pollack and M. Robinson, Electron. Lett. **24**, 320 (1988).

96. F. Auzel, D. Meichenin, and H. Poignant, Electron. Lett. **24**, 909 (1988).

97. M.C. Brierly and P.W. France, Electron. Lett. **24**, 815 (1987).

98. R.R. Petrin, R.J. Reeves, M.L. Kliewer, R.C. Powell, I.D. Aggarwal and R.C. Ginther, in **OSA Proceedings Vol. 6: Advanced Solid-State Lasers**, eds H . P. Jensssen and G. Dube, (Optical Society of America, Washington, D. C., 1990) p236.

99. J. Lucas, M. Chanthanasinh, and M. Poulain, J. Noncrys. Solids **27**, 273 (1978).

100. L.Wetenkamp, G. F. West, and H. Tobben, J. Non-Cryst. Sol. **140**, 35 (1992).

101. R. Reisfeld, M. Eyal, and C. K. Jorgensen, J. Less. Common Metals **126**, 187 (1986).

102. A. A. Tesar, J. Quant. Spectrosc. Radiat. Transfer **46**, 425 (1991).

103. R. Cases and M. A. Chamarro, J. Sol. St. Chem. **90**, 313 (1991).

104. M. J. Weber, J. Non-Cryst. Sol. **123**, 208 (1990).

105. S.E. Stokowski, R.A. Saroyan, and M.J. Weber, Pub. M-095, U.S. Dept. Of Energy, Lawrence Livermore National Lab. 1978.

106. T.M. Pollak, W.F. Wing, R.J. Grasso, E.P. Chicklis, and H.P. Jenssen, IEEE J. Quantum Electron. **QE-18**,159 (1982).

107. D. Findlay and R.A.Clay, Phys. Lett. **20**, 277 (1966).

108. A.W. Tucker, M. Birnbaum, C.L. Fincher, and J.W. Erler, J. Appl. Phys. **48**, 4907 (1977).

109. R. Beach, S. Weinzapfel, R. Staver, R. Solarz, M. Shinn, and W. Krupke, Opt. Lett. **14**, 856 (1989).

110. J.A. Caird, S.A. Payne, P.R. Staver, A.J.Ramponi, L.L.Chase, and W.F.Krupke, IEEE J. Quantum Electron. **QE-24**, 1077 (1988).

111. S.A. Payne, L.L. Chase, H.W. Newkirk, L.K. Smith, and W.F. Krupke, IEEE J. Quantum Electron. **QE-24**, 2243 (1988).

112. A. A. S. da Gama, G. F. de Sa, P. Porcher, and P. Caro, J. Chem. Phys. **75**, 2583 (1981).

113. D. C. Yeh, W. A. Sibley, and M. Suscavage, J. Appl. Phys. **63**, 266 (1987).

VITA

ROGER R. PETRIN

Candidate for the Degree of

Doctor of Philosophy

Thesis: SPECTROSCOPIC AND LASING PROPERTIES OF RARE-EARTH ION BASED LASER MATERIALS

Major Field: Physics

Biographical:

Personal Data: Born in Fall River, Massachusetts, August 9, 1965, the son of George and Marie Petrin.

Education: Received Bachelor of Science Degree in Electrical Engineering from Southeastern Massachusetts University, North Dartmouth, Massachusetts 1987; completed requirements for the Doctor of Philosophy Degree at Oklahoma State University, Stillwater, Oklahoma in May, 1993.